8-2022

Development of Metal Halide Perovskites for Radiation Detection

Ryan Tan
University of Tennessee, Knoxville, rtan3@vols.utk.edu

To the Graduate Council:

I am submitting herewith a dissertation written by Ryan Tan entitled "Development of Metal Halide Perovskites for Radiation Detection." I have examined the final electronic copy of this dissertation for form and content and recommend that it be accepted in partial fulfillment of the requirements for the degree of Doctor of Philosophy, with a major in Nuclear Engineering.

Eric D. Lukosi, Major Professor

We have read this dissertation and recommend its acceptance:

Jason P. Hayward, Charles L. Melcher, Mahshid Ahmadi

Accepted for the Council:

Dixie L. Thompson

Vice Provost and Dean of the Graduate School

(Original signatures are on file with official student records.)

Development of Metal Halide Perovskites for Radiation Detection

A Dissertation Presented for the
Doctor of Philosophy
Degree
The University of Tennessee, Knoxville

Ryan Tan
August 2022

ACKNOWLEDGEMENTS

I would like to acknowledge and express my gratitude to the following individuals:

Dr. Eric Lukosi, for his guidance and mentorship as my advisor during my entire time at the University of Tennessee, and without whom the research presented in this dissertation would not be possible.

Dr. Mahshid Ahmadi, Dr. Jason Hayward, and Dr. Chuck Melcher for their support throughout my dissertation research and coursework as committee members and professors.

Dr. Bin Hu, Dr. Kate Higgins, Dr. Jonghee Yang, Bogdan Dryzhakov, and Jakob Cielo for their collaboration within the Materials Science and Engineering department at the University of Tennessee.

Jessica Charest, Lance Drouet, Owen Johnson, Chris Busch, and Chris Shaff for their hard work in support of this project.

I would also like to acknowledge the NNSA Graduate Fellowship Program, along with Y-12 National Security Complex for partially funding my graduate studies at the University of Tennessee.

This research was conducted at the Institute for Advanced Materials and Manufacturing (IAMM) at the University of Tennessee-Knoxville. This material is based upon work supported by the U.S. Department of Homeland Security under grant no. 16DNARI00018-04-0. Part of this work was conducted in the Micro-Processing Research Facility, a University of Tennessee Core Facility. The collaboration with OSU was partially supported by the U.S. Department of Defense, Defense Threat Reduction Agency under Grant HDTRA-11910024.

Disclaimer: The views and conclusions contained in this document are those of the authors and should not be interpreted as necessarily representing the official policies, either expressed or implied, of the U.S. Department of Homeland Security.

Finally, I reserve my deepest gratitude to my family and friends and their unwavering love, encouragement, and support.

Soli Deo Gloria

ABSTRACT

Metal halide perovskite (MHP) semiconductors have attracted significant interest in recent years within photovoltaic and radiation detection communities due to their inexpensive solution growths, high effective atomic number for gamma and X-ray sensing, suitable bandgap, large resistivity, and moderate mobility-lifetime products. The MHP stoichiometry can also be tuned as needed to achieve desired physical and electronic properties. Moreover, the hybrid or organometallic halide perovskite (OMHP) variants contain a large atomic fraction of hydrogen for fast neutron sensing. These qualities make MHPs an attractive low-cost option for meeting detector needs within nuclear security and imaging applications. This work presents the development of MHPs for radiation sensing, with the majority of the results pertaining to a specific OMHP variant, methylammonium lead tribromide ($CH_3NH_3PbBr_3$, $MAPbBr_3$, or MAPB). The implementation of birefringence screening, chemomechanical polishing, and tin oxide electrode designs as improvements to the detector fabrication process are demonstrated, followed by benchmarking of the charge transport properties through alpha particle irradiation, X-ray induced photocurrents, and deconvolution of preamplifier signals. Notable achievements in radiation sensing are then presented, including X-ray imaging with MAPB, the development of a bi-parametric program to improve gamma ray sensing, and thermal neutron sensing with lithium-doped MAPB. Finally, the negative effects of radiation damage on the performance of MHP devices are demonstrated, followed by the evaluation of annealing and low temperature testing as strategies to mitigate detector degradations over time and improve radiation detection performance. Although certain challenges remain to minimize physical and electronic defects to improve detector stability and charge transport properties, the methods and findings presented in this dissertation demonstrate the potential for MHP radiation sensors to meet detector requirements within nuclear security and imaging applications.

TABLE OF CONTENTS

LIST OF FIGURES

LIST OF TABLES

Chapter 1: Introduction

The solid-state radiation detection systems commercially deployed in nuclear security and X-ray imaging applications are generally well-established. Despite the unique requirements that both fields possess, there exists a common need for the development of new materials and methods to reduce cost, improve detection efficiency, increase volume and surface area, decrease the logistical burdens associated with fabrication and operation, and ensure long-term stability of detection systems. This chapter will first provide an overview of the requirements and current state of radiation detection systems for nuclear security and X-ray imaging, followed by a more focused discussion on the physics and challenges of semiconductor detectors. The discussion will then introduce perovskites as a potential semiconducting detector material to meet the needs of the nuclear security and X-ray imaging industries, and literature review of reported achievements in sensing gamma rays, neutrons, and X-rays with perovskites will be presented. The chapter will conclude with the challenges associated with perovskite radiation detectors that hinder their performance and the efforts that have been made to mitigate their effects.

1.1. Detectors for Nuclear Security and X-ray Imaging

Nuclear Security

Requirements

A principal component of radiation detectors for nuclear security is the ability to distinguish between benign sources and material that could potentially be harmful to the public and environment. The latter includes special nuclear material (SNM), which refers to the radioactive material needed to create a nuclear weapon such as plutonium and uranium enriched in $^{239/241}$Pu and $^{233/235}$U, as well as any radioactive material outside of regulatory control that could be inadvertently or maliciously released. This proves to be a challenging task, as apart from SNM, there remain many radioisotopes that have benign uses in modern technology and medicine. Commercially used sources include ^{241}Am, ^{133}Ba, ^{137}Cs, ^{57}Co, ^{60}Co, ^{92}Ir, ^{226}Ra, and depleted uranium (DU). Additionally, medical isotopes such as ^{14}C, ^{51}Cr, ^{18}F, ^{67}Ga, ^{123}I, ^{131}I, ^{111}In, ^{153}Sm, ^{89}Sr, ^{99m}Tc, and ^{201}Tl are commonly used in radiopharmaceuticals. Finally, naturally occurring radioactive material (NORM), which consists of ^{40}K, ^{238}U, and ^{232}Th, is found in trace quantities

virtually anywhere on earth and is considered a nuisance source for detection systems [1]. Because these isotopes can have overlapping radiation signatures, their presence contributes to a phenomenon dubbed "radiation clutter," and often raise false alarms at radiation monitoring stations searching for illicit nuclear material [2]. As a result, the identification of radioactive material is of paramount importance, and strong nuclear security regimes require detectors that not only detect radiation, but also possess high resolution, have ability to sense neutrons given that few benign sources are neutron emitters, and can be widely deployed in order to achieve this mission.

Current State

The majority of deployed detection technologies are semiconductors (Si, Ge, CdTe, and CZT) and scintillators (NaI:Tl, CsI:Tl, $LaBr_3$:Ce, $CeBr_3$, polyvinyltoluene (PVT), CsLiYCl:Ce (CLYC), and $Bi_4Ge_3O_{12}$ (BGO)) [3]. The most prevalent commercial handheld radioisotope identification devices (RIIDs) currently deployed are listed in Table 1.1.1, which show clear tradeoffs between excellent spectroscopic performance (in terms of energy resolution), detector volume, and cost. While HPGe detection systems possesses the highest resolution, they are easily the most expensive and the most burdensome, as much of the unit is devoted towards keeping the crystal cooled to cryogenic temperatures. Additionally, although CZT possesses the second-best resolution and can be operated at room temperature, the growth yields are relatively low compared to other materials, which increase the cost of production. As a result, NaI:Tl is the most ubiquitous due to its relatively lower cost per unit volume despite its moderate resolution compared to semiconductor materials [3]. Meanwhile, the development solid-state neutron sensors such as elpasolite and plastic scintillators along with conversion layers on semiconductors has not yet been able to supplant ^{3}He gas detectors as the most widely deployed neutron sensor [4], leaving a gap in the market for a low-cost, solid-state, dual gamma/neutron sensor that can be grown in large volumes and possesses sufficient resolution for nuclear security applications.

Table 1.1.1. Comparison of commercial handheld radioisotope identification devices [5]

Detector	Resolution (662 keV)	Detector Volume (cm^3)	Total Weight** (lbs)	Cost per Unit (US Dollars)
NaI:Tl	6 - 8%	10 - 350	2.6 – 10.8	9,500 – 32,000
$LaBr_3$:Ce	2 – 4%	20 - 45	2.3 – 8.9	22,950 – 42,000
$CeBr_3$	4 – 5%	45	4.8 – 6.5	17,600 – 33,135
CZT*	1 – 2%	1 – 2.5	2.0 – 2.5	15,510 – 36,000
HPGe	< 0.2%	80 - 175	15.0 – 37.1	85,000 – 98,150

*Due to the low yield of CZT growth, most handheld RIDs contain between 4-6 CZT detectors arranged in an array

** Total weight include detector, base unit, batteries, and probes (if applicable)

X-ray Imaging

Requirements

X-ray imaging applications, such as security scanners or medical imaging procedures, desire detectors that possess large active areas, have high sensitivity, are efficient at detecting X-rays within relevant energy ranges for the application, and exhibit a high signal-to-noise ratio (SNR) to minimize the irradiation time and remain within dose limits. In X-ray cargo scanning security systems, the total dose to the cargo is limited to 0.5 Gy, and the standard dose rate limit to drivers, control room operators, and other operational crew members is set to 0.5 $\mu Sv\ h^{-1}$ [6, 7]. These requirements limit the dose rates that X-ray cargo scanners can utilize, which necessitates the need to advance the imaging detector capabilities. Currently, high-density scintillator materials such as $CdWO_4$ and $PbWO_4$ are used for cargo scanning, although high-Z sensitized plastic scintillators have been considered as well [8, 9]. For this application, cost-effective and large area detectors are critical to efficiently scan large objects, which are reasons why scintillators have typically been preferred over semiconductors due to the latter being traditionally more expensive per unit volume as referenced in the previous section. Medical imaging dose rate requirements, on the other hand, are more well defined. Depending on the type of examination, routine multi-slice diagnostic computed tomography (CT) scans use dose rates of approximately 0.20 $mGy\ mA^{-1}\ s^{-1}$ to deliver between ~50 mGy (chest, C-spine, abdomen) and 100 mGy (L-spine) of total dose to an adult patient, while 4D respiratory correlated CT scans range from 250 to 400 mGy of total dose. Moreover, medical X-ray imaging procedures follow dose limits set by the U.S. Food and Drug Administration and the National Cancer Institute beyond which injuries to the eyes and skin begin to occur:1 Gy for eye lens opacity, 5 Gy for debilitating cataracts, and up to 15 Gy for dermal necrosis and the death of most skin cells [10-12].

Current State

Typical scintillators used for medical imaging include CsI:Tl scintillators formed on amorphous silicon photodetector arrays [13], $Lu_2Si_2O_5$:Ce (LSO), $(LuY)_2Si_2O_5$:Ce (LYSO), $LuAlO_3$:Ce (LuAP), $(Lu_{0.7}Y_{0.3})AlO_3$:Ce (LuYAP), $Bi_4Ge_3O_{12}$ (BGO), and Gd_2O_2S:Pr (GOS) [14, 15]. Semiconductor imaging devices are typically of amorphous selenium detectors, which are

very efficient for soft X-rays (<40 keV) making them suitable for mammography. However, the α-Se detectors possess poor mobility-lifetime product (10^{-7} cm^2 V^{-1}), require extremely high operational electric fields (15 V μm^{-1}), and have poor stopping power for hard X-rays (>40 keV) [13]. Higher energy X-ray applications typically utilize CZT, although as previously mentioned, the material is expensive to produce, limited to single detector elements, and used more for dosimetry rather than imaging [16]. Si and HgI_2 have also been utilized as direct conversion layers for digital X-ray imaging [17].

1.2. Semiconductor Radiation Sensors

While both scintillators and semiconductors have been presented as widely utilized detection materials within nuclear security and imaging up to this point, it is generally semiconductors that possess the greater potential for high resolution radiation detection within these fields. This is due to the direct collection of radiation induced charge in semiconductors, smaller energy required per recorded interaction (typically several eV for electron-hole pairs in semiconductors and tens of eV per photon in scintillators), and lower variance in semiconductor signals compared to scintillators that typically possess non-proportional scintillation and non-uniform light collection [3, 18]. Table 1.2.1 contains an expanded list of the most prominent semiconductors evaluated for radiation detection systems, which include both compound semiconductors and elemental semiconductors.

There are several key factors that determine a semiconductor's effectiveness as a radiation detector. The first is the material's atomic number (Z for elemental, Z_{eff} for compounds). In sensing charged particles, gamma rays, and X-rays, the vast majority of interactions occur with electrons in the material. High Z materials have a high density of electrons, which make the photon interaction probability high. On the other hand, neutron sensing requires low Z materials to effectively moderate the neutrons and increase the probability of a nuclear reaction, which produces charged particles and gamma rays that can be sensed by the detector. The density of the material is also positively corelated to the interaction probability in that incident radiation is more likely to interact with denser materials, regardless of their Z. Another factor is the bandgap (E_g), or the energy difference between the conduction band minimum (CBM) and the valence band

Table 1.2.1. Comparison of semiconductors for spectroscopic radiation sensing [3, 18-20]

Detector	**Density ($g\ cm^{-3}$)**	**Resistivity (Ω-cm)**	**μ_e ($cm^2\ V^{-1}\ s^{-1}$)**	**τ_e (s)**	**$\mu_e\tau_e$ ($cm^2\ V^{-1}$)**	**μ_h ($cm^2\ V^{-1}\ s^{-1}$)**	**τ_h (s)**	**$\mu_h\tau_h$ ($cm^2\ V^{-1}$)**
HPSi	2.33	10^5	1400	$>10^{-3}$	>1	1900	10^{-3}	~1
HPGe	5.33	50	3900	$>10^{-3}$	>1	1900	2×10^{-3}	>1
InP	4.78	10^9	4600	1.5×10^{-9}	5×10^{-6}	150	$<10^{-7}$	$<1.5 \times 10^{-5}$
GaAs	5.32	10^8	8000	10^{-8}	8×10^{-5}	400	10^{-7}	4×10^{-6}
CdTe	5.85	10^9	1100	3×10^{-6}	3×10^{-3}	100	2×10^{-6}	2×10^{-4}
CdZnTe	5.78	10^9-10^{10}	1000	3×10^{-6}	4×10^{-3}	120	1×10^{-6}	1.2×10^{-4}
HgI_2	6.4	10^{13}	100	3×10^{-6}	3×10^{-4}	4	1×10^{-5}	4×10^{-5}
PbI_2	6.2	10^{13}	8	10^{-6}	1×10^{-5}	2	3×10^{-7}	3×10^{-7}
TlBr	7.56	10^{12}	30	2.5×10^{-6}	5×10^{-4}	4	3.7×10^{-5}	2×10^{-6}

maximum (VBM). The W-value, or the energy it takes to create an electron-hole pair, is related to E_g as shown in Figure 1.2.1. Because the elemental semiconductors (Si and Ge) have narrow bandgaps and small W-values, these materials have historically offered the best path towards extremely high-resolution sensors due to the larger number of electron-hole pairs generated per radiation interaction. However, large dark currents from thermally generated charge carriers significantly lower the signal to noise ratio at room temperature. Compound semiconductors, on the other hand, offer significant improvements in bulk resistivity as compared to their elemental counterparts that lead to reductions in dark current, which is shown in Table 1.2.1.

Finally, the transport of electrons and holes within the detector a fundamental parameter in determining its capabilities for radiation detection, and is often represented by the product of the mobility (μ) and lifetime (τ) for each carrier. As shown in Table 1.2.1, the elemental intrinsic semiconductors have the highest $\mu\tau$ by several orders of magnitude over the compound semiconductors, with the values for holes and electrons approaching unity. Compound semiconductors, while offering increased resistivity, possess significantly more trap states than elemental semiconductors, likely due to impurities, lack of stoichiometry, or mechanical damage caused by the fabrication process [19]. This significantly reduces the drift length of the carriers (λ) shown in Equation 1.2.1 due to a lower $\mu\tau$ for both carriers, and consequently limits the size and efficiency of compound semiconductor detectors for radiation sensing without correction techniques.

$$\lambda = \mu\tau E \tag{1.2.1}$$

It can be seen from Table 1.2.1 that the $\mu\tau$ values in compound semiconductors are also imbalanced with the electron transport higher than that of holes by orders of magnitude. For planar electrode devices in the ideal case of high carrier lifetime and absence of traps, the induced charge from a single ionizing radiation interaction is illustrated in Figure 1.2.2B and mathematically represented by Equation 1.2.2 (a simplified version of the Shockley-Ramo Theorem [21]) where *n* represents the energy dependent number of generated charge carriers, $\mathbf{e_0}$ is the elementary charge, and *X* is the depth of interaction. The first term in Equation 1.2.2 is the contribution from the movement of electrons and the second term is the contribution from the movement of holes, which sums to the total number of charge carriers initially generated [22]. When the drift length of one

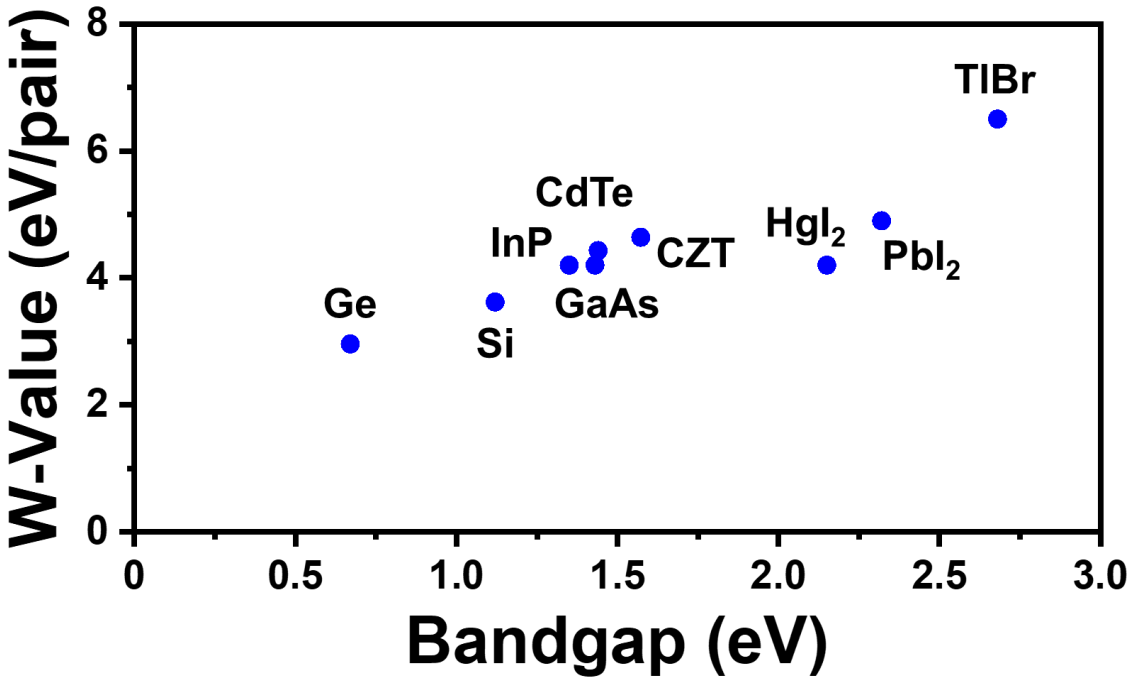

Figure 1.2.1 W-value vs bandgap for the semiconductors listed in Table 1.2.1

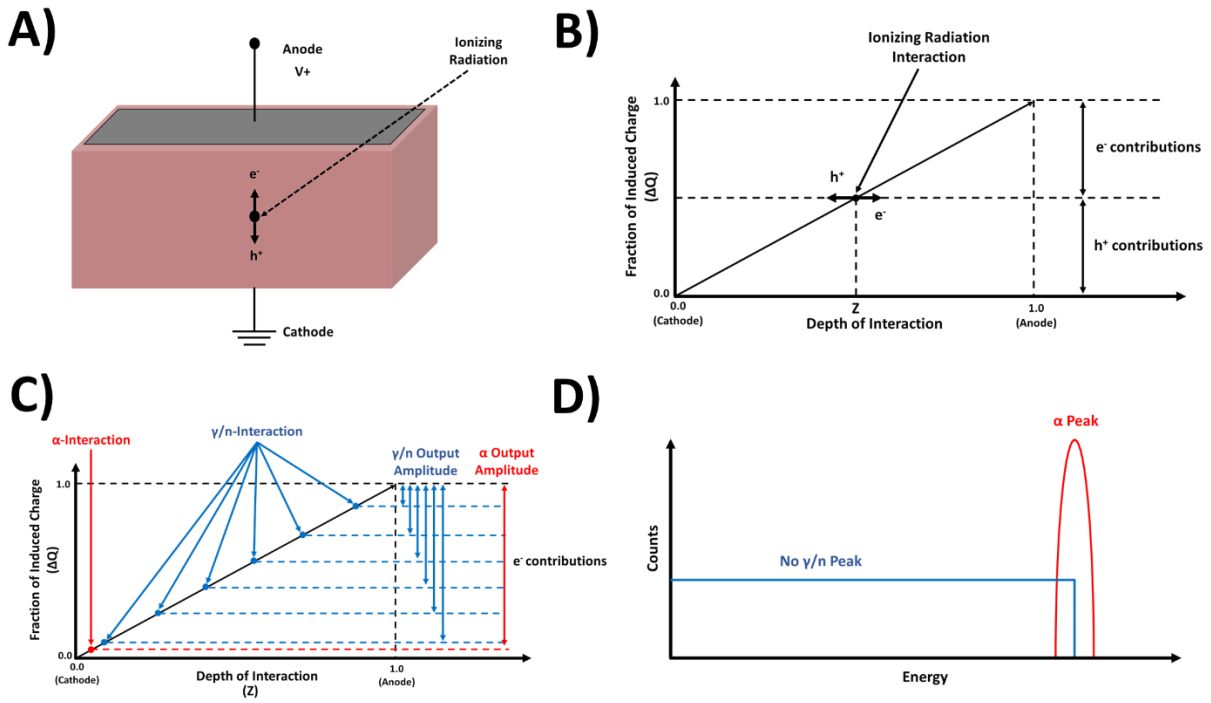

Figure 1.2.2. Depth dependent charge sensing: A) Detector with planar electrodes B) Signal contributions from holes and electrons in an ideal detector. C) Depth dependent energy deposition of alpha particles and gamma/neutrons with significantly poorer charge transport for one carrier D) Expected pulse height spectra from the radiation interactions Figure C

charge carrier, holes for example, is much smaller than the thickness of the detector due to low $\mu_h\tau_h$ as is the case for the semiconductors in Table 1.2.1, they cannot travel far enough to induce an appreciable signal and as a result, Equation 1.2.2 reduces to Equation 1.2.3.

$$\Delta Q = ne_0(X) + ne_0(1 - X) = ne_0 \tag{1.2.2}$$

$$\Delta Q_e = ne_0(X) \tag{1.2.3}$$

With poor hole transport properties, only electrons contribute to the ionizing radiation-induced signal as the holes do not reach the cathode to induce a signal proportional to the original charge generated [19]. For heavy charged particles (such as α-particles) and low energy photons, spectroscopy is still possible because of their short range in solid matter. This yields a relatively narrow range of induced signals, allowing peaks to be resolved as shown in Figure 1.2.2D. This is not the case for high energy radiation and indirectly ionizing radiation (i.e. photons and neutrons), which can deposit energy stochastically throughout the detector. Therefore, the output signal becomes depth dependent, and from Equation 1.2.3, the induced charge will range from 0 to ne_0, yielding little spectroscopic information. The same principles hold true for the opposite case where electrons have very short drift lengths compared to holes.

To address this deficiency of imbalanced carrier transport properties, various single carrier charge sensing techniques and correction methods have been developed to improve spectroscopic performance in compound semiconductors. Certain techniques such as Frisch grids, hemispherical, pixel, and coplanar geometries utilize the near-field effect to reduce the positional dependence of the radiation interaction and remove contributions from the slower moving carrier by ensuring that they traverse a region with weak signal induction while the other carrier travels through a high field region with high signal induction [23-31]. From the Shockley-Ramo theorem, a charge Q induced on an electrode due to a point charge q moving from a point x_i to x_f is represented by Equation 1.2.4, where E_w and Φ_w refer to the weighting field and weighting potential respectively [21]. The weighting field is different from the permanent electric field in that while the electric field determines the trajectory and velocity of the charge carrier, the weighting field determines how the charge motion is coupled to an electrode. These two fields are identical and easily calculated for simple two-electrode geometries, however, solutions for complex geometries usually require computational modeling [19]. From Equation 1.2.4, it can be seen that the induced

charge is dependent only on the gradient of the weighting potential. Dividing both sides of the equation by the time differential Δt yields $I(t)$, the instantaneous induced current, which is represented as Equation 1.2.5. In this equation, v represents the velocity of the charge carrier, μ is the carrier mobility, and E is the static permanent electric field. While mobility as a bulk property is not easily modified after growth and shaping the electric field often adversely affects leakage current and charge collection efficiency, the near field effect manipulates the weighting field so that charge is generated in a high-field region that is small relative to the detector volume and close to the collecting electrode, thereby maximizing $\Delta\Phi_w$ and the induced current.

$$\Delta Q = \int_{x_i}^{x_f} q\vec{E}_w \, dx = -q\Delta\Phi_w]_{x_i}^{x_f} \tag{1.2.4}$$

$$I(t) = \frac{q\Delta\Phi_w}{\Delta t} = q\vec{v}\vec{E}_w = q(\mu\vec{E})\vec{E}_w \tag{1.2.5}$$

While near field effect has been shown to dramatically improve radiation sensing capabilities, complex fabrication, electronic, and computational techniques are often required. Alternatively, the negative effects of the imbalanced carriers can be corrected for and mitigated during post-processing. Rise time discrimination, as the name implies, relies on the differences in rise time between holes and electrons to improve spectral shape by setting a rise time threshold to reject signals dominated by the slower carrier, which are identified by slower rise times. While this technique has been shown to increase energy resolution in CZT (1 keV FWHM to 0.7 keV FWHM at 59.54 keV), it also results in a significant loss in efficiency due to the discarded pulses [32, 33]. On the other hand, since rise time and pulse height are depth dependent, it is possible to generate a set of correction factors by plotting rise time as a function of pulse amplitude and energy. By multiplying the measured charge by the appropriate correction factor, a corrected pulse amplitude can be generated to correct for loss of charge during drift. This technique has also improved resolution in TlBr (5.8% to 4.3% at 122 keV) and does not result in the loss of sensitive volume. However, the electronics are complex, and because the ballistic deficit varies nonlinearly with rise time, the reported bi-parametric techniques cannot be applied over the entire detector depth [34, 35].

From the discussion up to this point, it is clear that reducing the cost of semiconductor radiation detection systems for more widespread deployment requires a combination of cheaper detection media, simpler fabrication and operational methods, or post-processing techniques that correct for variable ballistic deficit without rejecting signals based on dependence or location. The following section will introduce perovskites as a potential low-cost semiconducting material for achieving this goal.

1.3. Perovskite Radiation Sensors

Within the last decade, metal halide perovskites (MHPs) have attracted significant attention as semiconductor radiation sensors due to their impressive performance as photovoltaic and optoelectronic devices [3, 17, 36, 37]. Perovskites generally refer to materials consisting of units with the chemical formula ABX_3 as shown in Figure 1.3.1, where A is a large cation (methylammonium ($CH_3NH_3^+$ or MA), formamidinium ($HC(NH_2)_2^+$ or FA), or Cs^+), B is a smaller metal cation (Sn^{2+}, Bi^{2+}, or Pb^{2+}), and X is a halogen (Cl^-, Br^-, I^-) [38]. MHPs possess many economic, physical, and electronic qualities that are desirable for radiation detection, which will be reviewed in this section.

Low-Cost Growths and High Detection Efficiency

Most single crystal (SC) semiconductors are synthesized via high temperature furnace growth methods, which are expensive and limit widespread commercial production. While MHPs can be fabricated in this manner [39], they can also be grown in large volumes in solution through the mixing of precursor salts which, while less controllable than furnace growth methods, are significantly cheaper [40]. The cost of the MHP semiconductor material has been estimated to be less than \$10 cm^{-3} [36, 41], with some reports placing the figure at less than \$1 cm^{-3} [42, 43]. For comparison, the material cost of CZT is typically greater than \$1000 cm^{-3} [41]. Despite the fact that these values do not consider other costs associated with detection systems that are included in the commercial cost estimates in Table 1.1.1 [5], it is still clear that MHPs are an attractive low-cost option for semiconductor radiation detectors. As previously stated, many MHP variants for radiation sensing contain high Z elements such as Cs, Br, and I in addition to Pb. This results in Z_{eff} greater than or on par with commercial semiconductor radiation sensors such as HPSi, HPGe,

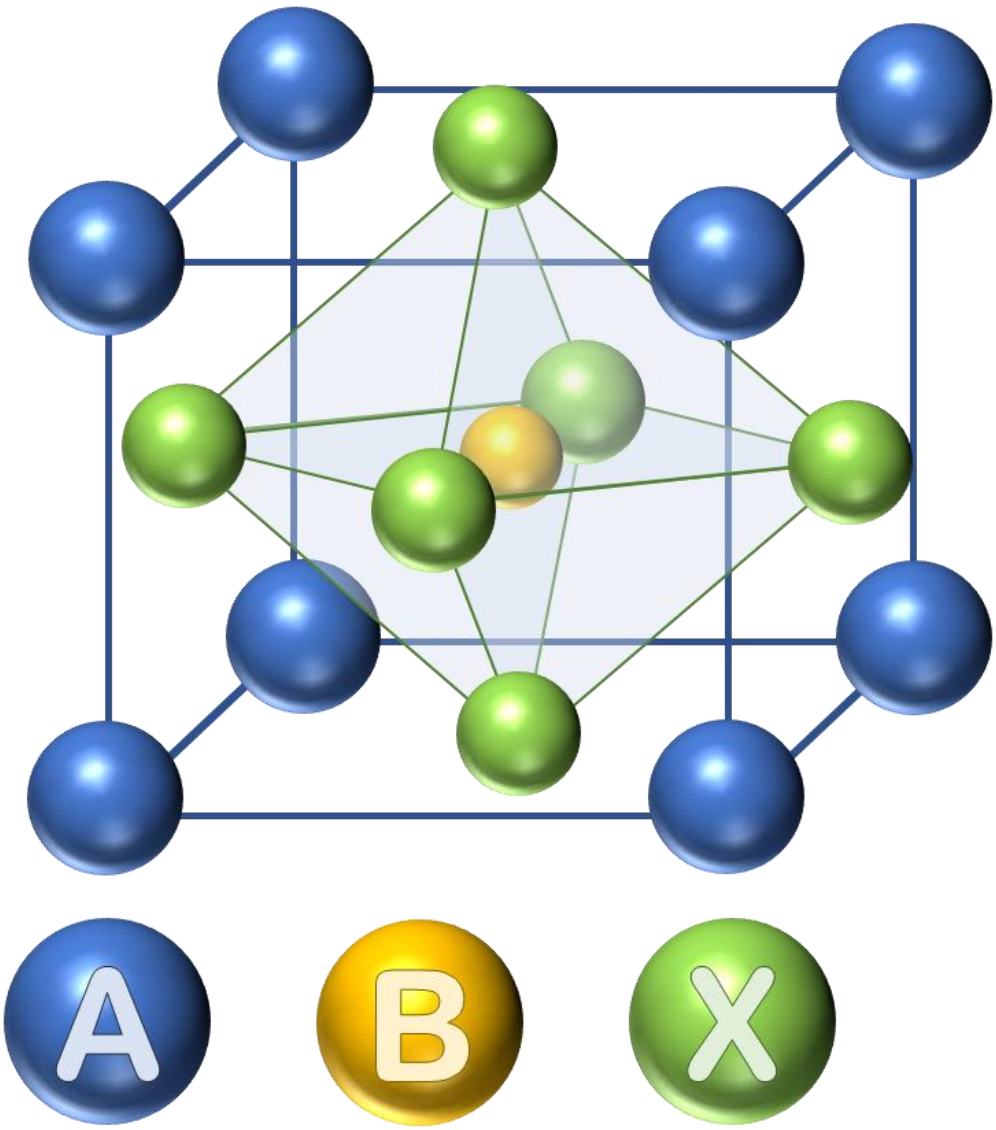

Figure 1.3.1. Single layer perovskite structure

and CZT which, in addition to the desirable density of around 3-4 g cm-3 [17, 36], provides increased detection efficiency for X-rays and gamma rays at a fraction of the cost [17, 19, 37].

Suitable Bandgap and Resistivity

As a general rule of thumb, a bandgap greater than 1.4 eV is required for semiconductors to operate at room temperature, which allows for radiation induced signals to be distinguishable from the dark current produced by thermally generated charge carriers [20]. As opposed to narrow bandgap semiconductor detectors such as HPSi and HPGe that need to be cooled during operation, the bandgaps of MHPs are well suited for room temperature operation. The bandgap of the fully inorganic $CsPbBr_3$ was determined to be 2.3 eV at room temperature [44], while the most common hybrid or "organometallic" halide perovskites (OMHP), $MAPbX_3$, have bandgaps of 1.5, 2.2, and 3.1 eV when the halogen is I, Br, and Cl respectively [37]. The resistivity of MHP detectors is also an important parameter for minimizing dark current and noise to maximize the signal to noise ratio (SNR). While high resistivity semiconductors such as CZT and TlBr have resistivities on the order of 10^{10} to 10^{12} Ω cm, MHP resistivities are reported to be several orders of magnitude lower and range from 10^7 Ω cm for $MAPbI_3$ to 10^{10} Ω cm for $CsPbBr_3$, with $MAPbBr_3$ variants in between [17, 36, 42, 45, 46].

Tunable Stoichiometry

Ever since Stoumpos *et al.* reported the first demonstration of X-ray and gamma ray detection with perovskites using $CsPbBr_3$, MHPs for radiation sensing have typically utilized Pb^{2+} at the B-site while the cations and anions at the A-site and X-site respectively have been utilized interchangeably in various combinations [44]. For example, Nazarenko *et al.* showed that doping $FAPbI_3$ with Cs and Br demonstrated improved phase stability [47]. Electronic properties can also be optimized through judicious selection of dopants, as the bandgap of $MAPbBr_3$ was shown to be tunable by adjusting the Cl doping concentration at the X-site, which also increased the resistivity by reducing the charge carrier concentration of the SC [42]. As a result, various combinations of cations and anions can be incorporated into the MHP stoichiometry to achieve desired properties, provided that the crystal integrity is maintained.

Moderate Mobility-Lifetime Product

Perovskite semiconductors suffer from the same imbalanced charge carrier dynamics as previously described for compound semiconductors, with the difference being that charge induction occurs from the drift of holes as the dominant carriers rather than electrons. As a result, the hole transport properties are a crucial figure of merit to optimize for enhancing gamma ray spectroscopic capabilities. Table 1.3.1 describes the recent progress in improving $\mu_h\tau_h$, gamma sensing, and X-ray sensing parameters in various hybrid and inorganic single layer MHP (ABX_3) SC semiconductors, with X-ray sensing discussed further in subsequent sections.

Typically, the values for $\mu_h\tau_h$ can be derived by fitting charge collection as a function electric field to the single polarity Hecht Equation shown in Equation 1.3.1 that describes the induced charge on electrodes and accounts for the inevitable charge loss due to trap states, where *CCE* is the charge collection efficiency, *E* is the electric field which is assumed to be linear, and *d* is the thickness of the detector [48]. In DC photocurrent-based Hecht fits that use a continuous radiation source for excitation such as LEDs, IR light, UV light, or a continuous flux of X-rays, CCE is represented by changes in induced photocurrents as a function of applied bias. In single quanta sensing modes that use alpha particles or gamma rays, however, CCE is represented by the shifting of peaks within the pulse height spectrum as a function of applied bias. From the reported $\mu_h\tau_h$ values in Table 1.3.1, the orders of magnitude difference in $\mu_h\tau_h$ for the different detectors can be attributed to the manner by which $\mu_h\tau_h$ was determined. With photoconductivity methods, the continuous radiation source generates a sufficient number of carriers within the detector that traps are essentially passivated, leading to enhanced $\mu_h\tau_h$ generally on the order of 10^{-2} cm^2 V^{-1} [42, 43, 47, 49-53] compared to 10^{-4} to 10^{-3} cm^2 V^{-1} for single quanta methods that operate in the space charge free regime with minimal trap passivation [39, 42, 45, 54-59]. Both sets of reported values can be valid depending on the application space and whether the incident radiation has a high count rate (e.g., X-ray imaging) or low count rate (e.g., passive radiation detection) [19, 60].

$$CCE = \frac{\mu_h \tau_h E}{d}\left[1 - \exp\left(-\frac{d}{\mu_h \tau_h E}\right)\right] \tag{1.3.1}$$

Table 1.3.1. Notable achievements in X-ray and gamma sensing with solution grown (unless otherwise indicated) 3D MHP SCs

MHP Variant	Method of measuring $\mu_h\tau_h$	$\mu_h\tau_h$ ($cm^2\ V^{-1}$)	Gamma Source*	Resolution	X-ray Sensitivity ($\mu C\ Gy^{-1}\ cm^{-2}$)	Reference
$FAPbI_3$	8 keV Cu_α X-rays	1.8×10^{-2}	^{241}Am	35%	0.65	[43]
$FA_{0.9}Cs_{0.1}PbI_{2.8}Br_{0.2}$	Photoconductivity	4.0×10^{-2}	^{241}Am ^{137}Cs	-	-	[47]
$CsPbBr_3$	^{241}Am γ rays	1.3×10^{-3}	^{57}Co ^{137}Cs	3.9% 3.8%	-	[54]
$CsPbBr_3$	^{137}Cs γ rays	9.5×10^{-4}	^{241}Am ^{57}Co ^{137}Cs	28.3% 13.1% 5.5%	-	[61]
$CsPbBr_3$ (Bridgman)	^{241}Am γ rays	6.3×10^{-3}	^{137}Cs	1.4%	-	[39]
$CsPbBr_3$	-	-	-	-	770	[62]
$CsPbCl_3$	^{241}Am γ rays	3.2×10^{-4}	^{57}Co	16%	-	[55]
$MAPbI_3$	70 keV Ag X-rays	2.0×10^{-4}	-	-	2527	[49]
$MAPbI_3$	^{241}Am γ rays	8.1×10^{-4}	^{241}Am ^{57}Co	12% 6.8%	-	[56]
$MAPbBr_3$	Photoconductivity	1.2×10^{-2}	-	-	80	[50]
$MAPbBr_3$	^{241}Am α particles	1.6×10^{-3}	-	-	-	[57]
$MAPbBr_3$	^{241}Am α particles	4.2×10^{-4}	-	-	-	[59]
$MAPbBr_3$	-	-	-	-	2.4×10^4	[63]
$MAPbBr_3$	^{210}Po α particles	3.7×10^{-4}	-	-	-	[45]
$MAPbBr_3$	-	-	-	-	359	[64]
$MAPbBr_3$	39 keV W X-rays	4.1×10^{-2}	-	-	259.9	[51]
$MAPbBr_3$	Photoconductivity	2.1×10^{-2}	-	-	1274	[52]
$MAPbBr_3$	Photoconductivity	4.0×10^{-3}	-	-	2.1×10^4	[53]
$MAPbBr_{2.94}Cl_{0.06}$	Photoconductivity	1.8×10^{-2}	^{137}Cs	6.5%	8.4×10^4	[42]

**Gamma Energies: ^{241}Am (59.5 keV), ^{57}Co (122 keV), ^{137}Cs (662 keV)*

Collectively, the described qualities make MHPs an attractive material class for the next generation of radiation sensors [17]. The following sections will provide a review of notable achievements in gamma sensing, neutron sensing, and X-ray imaging with MHPs.

Gamma Sensing with MHPs

Although resolutions of 1.4%, 1.6%, and 1.8% at 662 keV were achieved in a Bridgman grown $CsPbBr_3$ with planar, quasi-hemispherical, and pixelated readouts respectively [39], success has been more limited with gamma sensing in solution grown MHPs. This is significant because a primary motivation for the development of MHPs for radiation sensing was the low cost of solution growth compared to the high costs associated with furnace grown semiconductors such as CZT [3]. Only two solution grown MHP variants have demonstrated spectroscopic capabilities at 662 keV, and the best resolutions of 3.8% and 6.5% for $CsPbBr_3$ and $MAPbBr_{2.94}Cl_{0.06}$ respectively offer only moderate improvements in resolution over the current detector technologies that are on the lower range in terms of cost [5, 42, 54]. The aforementioned imbalanced charge carrier properties play a role in this, as without single charge carrier sensing techniques, the insufficient transport properties of electrons limit the spectroscopic capabilities of MHP SCs. This is evident by the fact that two of the best performing solution grown MHP SC devices reported by He *et al.* for gamma sensing, $CsPbBr_3$ and $MAPbI_3$, also possess $\mu_e\tau_e$ values of 8.8×10^{-4} and 7.4×10^{-4} cm^2 V^{-1} respectively, which are both on par with their $\mu_h\tau_h$ values and lead to decent spectroscopic performance with only planar electrodes [54, 56]. Enhancements to the gamma spectroscopic performance in MHPs without the need for exotic electrode geometries or post-processing techniques requires improvements to the electron transport properties to the point where they are relatively balanced with the hole properties. Another significant contributor to the limited spectroscopic success is the fact that the reported $\mu_h\tau_h$ values obtained via single quanta sensing are relatively low compared to the dominant carrier properties of other high performing semiconductor detector materials from Table 1.2.1, such as HPGe and CZT, which indicate the need for improvements to $\mu_h\tau_h$ as well in order to maximize the efficacy of the single carrier charge collection techniques described in Chapter 1.2 [3, 19].

Finally, the reported results in Table 1.3.1 suggest that fully inorganic $CsPbBr_3$ variants possess the greatest potential for gamma sensing with MHP SCs, and it has been postulated that

the coexistence of organic and inorganic cations within the hybrid MHP variants causes instabilities that prevent from achieving high energy resolution [39]. Despite this, hybrid MHP variants continue to attract interest for development due to their neutron sensing capabilities and potential to act as dual gamma/neutron sensors due to the presence of hydrogen within the stoichiometry, and significant effort has been dedicated to benchmarking the neutron sensing performance of both OMHP semiconductors and scintillators.

Neutron Sensing with MHPs

As previously stated, the detection of neutrons is a critical component of a nuclear security regime as very few materials aside from SNM give off neutron signatures. Notable achievements to date in neutron sensing with perovskite materials are listed in Table 1.3.2. Since hybrid MHPs contain a large atomic fraction of hydrogen within the organic component, they are particularly well-suited for fast neutron sensing. Organometallic halide perovskite (OMHP) variants such as $FAPbBr_3$ and Mn-STA_2PbBr_4 in the forms of nanocrystals and microplates respectively have been shown to scintillate in response to fast neutrons, and fully inorganic $CsPbBr_3$ nanocrystals doped with Mn also showed the same capability [65-67]. Meanwhile, $MAPbBr_3$ SC semiconductors demonstrated fast neutron detection efficiencies comparable to commercial plastic scintillators [45].

None of the aforementioned materials, however, intrinsically possess thermal neutron sensitivity due to the absence of isotopes with high thermal neutron capture cross sections such as ^{6}Li, ^{10}B, ^{155}Gd, and ^{157}Gd within the detector stoichiometry. As a result, MHPs lacking intrinsic thermal neutron sensitivity require extrinsic methods of converting incident thermal neutrons into other forms of radiation, which are shown in Figure 1.3.2. One method shown in Figure 1.3.2A is to use a sheet or foil containing thermal neutron sensitive isotopes to produce gamma rays from the neutron capture reaction, which can then deposit their energy within the detector and produce a response. Using this technique, thermal neutron detection with a $MAPbBr_3$ SC semiconductor was achieved by sensing gamma rays produced from neutron capture reactions within Gd foil as well as a sheet of borated polyethylene [68]. While this detection method is simple, the highly penetrating nature of prompt gamma rays from nuclear reactions result in low detection efficiency without sufficient detector thickness or stopping power, and can also distort any signatures from

Table 1.3.2. Notable achievements in neutron sensing with MHPs. Full chemical formulas are listed in italics to show hydrogen within organic components.

MHP Variant	Detector Type	Structure	Conversion Mechanism	Reference
$FAPbBr_3$ *$(CH_5N_2)PbBr_3$*	Scintillator	Nanocrystal	N/A	[65]
Mn-STA_2PbBr_4 *Mn-$(C_{18}H_{37}NH_3)PbBr_4$*	Scintillator	Microplate	N/A	[66]
$CsPbBr_3$:Mn	Scintillator	Nanocrystal	N/A	[67]
$MAPbBr_3$ *$(CH_3NH_3)PbBr_3$*	Semiconductor	Single Crystal	N/A	[45]
$(PEA)_2PbBr_4$:Li *$(C_8H_{12}N)_2PbBr_4$:Li*	Scintillator	Thin film	Direct	[69, 70]
$CsPbBr_3$	Semiconductor	Thin film	^{10}B film	[71, 72]
$MAPbBr_3$ *$(CH_3NH_3)PbBr_3$*	Semiconductor	Single Crystal	^{10}B layer Gd_2O_3 heterojunction	[73]
$MAPbBr_3$ *$(CH_3NH_3)PbBr_3$*	Semiconductor	Single Crystal	Gd foil Boripoly sheet* Gd_2O_3 pellets	[68]

**Boripoly refers to borated polyethylene*

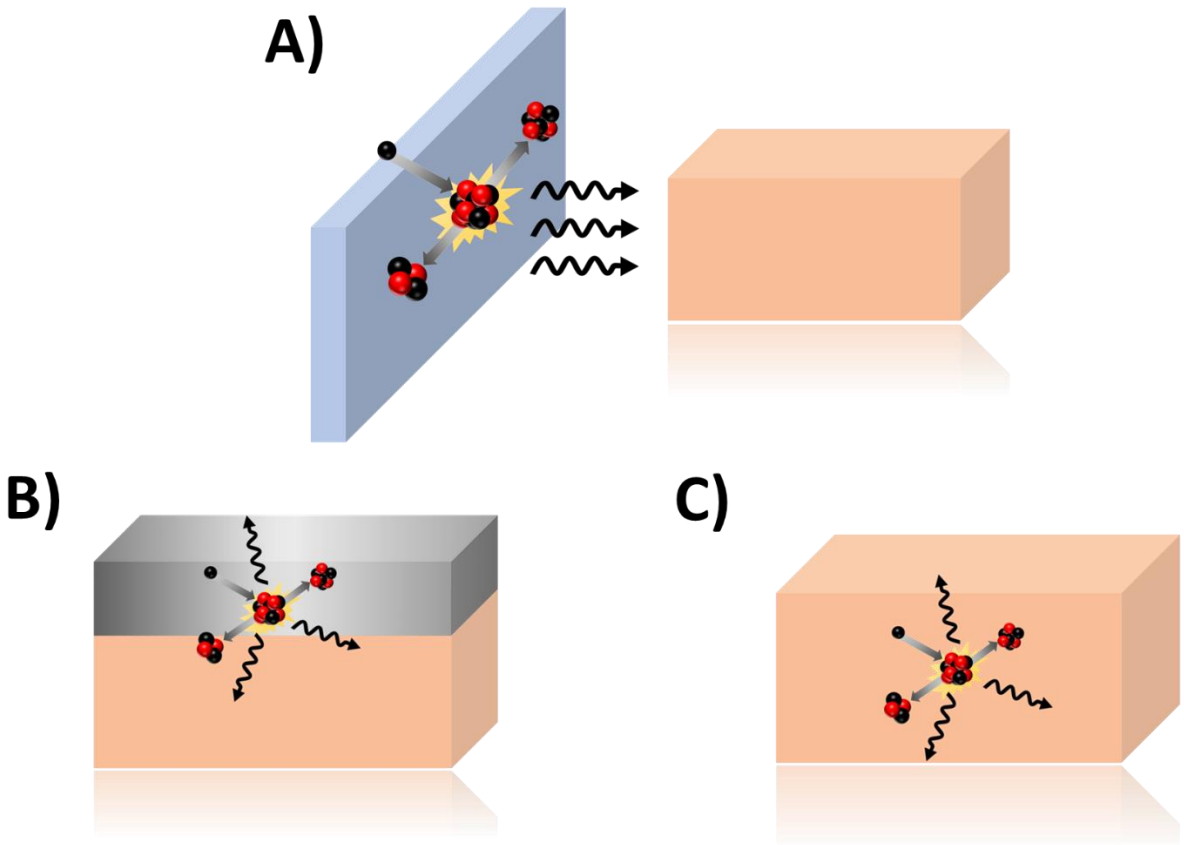

Figure 1.3.2. Reported methods of thermal neutron sensing with the thermal neutron sensitive isotope A) embedded in a sheet or foil to produce gamma rays that the detector can sense, B) within a heterojunction (not to scale) to produce charged particles that will deposit energy within the detector, and C) within the detector itself

gamma emitting sources of interest. Alternatively, conversion layers containing thermal neutron sensitive isotopes can be directly deposited onto semiconductor detectors, allowing for the detection of both secondary charged particles and gamma rays produced by the neutron capture, which is shown in Figure 1.3.2B. ^{10}B conversion layers have been used for both $CsPbBr_3$ thin film and $MAPbBr_3$ SC semiconductors, while Gd_2O_3 heterojunctions on $MAPbBr_3$ SCs have also demonstrated thermal neutron detection capabilities [71-73]. However, there are two primary limitations to using conversion layers. First, the short range of the secondary charged particles produced in the neutron reaction limits the conversion layer thickness, which in turn limits the thermal neutron *absorption efficiency* to approximately 11% [74]. Second, since the charged particles produced in the conversion layer by the neutron reaction are emitted antiparallel to each other, at most only one of the reaction products can reach the semiconductor bulk to produce electron-hole pairs and induce a response, which decreases the already low efficiency by at least half [4]. As a result, the maximum thermal neutron *detection efficiency* with conversion layers is limited to only 4-5% [75].

Given the drawbacks associated with these indirect conversion methods, it is desirable to incorporate thermal neutron sensitive isotopes into the detector medium for direct conversion as shown in Figure 1.3.2C. $MAPbBr_3$ SC semiconductors were shown to be capable of incorporating various objects into the crystal bulk during growth [76], which led to the embodiment of Gd_2O_3 pellets in the detector medium that allowed for thermal neutron sensitivity [68]. However, the grain boundaries produced through the heterogeneous incorporation of thermal neutron sensitive isotopes in this manner could lead to potential degradations in charge transport and detector performance [77, 78]. As a result, the incorporation of thermal neutron sensitive isotopes directly into the MHP structure could offer the greatest potential for high performing perovskite thermal neutron sensors. $(PEA)_2PbBr_4$ thin film scintillators doped with lithium have previously demonstrated direct conversion thermal neutron sensing and gamma/neutron discrimination [69, 70]. However, there remains a gap for low-cost, high resolution, and high efficiency dual gamma/neutron perovskite semiconductor detectors, as no reported perovskite SC semiconductors to date are capable of direct thermal neutron detection with the thermal neutron sensitive material incorporated into the perovskite structure.

X-ray Imaging with MHPs

In addition to gamma/neutron sensing for nuclear security applications, MHPs have also shown potential to meet the need for low-cost, large area, high stopping power semiconductor detectors for X-ray imaging. There have been a number of reports evaluating the sensitivity of solution grown 3D MHP SCs to X-rays already listed in Table 1.3.1, which has improved in recent years to range from 10^2 to 10^4 μC Gy^{-1} cm^{-2} [42, 43, 50-53, 62-64]. While the thicker SC detectors may provide better stopping power, higher efficiency, and allow for harder X-rays to be used in a greater variety of imaging operations, polycrystalline MHP films have been suggested to be the better fit for satisfying the large area requirement [79]. Shrestha *et al.* achieved polycrystalline 3D wafers that were 200 μm to 1 mm in thickness by sintering $MAPbI_3$ microcrystals with X-ray efficiencies on the order of mC Gy^{-1} cm^{-2} [49]. Meanwhile, Kim *et al.* printed polycrystalline $MAPbI_3$ films 830 μm thick that were able to resolve a hand phantom X-ray image with only a dose of 25 μGy, although a high dark current was also observed [13]. Continued development of large area polycrystalline MHPs for efficient X-ray detection and imaging require substantial improvements to both thickness and SNR, which will limit the dose required to take the radiograph, lower the cost of fabrication, and provide greater versatility for a wider range of imaging applications.

The notable achievements in sensing gamma rays, neutrons, and X-rays described in this section also highlight several areas in need of improvement for MHPs to become viable options for radiation detection and imaging, particularly when it comes to stability. Whether it is for nuclear security or X-ray imaging, detectors must be able to maintain a consistent and stable response during operation. The following section will discuss several areas where degradations to detector performance can originate, as well as reported efforts to mitigate the effects.

1.4. Current Challenges with Perovskites

Surface Passivation

High surface quality is required to mitigate carrier recombination at the MHP surface that can potentially cause polarization, detector instability, and detriments to the observed charge

transport properties. The surface recombination velocity (SRV) defines the carrier recombination in units of cm s^{-1}, and high SRV values are representative of charge carrier losses that lead to degradations in charge collection efficiency [17, 80]. As a result, significant effort has been dedicated toward understanding and minimizing recombination at the surface to improve detector performance.

Studies on CZT radiation detectors have previously demonstrated that neglecting surface recombination effects can contribute to significant discrepancies between the real and measured bulk electronic transport properties of single carriers [19, 81]. Since recombination and loss of charge collection efficiency occurs at the surface, failure to account for this effect results an underestimation of the true $\mu\tau$ values for carriers traversing the detector bulk. Accounting for surface recombination requires the use of the single polarity Many relation shown in Equation 1.4.1, which is identical to the Hecht relation previously described in Section 1.3 except for an additional term, where S is the SRV and can also be reported as S/μ [82].

$$CCE = \frac{\mu_h \tau_h E}{d}\left[1 - \exp\left(-\frac{d}{\mu_h \tau_h E}\right)\right]\left(\frac{1}{1 + \frac{S}{E\mu_h}}\right) \tag{1.4.1}$$

Significant effort has been dedicated to passivating MHP surfaces from electronic defects to minimize the SRV, suppress leakage current, and extend detector lifetime. For instance, the use of a guard ring that limits electronic noise from surface currents around the detector has been shown to suppress dark current by as much as fourfold, as well as increase the apparent resistivity [42]. Moreover, given that hydration and oxidation from the ambient environment are primary degradation mechanisms of MHP SCs [83, 84], various methods that create protective barriers have been evaluated such as epoxies [42, 85, 86], UV-ozone to oxidize the surface [50], conversion of the MHP SC surface into water-insoluble lead(II) oxysalts ($PbSO_4$ and $Pb_3(PO_4)_2$) [87], coating the SC with 2D Ruddlesden-Popper hybrid perovskite [88], and encapsulation with boron nitride flakes [89]. Several examples showing the effects of surface passivation on the SRV are shown in Table 1.4.1, which contains reported SRV values for $MAPbBr_3$ SC photodetectors. Wei *et al.* demonstrated that passivating a SC surface with UV-ozone led to an approximately 20-fold

Table 1.4.1. Reported SRV values for $MAPbBr_3$ SC photodetectors

MHP Composition	**S ($cm\ s^{-1}$)**	**μ_h* ($cm^2\ V^{-1}\ s^{-1}$)**	**S/ μ_h ($V\ cm^{-1}$)**	**Reference**
$MAPbBr_3$	4	206	0.02	[80]
$MAPbBr_3$	2200	201	10.95	[53]
$MAPbBr_3$**	1120 (No Passivation) 64 (With Passivation)	217	5.16 (No Passivation) 0.29 (With Passivation)	[50]
$MAPbBr_{2.94}Cl_{0.06}$	55	560	0.98	[42]

* μ_h determined via ToF methods
** Passivation with UV-ozone

reduction in SRV [50], while ultra-low SRV values were achieved by Fang *et al.* in SCs by modulating the physisorption of O_2 and H_2O molecules [80].

While passivation of electronic defects is significant, it is also known that carrier recombination tends to originate from physical defect sites on the surface [87]. As a result, the optimization of physical surface quality a critical objective in the fabrication of high-quality sensors. One of the most significant physical parameters to minimize is the surface roughness, which is commonly represented by the root mean square (RMS) roughness. Most of the reports of MHP surface roughness have been for thin films or very thin single crystals that do not require or are not suitable for physical polishing, which report RMS values on the range of nanometers to tens of nanometers through a variety of methods such as spatially confined inverse temperature crystallization growths [90] planar hot processing methods [91], the use of non-halide lead sources [92], spin coating and stamping with polydimethylsiloxane [93], and sol-gel processes [94] in order to remove shunting pathways, limit pinholes, and minimize scattering that would otherwise degrade photovoltaic performance. With large 3D MHP SCs, very smooth surfaces have been achieved as well, with reports demonstrating roughness values of 8.5 nm [95], 1-2 nm [96], and even sub nanometer roughness [97]. However, for MHP devices fabricated to be used for radiation detection purposes, limiting surface roughness becomes difficult considering that mechanical polishing is often an essential step for creating parallel surfaces in order to maintain a flat electric field profile, even though the mechanical polishing processes introduce microcracks, scratches, and other defects, which in turn lead to recombination centers on the surface that lower the observed charge collection efficiency. For instance, El Bouanani *et al* report $MAPbBr_3$ SC roughness values of 40.82 nm after processing with a polishing wheel which, while a significant improvement over their as-grown crystals that had roughness greater than 10 μm, was still significantly higher than the aforementioned SC roughness values [73]. On the other hand, the $MAPbBr_{2.94}Cl_{0.06}$ SC reported by Wei *et al.* was grown with exceptional quality and did not require physical polishing, which showed a low SRV of 55 cm s^{-1} and spectroscopic response to gamma rays as previously described in Table 1.3.1 [42]. These reported results demonstrate that improving upon the surface roughness is a critical objective toward minimizing the SRV, both by mitigating

the damage brought about by mechanical polishing as well as improving upon growth quality to eliminate the need for polishing altogether.

As previously discussed, properly prepared surfaces also enhance the quality of the detector-electrode interface. The following section will discuss the challenges associated with the electrode itself, and the need to ensure judicious selection of electrode material.

Electrode Engineering

In many studies utilizing MHP semiconductor SCs for radiation sensing, metallic electrode materials utilized have included chromium [42, 45, 57, 98], InGa [88], gallium [56, 99], gold [51, 56, 59, 64, 73, 100, 101], and silver [73, 100], while organic interfacial layers have included fullerene [42, 57, 87, 100, 102] and poly-TPD [100]. The selection of electrode material must consider a number of factors. First, the work function of the contact metal must be suitable in relation to the band structure of the semiconductor. The Fermi level of the metal is equal to the distance between the vacuum level and its work function. Since the valence and conduction bands of the semiconductor bend in order to match its Fermi level with the metal and create the Schottky barrier, the metal work function becomes a key parameter in determining the barrier height, which is essential for limiting the leakage current within the semiconductor device at equilibrium [103]. Second, the cost of the electrode material must be considered as well in order to keep fabrication costs low. For example, both gold and nickel have very similar work functions at 5.1 eV and 5.15 eV respectively. However, the latter has attracted interest as a potential replacement given the significantly lower cost. Additionally, lower Z materials are occasionally preferred in order to minimize the number of interactions taking place between the contact material and the incident radiation, although the contact thickness is usually sufficiently thin where these effects are negligible.

Another important set of considerations for electrode materials is their resiliency against phenomena that degrade detector performance. One such phenomenon is the natural diffusion of the perovskite to the metal contact and vice versa. The elastic properties and soft Pb-X lattice of MHPs make them defect tolerant, but also susceptible to mobile ion and charged impurity diffusion into the perovskite [104, 105]. Studies with $MAPbI_3$ and silver contacts have demonstrated that both the iodine and methylammonium ions can diffuse and accumulate at the Ag internal surface

to form an AgI barrier, which led to device destabilization [106]. Moreover, interfacial redox reactions that lead to the deposition of metallic lead within MHPs have been demonstrated to degrade device performance, even going so far as to transform anodic contacts into cathodes as well as diffuse into the perovskite itself [103, 107, 108]. Another phenomenon is the tendency of certain contact materials to the absorption of moisture and oxygen in ambient environments. Studies have shown that fullerene-based contacts are poor barriers against the ingress of moisture towards the hygroscopic perovskite, leading to performance degradations [109]. Finally, ionic conductivity can play a significant role in the degradation of device performance. It has been shown that in TlBr radiation sensors under bias, bromine ions have a tendency to drift and react aggressively with the anode. As a result, their migration results in electrochemical reactions and formation of bromine-metal complexes at the interface, which distort the electric field within the semiconductor and lead to additional degradations in performance [110].

In order to mitigate these detrimental destabilizing effects and effectively improve device lifetime and performance, p-type hole transport layers (HTLs) and n-type electron transport layers (ETLs) have been widely implemented in photovoltaic development. Ideally, these layers must have good electrical conductivity, suitable energy levels, low surface defect density, high transmittance, pinhole-free morphology, and be thermally stable to ensure efficient charge extraction from the perovskite with minimal losses or recombination [111]. While a wide range of materials have been shown to be good HTL materials and electron blocking layers, the choices for ETLs and hole blocking layers is more stringent. As previously stated, a significant amount of focus has been on organic ETL materials with promising performance results, although the materials have been shown to be expensive and unstable [112]. On the other hand, the incorporation of inorganic ETLs has shown potential in recent years for improving MHP device stability and performance. For example, metal oxides as ETLs have been shown to minimizing interfacial electrochemical reactions between mobile halide ions and metal electrodes within TlBr radiation detectors [110].

In summary, many of the phenomena that lead to performance degradations within MHP semiconductor radiation detectors occur at or in the vicinity of the semiconductor-electrode interface. As a result, the judicious choice of electrode and interfacial layers is a critical component

of the detector fabrication process toward mitigating these detrimental effects and enhancing performance and stability.

Radiation Damage

Detector hysteresis, often defined as the degradation of a device over time, is a well-documented phenomenon in perovskites [113]. In addition to the ionic conductivity induced polarization and electric field degradation at the electrode interface described in the previous section, radiation damage is another phenomenon to consider as a potential source of hysteresis within detectors operated within high radiation fields exposed to a continuous flux of radiation, such as imaging and space applications.

Radiation damage from other highly energetic particles such as protons, electrons, and neutrons has been investigated for the potential use of perovskite solar cells in space applications, as well as to determine whether characterization studies that utilize electron beams are inducing significant damage to the perovskite [114]. The results of these studies have been mixed, with reports of remarkable stability of perovskites to proton irradiation at doses of 10^{15} particles cm^{-2} (0.5 MeV protons) [115] and 10^{13} particles cm^{-2} (68 MeV protons) [116], while 1.5 keV electron beams induced significant damage between 10^{15} and 10^{17} particles cm^{-2} [117]. It was also demonstrated that atomic displacement from fast neutron irradiation formed permanent shallow traps, although these Frenkel defects could act as dopants to decrease leakage current [114]. Moreover, studies of radiation induced degradation in perovskite solar cells have shown that incident radiation can form deep-level trap states as well as induce the dissociation of weakly coordinated anions and cations that increases the rate of ion migration [117-121], which led to an increased focus on self-healing as a mechanism to extend the lifetime of perovskite devices for such applications [122-124].

For gamma and X-ray radiation damage, there have been a handful of reports for MHP thin film detectors, [125-128], while reports on SCs are even more scarce [129-131]. Yang *et al.* reported that $Cs_{0.05}FA_{0.81}MA_{0.14}PbI_{2.55}Br_{0.45}$ thin film solar cells were able to retain 96.8% of their initial power conversion efficiency after 2.3 Mrad of continuous ^{137}Cs gamma radiation, although this total dose was accumulated for over 1500 hours at a low rate of 4.2 mGy s^{-1} [128]. Boldyreva *et al.* demonstrated that a 42 mGy s^{-1} dose rate and a total dose of 500 Gy from ^{137}Cs in a variety

of MHP films resulted in significant photocurrent loses, which were attributed to phase segregations of halide-rich domains [125, 126]. Additionally, Yang *et al.* used a ^{60}Co dose rate of 0.5 Gy s^{-1} in $Cs_{0.03}FA_{0.945}MA_{0.025}PbI_{2.25}Br_{0.75}$ films and observed a decreased level of UV-vis light absorption beginning at 1 kGy of total dose, which was deemed to be due to phase transition as confirmed by XRD [127]. These results show that the effect of radiation damage is correlated with both the dose rate as well as the total accumulated dose, and these trends are not limited to thin films. Xu *et. al.* reported that $MAPbBr_3$ SCs exposed to 0.19 Gy s^{-1} from ^{60}Co saw a reduced transmittance and induce defects, decomposition, and even microcracks after 16.56 kGy of accumulated dose [130]. On the other hand, Gao *et al.* reported that $Cs_{0.05}FA_{0.95}PbI_{2.7}Br_{0.3}$ SCs exposed to 0.5 Gy s^{-1} from ^{60}Co were able to self-heal when stored in the dark below 2 kGy of accumulated dose. The detector damage beyond this threshold was attributed to material decomposition and ion displacement mechanisms such as ionic conductivity, which is characterized by slow response time, and Frenkel defects that increase dark current and decrease photocurrent [131].

Chapter 2: Methods

This section will present the growth, fabrication, testing, and post-processing methods utilized in the evaluation of MHPs as radiation sensors. The majority of results presented in this dissertation pertain to a specific OMHP variant, methylammonium lead tribromide ($CH_3NH_3PbBr_3$, $MAPbBr_3$, or MAPB). However, the fabrication and evaluation methods described were utilized in similar fashion for both fully inorganic MHPs and OMHPs, and as a result, both will be referred to as MHPs throughout this dissertation unless disambiguation is necessary.

2.1. Crystal Growth

Precursors for the growth solution were utilized as received, and the crystal growth technique applied for all crystals in this study was inverse temperature growth (ITC) [132, 133]. For pure $MAPbBr_3$ (MAPB) SCs, MABr (GreatCellSolar, 99+%) and $PbBr_2$ (sigma, 99.999%) were dissolved in N, N-dimethylformamide (DMF, Sigma Aldrich, 99.8% anhydrous) at a stoichiometric ratio of 1.2 to 1, respectively, for a 1 M solution of $MAPbBr_3$ precursor in DMF. The precursor solution stirred for 6 hours (or until a clear solution was achieved) at room temperature. The solution was filtered through a 0.2 μm PTFE filter and 2 mL of the precursor was displaced into a 25 mL glass vial. Crystals nucleated to full size after 4-5 days of slowly heating the solution to 75°C in an oil bath on a hot plate. All precursor solution preparation occurred in a glove box in an N_2 environment, while the filtering and growths occurred in an ambient environment. It was discovered that the curved bottom of certain vials resulted in the formation of concavities, as shown in Figure 2.1.1A. The features were removed through mechanical polishing out of necessity to ensure effective electrode deposition, which resulted in significant loss of crystal volume. Switching the growth container to flat bottomed cuvettes produced more uniform surfaces such as the one shown in Figure 2.1.1B.

The techniques described above were subsequently modified depending on the desired SC properties. $MAPbBr_{3-x}Cl_x$ SCs were prepared by stoichiometric substitution of MABr with MACl (Sigma Aldrich, 99%) while $Li_yMA_{1-y}PbBr_{3-x}Cl_x$ SCs substituted MABr with LiCl (Sigma Aldrich, 99%) along with the stoichiometric replacement of DMF with dimethyl sulfoxide (DMSO), both during the precursor solution preparation stage. Recrystallization as a means of purifying the

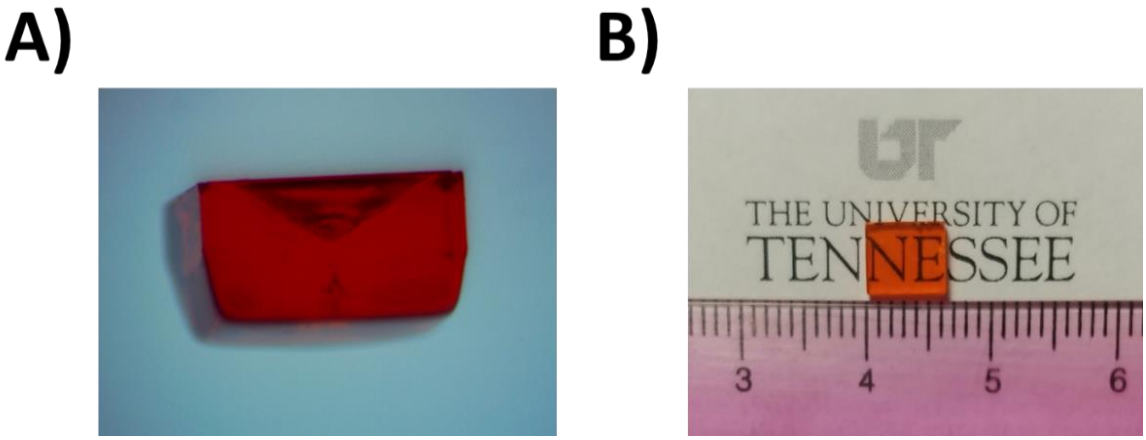

Figure 2.1.1. A) Side profile of $FAPbBr_3$ grown in a vial with a curved bottom showing significant concavity, B) Smooth crystal surfaces after growth

already grown SC was achieved by washing the SCs in dichloromethane (DCM, Sigma Aldrich, 99.8% anhydrous), followed by weighing and dissolving in fresh DMF solvent to produce a 1 M solution before repeating the filtering and growth process [58].

The precursor solution for polycrystalline $MAPbBr_3$ was prepared in the same way as previously described. The solution temperature ramped up rapidly to 70 °C to nucleate a cluster of small (~1 mm) crystals. These crystals were collected and placed into a fresh precursor solution at 50 °C with an open lid for the DMF to evaporate. As the DMF evaporated, the small crystals grew and fused together forming a crystal mosaic. The resulting monolith was a multi-inch freestanding wafer of MAPB and is shown in later in Figure 3.2.1. To disambiguate, it is important to note that the term "wafer" in this context refers to a 3D structure with a large surface area, and is not to be confused with other published work that uses the term to refer to 2D wide area thin films.

2.2. Detector Fabrication

Surface Processing

Mechanical polishing was conducted by hand using 1 μm diamond lapping pads until true rectangular parallelepipeds were achieved, which important to achieve a consistent electric field strength through the bulk. Chemomechanical polishing was then conducted with DMF on cellulose based paper for several seconds at a time to reduce the surface roughness, remove mechanical damage from previous polishing steps, and remove adventitious carbon, oxygen, and other unwanted impurities [134]. Detector dimensions were then measured either with a micrometer or via analysis with ImageJ software. Surface roughness values before and after DMF polishing were measured with a WYKO NT8000 white light interferometer [58]. Plasma cleaning was conducted in a Harrick Plasma Cleaner in an Ar/O_2 environment. The polycrystalline wafers were too brittle to be mechanically polished with lapping pads, and were instead lightly chemomechanically polished using DMF.

Electrode Deposition

Electrode design E1 from Chapter 3.3 was deposited via thermal evaporation with 60 nm of Cr on one face and 20 nm of C_{60}, 8 nm of bathocuproine (BCP), and 60 nm Cr on the opposite

face [45, 58]. The contact scheme utilizing SnO_2 was deposited via RF sputtering at the Micro-Processing Research Facility (MPRF) at the Institute for Advanced Materials and Manufacturing (IAMM). On one face of the SCs, a single 60 nm layer of Cr was deposited; on the other face 4 nm of SnO_2 was deposited and capped with 60 nm of Cr [58]. For the polycrystalline MAPB wafers, Cr deposited on both sides at a thickness of 50 nm via thermal evaporation on the parallel surface areas of the polycrystalline samples to allow carrier transport to occur through the detector bulk in the z-direction. Following electrode deposition, the fabricated detectors were stored in the dark under vacuum and ambient conditions.

2.3. Electronics

Fabricated devices were tested in a custom aluminum enclosure shown in Figure 2.3.1A that contained both the evaluation board and the preamplifier in order to limit the distance that the detector would have to traverse. A custom 3D printed radiation source holder resided beneath the evaluation board to keep an alpha particle source (usually ^{210}Po) separated from the detector by approximately 6 mm of air. Low temperature tests were conducted with the entire enclosure placed within a Tenney Test Chamber TJR-A-F4T.

Current-voltage (I-V) behavior was measured in a secondary enclosure without a preamplifier shown in Figure 2.3.1B, with a Keithley 6487 picoAmmeter supplying the voltage and measuring the resulting current. The voltage was incrementally increased from zero in both the positive and negative directions, and the slope of the combined dataset was taken as the resistance of the device if there was a consistent linear correlation. Resistivity (ρ) was then calculated with Equation 2.3.1, where R is the resistance while A and d are the surface area and thickness of the device respectively.

$$\rho = \frac{R \times A}{d} \tag{2.3.1}$$

The individual components of the analog pulse processing electronics are illustrated in Figure 2.3.2 and consist of a high voltage power supply (HVPS, NHQ 203M), charge sensitive preamplifier (CREMAT CR-110 or CAEN A1422 F2-90), shaping amplifier (ORTEC 572A or Canberra 2025), and a multi-channel analyzer (MCA) with discriminator (ORTEC ASPEC-927).

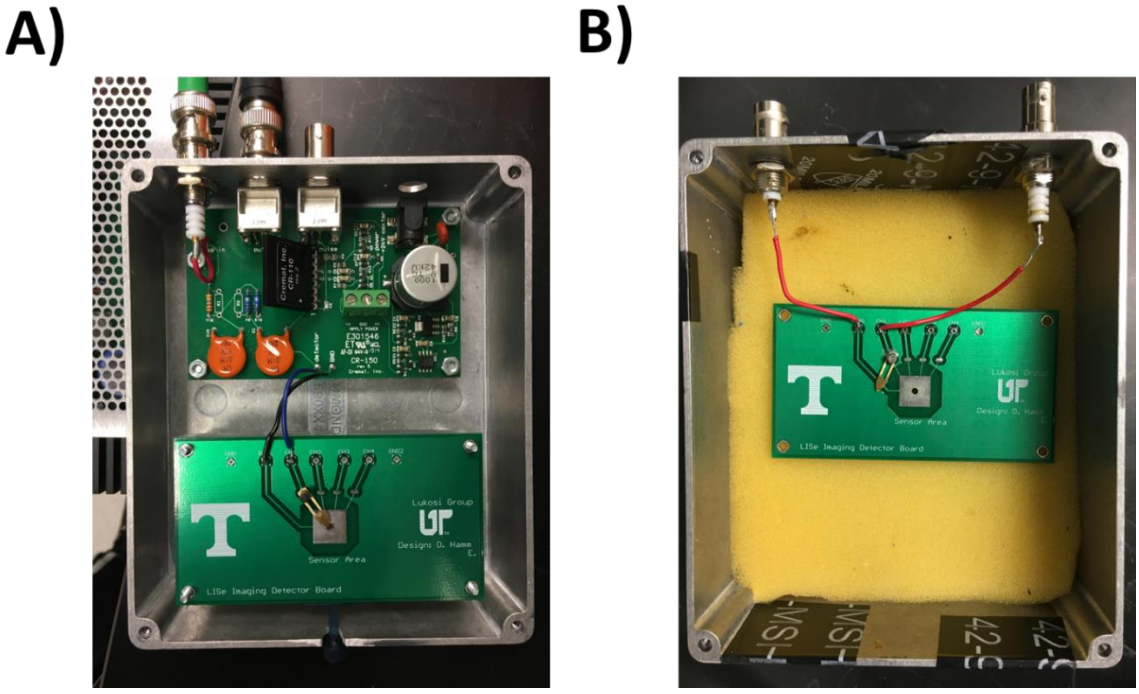

Figure 2.3.1. A) Custom enclosure containing the evaluation board and preamplifier, B) Secondary enclosure only containing the evaluation board

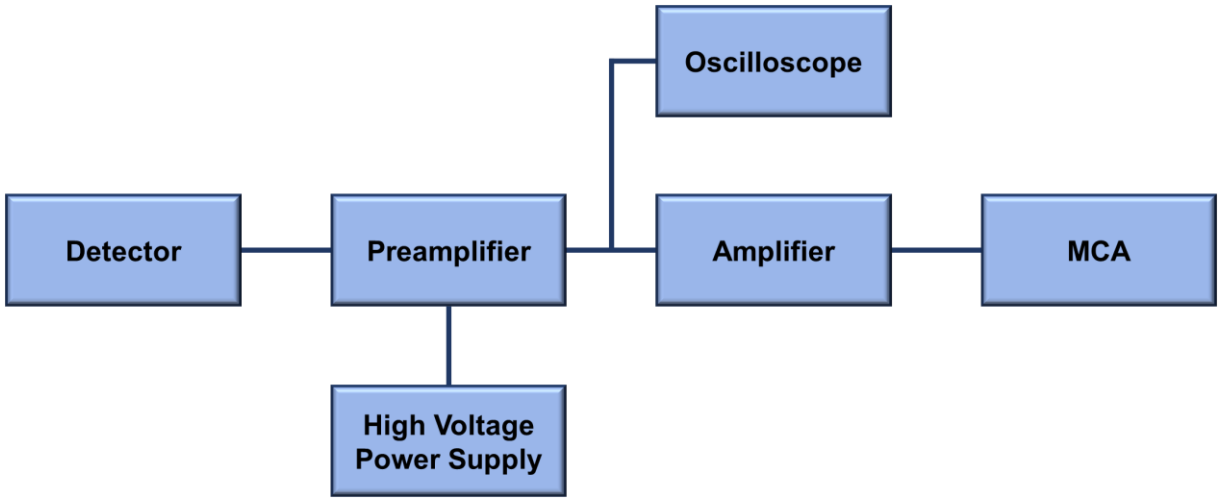

Figure 2.3.2. Pulse processing chain

The preamplifier output could also be read out into an oscilloscope (GW INSTEK GDS-3254 or Agilent 54845A).

The effect of the electronics on the radiation-induced signals become extremely significant when the charge carrier properties are both low and imbalanced, as is the case with MHPs and many other semiconductor materials. While spectroscopic degradation due to one carrier having a significantly lower $\mu\tau$ and drift length has already been discussed in Chapter 1.2, ballistic deficit becomes a significant issue when the dominant charge carrier has a low mobility. Ballistic deficit refers to the phenomenon where pulse processing electronics fail to register the complete signal from a radiation interaction due to an excessively long carrier drift time relative to the electronics, and can manifest in both the charge sensitive preamplifier as well as the shaping amplifier [45, 135-137]. Recall from Chapter 1.2 that the movement of charge carriers produced by the radiation interaction induces a charge on the electrodes based on the Schockley-Ramo theorem. The induced charge is induced over the carrier drift time, resulting in a current pulse that is the input to the voltage pulse produced by the charge sensitive preamplifier. The preamplifier has a decay time constant that is very long to minimize thermal noise contributions (CREMAT CR-110: 140 μs, CAEN A1422 F2-90: 150 μs), but still finite in order to avoid pulse pileup. The maximum amplitude of the preamplifier voltage pulse is shown in Equation 2.3.2, where V_m is the maximum voltage amplitude, i_d is the current pulse amplitude, RC is the decay time constant of the output voltage pulse (or preamplifier fall time), R is the resistance of the effective RC circuit, and T is the duration of the current pulse, which is related to the drift time of the carrier [137].

$$V_m = i_d R \left(1 - e^{-\frac{T}{RC}}\right) \tag{2.3.2}$$

In order to preserve spectroscopic information, the output voltage pulse V_m should be proportional to the true integration of the detector's output current, or total charge collected i_dT, which is also referred to as the ballistic signal [136]. However, V_m is only proportional to i_dT when $T<<RC$. As T increases relative to RC, the charge losses increase as well. This is not a significant issue in and of itself, as simple scaling corrections could be made during post-processing so long as the fraction of lost charge remains constant. However, when compounded with depth dependent

charge induction where *T* becomes variable, the charge losses from ballistic deficit also become variable with depth [137]. Mitigating these effects requires reconstruction of the ballistic signal and produce clean signal data without the poles from the preamplifier transfer function [45, 135].

Additional charge can be lost from the signal that passes the preamplifier due to the finite shaping time of the amplifier. Since the rise times of the preamplifier signals are also affected by the carrier drift, long drift times result in long preamplifier signal rise times that cannot be fully captured within the amplifier shaping time. Although the longest shaping times are typically on the order of 10 to 12 μs, a shorter shaping time is typically preferred in order to limit the dead time of the system. As a result, low mobility for the dominant carrier results in spectroscopic degradation on three fronts: variable charge losses in the preamplifier pulse height, incomplete charge integration within the shaping time of the amplifier, and potential limitations in count rate when the shaping time is increased out of necessity [136].

2.4. X-ray Sensing Setup

To evaluate the X-ray sensing capability of the two polycrystalline MAPB wafers (referred to as MAPB A and B), X-rays were generated with a MOXTEK® MAGPRO 60 kV (12 W) tube with a tungsten anode placed 0.5 cm away from the surface of the two MAPB detectors within the secondary enclosure as well as a diamond sensor for reference. The X-ray tube, which has a cone angle of 130°, was held at a constant operating voltage of 40 kV that produced a photon flux of 3.1×10^{11} photons s^{-1} sr^{-1} $100\mu A^{-1}$. According to the manufacturer, the flux scales linearly with the current to the X-ray tube [138].

Figure 2.4.1 shows the experimental setup with geometrically derived dimensions required to perform the calculations listed in Table 2.4.1. Equations 2.4.2-2.4.4 were used to calculate the total photon flux produced by the X-ray tube with the voltage set at 40 kV and a full opening angle of 130°. Since all 3 detectors (MAPB A, B, and Diamond) were smaller than the total beam area, Equation 2.4.5 was used to determine the cone angle to match the detector dimensions. The flux incident on the detector as a fraction of the total flux was derived with the calculated smaller cone beam angle and the flux intensity distribution. At a distance of 0.5 cm and a cone angle of 130°, the active sensing area of all three detectors were smaller than the cone area, resulting in 65%,

A)

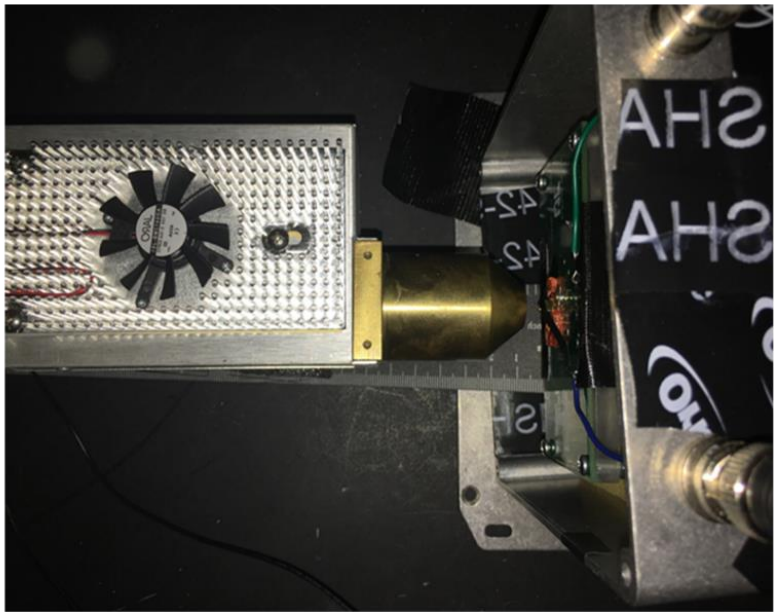

B)

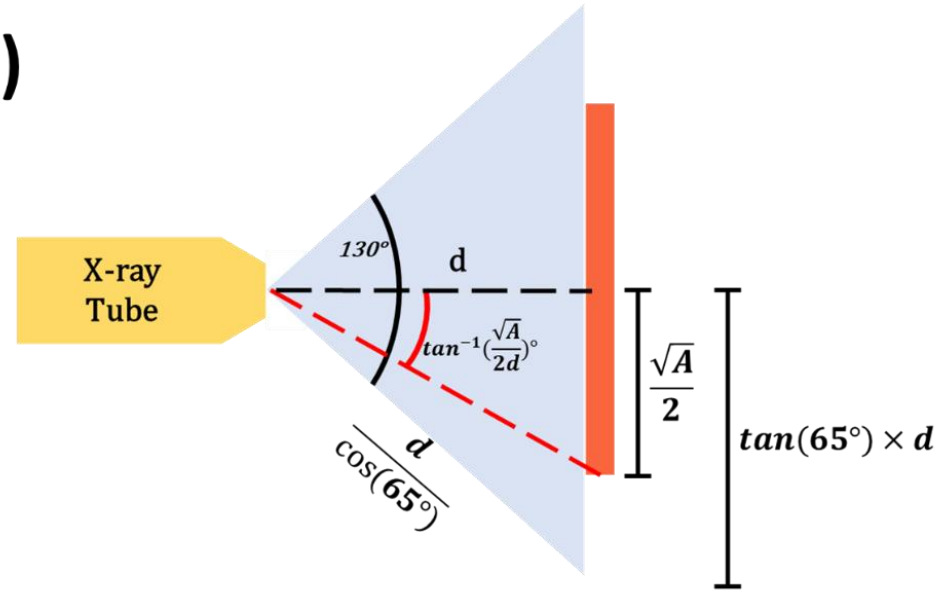

Figure 2.4.1. A) Experimental setup for X-ray irradiation of polycrystalline MAPB, B) Geometrically derived dimensions for X-ray irradiation on MAPB, where *d* is the distance from the X-ray tube to the detector and *A* is the area of the detector

Table 2.4.1. Equations to calculate incident photon flux on X-ray detectors

X-ray output @ 40 kV per manufacturer specifications	$3.1 \times 10^{11} \frac{photons}{s - sr - 100uA}$	(2.4.2)
Steradians with 130° cone angle	$1\ sr = \left(\frac{d}{\cos(65°)}\right)^2\ cm^2$	(2.4.3)
Full cone beam area for total X-ray output	$\pi[tan(65°) \times d\ ]^2 cm^2$ $= \pi[tan(65°)\cos(65°)]^2\ sr$ $= \pi[sin(65°)\ ]^2\ sr$	(2.4.4)
Cone angle for detector smaller than full cone beam area	$tan^{-1}(\frac{\sqrt{A}}{2d})°$	(2.4.5)

94%, and 92% of the total emitted X-rays striking the diamond, MAPB A, and MAPB B sensors, respectively [138]. These parameters were used to calculate the dose rates for each detector listed in Table 2.4.2. The average energy of the X-ray flux was calculated from the spectrum in Figure 2.4.2, which was a manufacturer provided spectrum of the X-ray tube with a tungsten anode at 40 kV collected by a CdTe detector. With the average X-ray energy calculated to be 12.67 keV, the flux of X-rays incident on the detector calculated from Equations 2.4.2-2.4.5, and the mass of each detector known, a dose rate could be estimated for all 3 detectors.

The induced photocurrent measurements from X-ray irradiation were carried out using a Keithley 6487 picoAmmeter. X-ray imaging was performed by using a stepper motor to move a brass key (66% copper, 34% zinc) to predefined grid positions (5 mm vertical and 2 mm horizontal steps) between the detector and X-ray source while keeping the detector and X-ray source stationary as shown later in Figure 3.4.2. The detector and X-ray source were separated by approximately 5 cm. At each key position, the induced current on the detector was recorded and used to produce a radiograph of the key. Radiation hardness experiments with $MAPbBr_{3-x}Cl_x$ SCs were conducted with the X-ray tube placed 0.5 mm from the Cr electrode, which ensured that the cone area was smaller than the surface area of the detector.

Table 2.4.2. Physical parameters for X-ray detectors

Parameter	Diamond	MAPB A	MAPB B
Thickness (cm)	0.05	0.34	0.25
Area (cm^2)	0.25	2.74	2.07
Density ($g\ cm^{-3}$)	3.50	3.58	3.58
Mass (g)	0.044	3.34	1.85
Dose Rate ($Gy\ s^{-1}$-100μA)	24.28	0.46	0.81
Mass Attenuation Coefficient @ 40 keV ($cm^2\ g^{-1}$) [139]	0.207	9.64	9.64
Thickness required to attenuate 99% of 40 keV X-rays (cm)	6.34	0.13	0.13

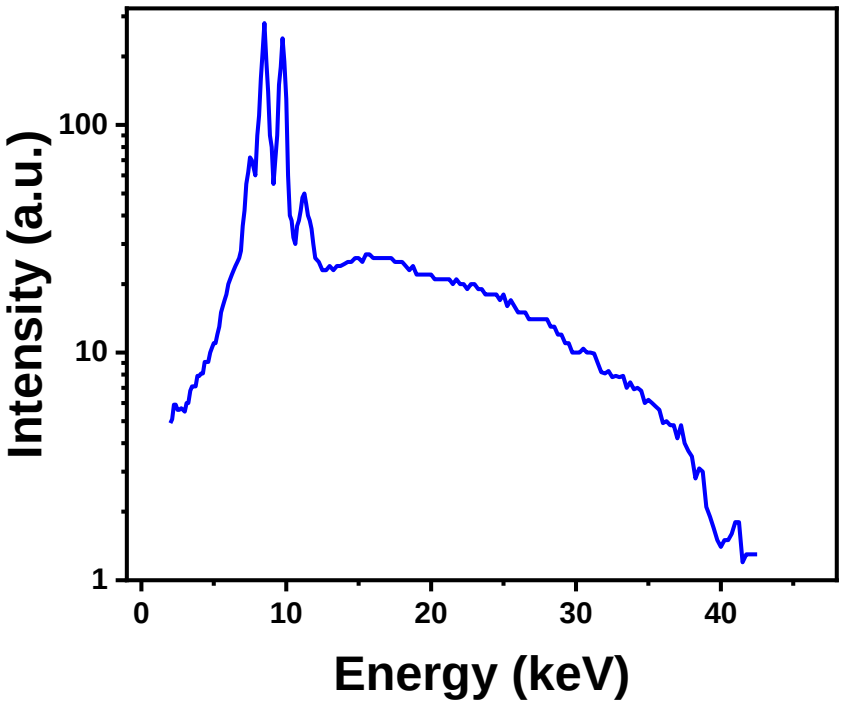

Figure 2.4.2. X-ray spectrum from a CdTe detector of a tungsten anode with an applied potential of 40 kV

Chapter 3: Results and Analysis

3.1. Characterization of Bulk Properties

This section presents the techniques utilized to characterize the physical and electronic bulk properties of the MHP detectors. The use of birefringence to rapidly screen for macroscopic crystal quality will be discussed, followed by several analytical techniques to verify the stoichiometry of the grown crystals. The final section in Chapter 3.1 will present methods for determining bulk charge transport properties of MHP detectors.

Birefringence

Characterization of bulk properties began with screening for quality by measuring the level of birefringence in a sample following polishing. Similar to techniques used to evaluate the quality of CVD diamond [140, 141], this method used cross polarized light to identify any physical defects or regions of strain within the bulk of the crystal. This concept is shown in Figure 3.1.1A, where no light passes through the second polarizer if it is positioned perfectly perpendicular to the first polarizer. By placing a crystal in between the polarizers crossed at right angles, any physical defects would cause light scattering and prevent the light from entering the second polarizer unperturbed and being eliminated. Meanwhile, the light would not be affected within defect-free areas of the sample and as a result, it would not be transmitted through the second polarizer.
Figure 3.1.1B shows a typical pattern observed in most MAPB and MAPB variant samples with features in the four corners that were hypothesized to be artifacts of the ITC growth process [132, 133]. It was observed that samples exhibiting similar patterns were likely to respond well to alpha radiation, while birefringence patterns that contained numerous and inhomogeneous defect regions such as the one shown in Figure 3.1.1D were indicative of samples that would respond poorly. While the sample in Figure 3.1.1D still responded to alpha particles, the discontinuity of the signal rise in Figure 3.1.1E was evidence of trap controlled conductivity (TCC), a phenomenon which occurs when trapped carriers stochastically de-trap through thermal excitations or externally applied electric fields, resulting in delayed charge collection [45, 142]. Ideally, when trapping has a minimal effect, the signal rise should be continuous, fast, and contain only one component

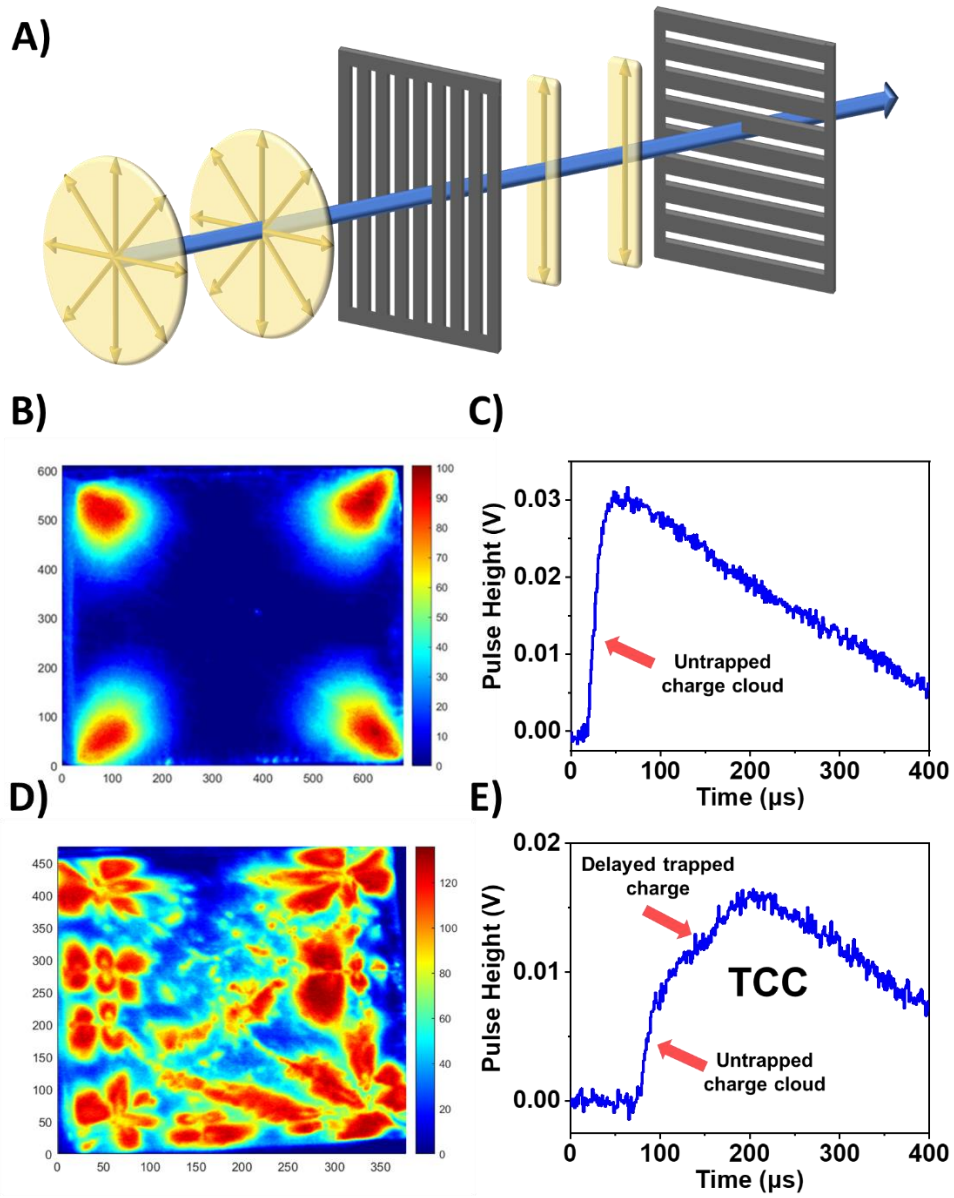

Figure 3.1.1. A) Cross polarization of light, B) Birefringence pattern of LiMAPB sample showing few defect regions, C) Alpha particle-induced pulse from LiMAPB, D) Birefringence pattern of a MAPB sample showing large amounts of defects, E) charge trapping and trap-controlled conductivity in the radiation induced pulse due to defects

corresponding to the transport of the untrapped charge cloud through the detector as shown in Figure 3.1.1C. The presence of TCC and lower pulse height observed in Figure 3.1.1E compared to Figure 3.1.1C indicated that the high concentration of physical defects observed through birefringence in Figure 3.1.1D could be correlated with a significant quantity of trap states. These results were the first reported use of birefringence imaging to pre-screen the quality of MHP SCs before fabrication as supported by the correlation of bulk quality to the observed radiation-induced transient signal, and established a simple and effective method by which the success rate of high-quality detector production could be improved.

Verification of Stoichiometry

As stated in Chapter 1.3, substitutions for the A-site cation and/or halide in MAPB have played an important role in improving radiation sensing performance [3, 42, 43, 99]. MAPB detectors presented in this work frequently have chlorine substituted for bromine during growth, while A-site substitutions have utilized cesium, lithium, and formamidinium. Since the stoichiometric quantities were substituted during the precursor solution preparation stage [58], it could not be assumed that the stoichiometric ratios initially selected were consistent with the stoichiometric ratios of the grown crystals. This section will describe the analytical methods used to verify incorporation of cations and anions at the desired concentration and site.

EDX

One method of determining the dopant concentration to compare with the intended stoichiometric ratios is energy-dispersive X-ray spectroscopy (EDX or EDS), which was performed on two 5% chlorine doped MAPB detectors, one standard and one recrystallized, to determine the chlorine dopant level. EDX is an analytical technique used to identify and quantify the elemental composition of a material by using an electron beam to excite and eject inner shell electrons of atoms near the surface. X-rays are then emitted as a result of an outer shell electron falling into the previously occupied core vacancy with energy equal to the difference in binding energy of the higher-energy shell and the lower. Since the energy levels of the shells are unique to the element, the intensity of the characteristic X-rays on the EDX spectra can be used to quantify

the elemental composition [143]. Figure 3.1.2 shows the EDX spectrum of the standard $MAPbBr_{2.85}Cl_{0.15}$, which contained the same characteristic peaks as the recrystallized sample. The notation ***L*** and ***K*** refer to the shell that the outer electron transitions to, while $\boldsymbol{\alpha}$ and $\boldsymbol{\beta}$ refer to a one shell and two shell transition respectively. By comparing the relative intensities of the peaks, it was determined that in the standard chlorine doped sample, the average chlorine substitution level was 5.7%, while the average level in the recrystallized sample was 16.5%.

ICP-OES

It is important to note, however, that EDX cannot detect elements below boron, and even elements such as carbon or nitrogen are difficult to distinguish within the spectra. As a result, while EDX is non-destructive and was useful for confirming chlorine substitution, verifying lithium incorporation in MAPB doped with 2.5% LiCl ($Li_{0.025}MA_{0.975}PbBr_{2.925}Cl_{0.075}$, or LiMAPB) for thermal neutron sensing required Inductive Coupled Plasma - Optical Emission Spectrometry (ICP-OES). which is a destructive analysis technique. ICP was performed by dissolving a LiMAPB single crystal into a mixture of DMSO and DMF. The new solution was compared to three standard solutions with different amounts of LiCl dopants, i.e., 1%, 2.5%, and 5%. From this, the percentage of LiCl incorporation of the LiMAPB crystal could be determined. The results of this study are listed in Table 3.1.1 and show good agreement between the experimental and theoretical predictions, thus confirming the incorporation of LiCl into the MAPB stoichiometry.

XRD

ICP spectrometry, however, is not capable of differentiating whether the detected lithium was residing in an interstitial site or if it was substituting for MA at the A-site. As a result, X-ray diffraction (XRD) measurements were performed on the LiMAPB SC that confirmed the A-site substitution of lithium into the crystal lattice. XRD can be a destructive or non-destructive analysis, and this study evaluated both methods by analyzing a MAPB and LiMAPB SC as grown as well as the crystals ground into polycrystalline powder. Figures 3.1.3A and B show the XRD pattern

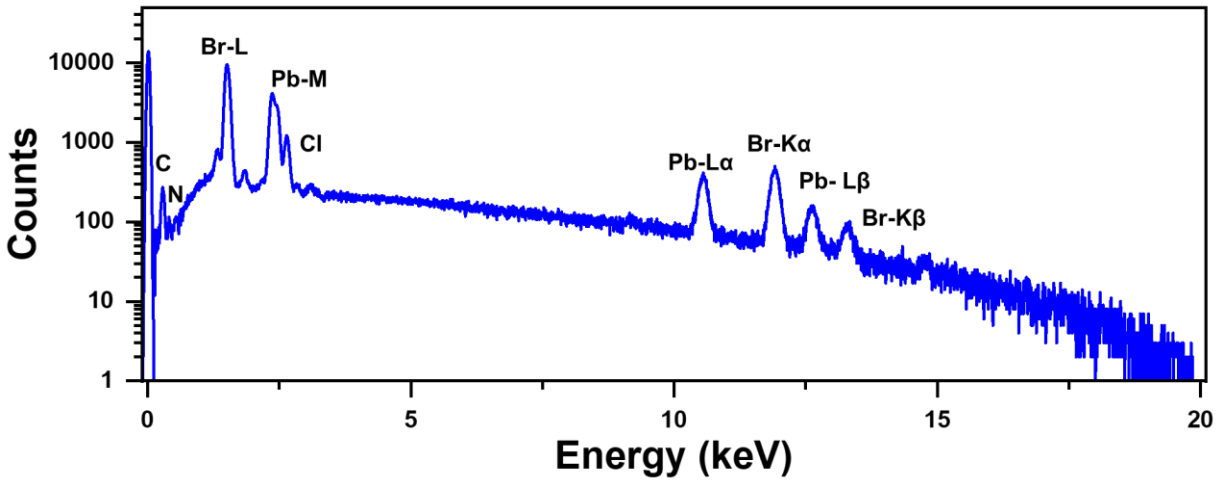

Figure 3.1.2. EDX spectrum of $MAPbBr_{2.85}Cl_{0.15}$ with peaks identified [144]

Table 3.1.1. Theoretical vs. experimental mass fractions for ICP-OES on LiMAPB SC

Element	Theoretical Mass Fraction (%)	ICP Mass Fraction (%)
Li	2.223	1.54 ± 0.94
Cl	11.353	10.89 ± 0.87
Br	25.590	24.96 ± 0.54
Pb	66.357	66.32 ± 0.82

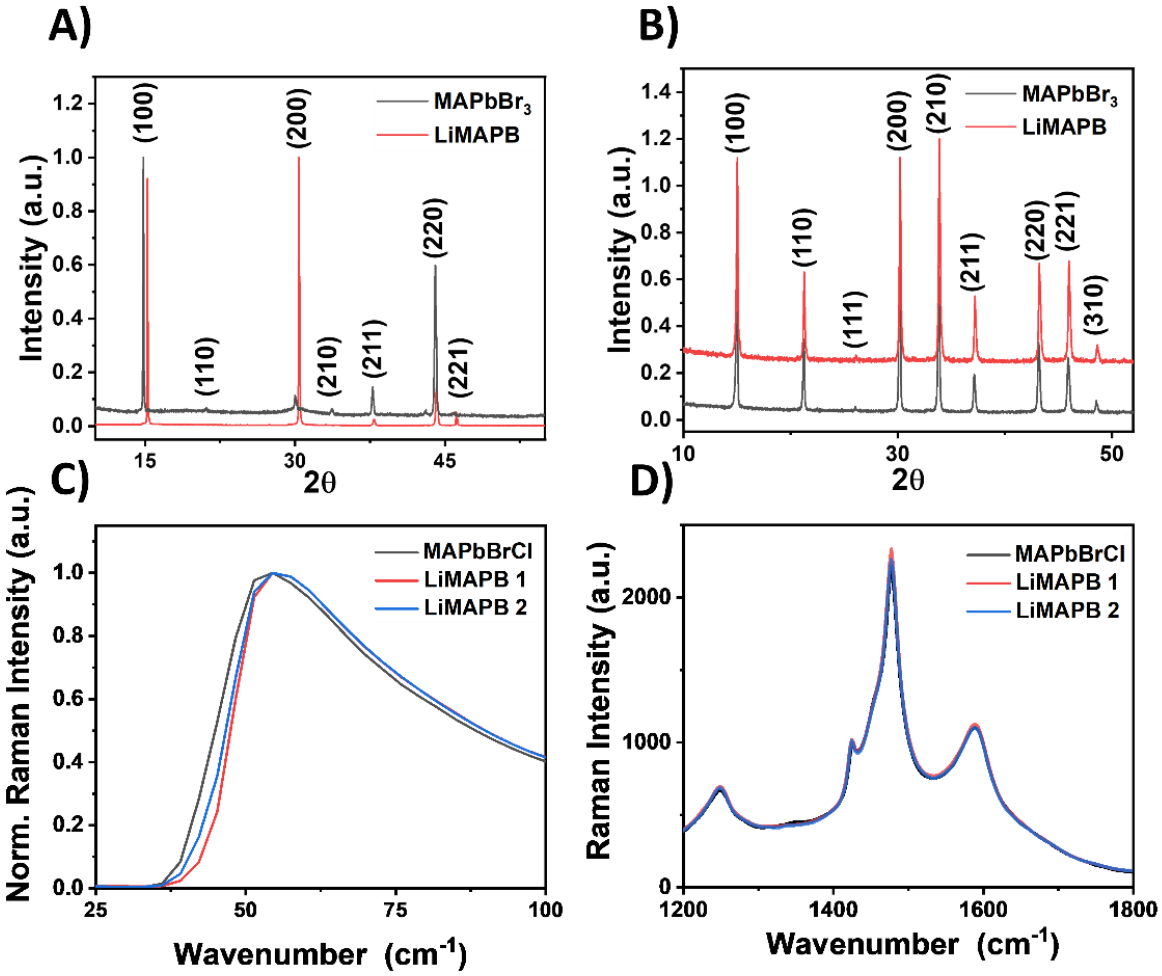

Figure 3.1.3. ***X-ray diffraction patterns*** **of A) $MAPbBr_3$ and LiCl-doped $MAPbBr_3$ single crystals and B) $MAPbBr_3$ and LiCl-doped $MAPbBr_3$ powder.** ***Raman spectra*** **for Cl and LiCl doped MAPB SCs showing C) a slight shift, indicating a shorter bond length at low wavenumber and D) no change to characteristic MAPB modes at broad range**

comparison between pure MAPB and LiMAPB single crystals, with Figure 3.1.3A showing SC diffraction patterns and Figure 3.1.3B showing the powdered samples. Overall, the patterns were similar except for a peak shift towards higher 2θ for the Li-doped crystals caused by the decrease of the lattice parameter from the smaller ionic radius of Li and Cl compared to CH_3NH_3 and Br respectively. These measurements collectively proved that lattice shrinkage was occurring due to LiCl doping, thereby confirming the successful A-site cation and X-site anion substitution into the crystal matrix.

Raman Spectroscopy

The XRD results alone, however, could not rule out the possibility that the observed lattice shrinkage was wholly due the smaller chlorine anions replacing bromine at the X-site. Comparison of Raman spectra with MAPbBrCl and two LiMAPB samples (labelled as LiMAPB 1 and LiMAPB 2 in Figures 3.1.3C-D) was able to further verify the A-site substitution of lithium into the crystal lattice. Here, MAPbBrCl refers to a SC with the stoichiometry $MAPbBr_{2.85}Cl_{0.15}$, making it a comparable crystal to LiMAPB ($Li_{0.025}MA_{0.975}PbBr_{2.925}Cl_{0.075}$). The low wavenumber Raman modes (<200 cm^{-1}) represented lattice vibrations, and shifting of the peaks indicated the effect that lithium had on the lattice [145]. Figure 3.1.3C shows a ~2 cm^{-1} shift to higher wavenumber following 2.5% LiCl incorporation, which was indicative of a shorter bond length. Since lattice shrinkage was still occurring despite the LiMAPB samples having a lower concentration of chlorine than the MAPbBrCl, it ruled out the possibility that chlorine in the X-site was the sole contributor to the lattice shrinkage observed in XRD and Raman, thereby verifying A-site substitution of lithium into the lattice. Furthermore, Figure 3.1.3D shows that lithium incorporation did not add to or change the characteristic MAPB Raman modes. Comparing LiMAPB to MAPbBrCl rather than pure MAPB ensured that the only difference in the chemical constituents was the addition of lithium, and the results indicated that LiMAPB could be grown with high crystallinity and no change in phase at a 2.5% doping concentration.

This section described several techniques utilized to verify the incorporation of select cations and anions. EDX, while non-destructive and capable of confirming chlorine substitution

levels, could not detect the presence of lithium. ICP was able to destructively confirm the incorporation of lithium, while XRD and Raman spectroscopy non-destructively confirmed the A-site substitution of lithium by analyzing the lattice shrinkage due to the smaller ionic radius of lithium compared to methylammonium.

Characterizing Charge Transport Properties

As previously discussed in Chapter 1.3, the trap states that inevitably exist within the detector result in an induced charge on the electrodes that is less than the charge deposited as predicted by the Schockley-Ramo theorem [21]. Instead, the CCE in compound semiconductors is dependent on $\mu\tau$ as indicated by the single polarity Hecht relation in Equation 1.3.1. By plotting the charge collected as a function of electric field, fitting the Hecht relation to the resulting curve would yield the $\mu\tau$ product for a detector [19, 48].

The mobility-lifetime product for each MAPB detector could be determined in two ways, the first of which is by sensing individual radiation quanta and plotting the charge collected as a function of electric field. Due to the poor electron transport properties in MAPB, it was desirable to use radiation with very short penetration depth to maximize the hole contribution to the induced signal, thereby ensuring that the maximum signal is consistently obtained (see Figure 1.2.2). As a result, ^{210}Po alpha particles were utilized to ensure that the detector operated in the space charge free regime with minimal trap passivation [39, 45, 54-58, 146]. Figure 3.1.4A shows the shifting alpha peaks as the bias voltage applied to a $MAPbBr_{2.85}Cl_{0.15}$ detector was increased from -10 V to -150 V in -10 V increments. When the average peak positions as determined via weighted average were plotted against the electric field, it can be seen that the data points in Figure 3.1.4B began to exhibit **1-*e*** behavior and approach an asymptote. This allowed for the Hecht equation to be fitted to the data points, which yielded an apparent $\mu_h\tau_h$ of 1.31×10^{-4} cm^2 V^{-1} [58]. The caveat to determining mobility-lifetime value with this method is that it does not take into account ballistic deficit, which the reason why it is referred to as apparent. As discussed in Chapter 2, ballistic deficit refers to the incomplete charge integration of the detector output signal due to long signal collection times relative to both the fall time of the preamplifier as well as the shaping time of the amplifier. The ballistic deficit becomes variable due to fluctuations in the signal collection time

from depth dependence of radiation interaction, low mobility, and TCC, which results in the deterioration of ballistic signal, or the proportionality of the signal amplitude to the total charge produced during the radiation interaction [135-137]. Since depth dependence is not a significant factor when sensing alpha particles, the signal collection time (as determined by the rise time of the preamplifier signal) is affected by the mobility as well as the presence of TCC which was shown previously in Figure 3.1.1. In a detector with sufficiently high hole mobility and limited TCC, the holes do not require a high electric field to reach their saturation velocity. Once the saturation velocity is reached, signals from alpha particles will yield a relatively narrow range of rise times, leading to a constant ballistic deficit that requires a simple scaling correction during post-processing. Under these conditions, the **1-*e*** behavior of the CCE curves may still be preserved, as was potentially the case for the $MAPbBr_{2.85}Cl_{0.15}$ detector in Figures 3.1.4A and B. In the case where the mobility is low and/or significant TCC exists, however, the radiation induced signal rise times are variable as a result of electric field dependent carrier velocities and/or stochastic de-trapping respectively. Under these conditions, the peak positions plotted as a function of electric field do not follow the **1-*e*** behavior required to perform a Hecht fit due to the signal losses from the preamplifier and the amplifier. This is illustrated by the alpha response from a $Cs_{0.01}MA_{0.99}PbBr_3$ detector in Figure 3.1.4C which was biased between -20 V and -200 V in -10 V increments. While charge collection continued to increase as the electric field increased, the linear behavior of an attempted Hecht fit in Figure 3.1.4D suggested that the use of alpha peaks collected at the end of the pulse processing chain was insufficient for determining $\mu\tau$ due to ballistic deficit.

Mitigating ballistic deficit required analysis of the alpha radiation induced preamplifier signal traces rather than the peaks in order to avoid the signal loss due to the finite shaping time of the amplifier. Preamplifier traces were collected from a $MAPbBr_{2.85}Cl_{0.15}$ detector (different from the $MAPbBr_{2.85}Cl_{0.15}$ from Figures 3.1.4A and B) biased between -10 V and -160 V in -10 V increments. Removal of the ballistic deficit was then achieved through a series of partial deconvolutions that reconstructed the charge distribution originally produced by the radiation interaction and simulated a true ballistic signal, thereby restoring the signal amplitude that was lost when the signal rise time was long relative to the fall time of the preamplifier. The deconvolution

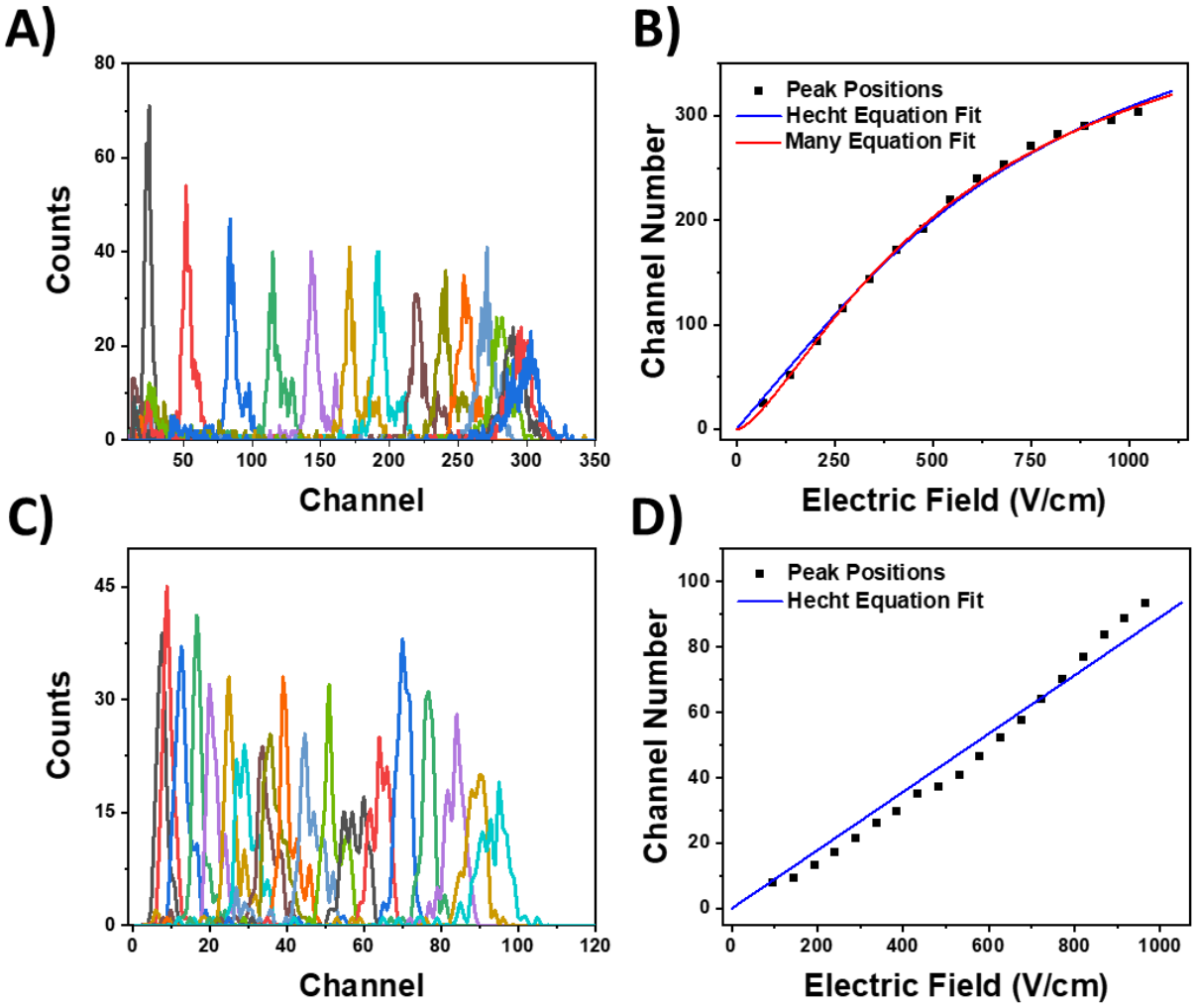

Figure 3.1.4. A-B) Hole response in a recrystallized $MAPbBr_{2.85}Cl_{0.15}$ detector with A) alpha spectra with detector biased between -10 V and -160 V in -10 V increments and B) corresponding CCE curve fitting using alpha peaks as a function of electric field. C-D) Hole response in a $Cs_{0.01}MA_{0.99}PbBr_3$ detector with C) alpha spectra with detector biased between -20 V and -200 V in -10 V increments and D) peak positions as a function of electric field unsuitable for CCE curve fitting

suppressed ballistic deficit effects and removed the single pole of the preamplifier transfer function as shown in Equation 3.1.1, where $V_c(i)$ is the preamplifier signal corrected for ballistic deficit, V_p is the uncorrected preamplifier signal, s is the sampling frequency of the oscilloscope, and τ_p is the fall time of the preamplifier [45, 135, 136]. Figures 3.1.5A and C show the unaltered and deconvolved alpha particle induced signals at -30V and -140V respectively, while Figures 3.1.5B and D show the initial rise of the same traces respectively on a logarithmic ordinate. Within the low voltage traces, there was evidence of TCC and detrapping, both in the continuous rise of the deconvolved signal beyond the end of collection in Figure 3.1.5A as well as the discontinuation of the rise from the unaltered signal that extended beyond 100 μs in Figure 3.1.5B. These features were not observed with a higher applied bias as seen in Figures 3.1.5C and D, which indicated that the trapped charge did not contribute to the primary signal with a higher electric field. Further evidence demonstrating the effect of ballistic deficit on charge transport properties is shown in Figure 3.1.6A, which plots the maximum amplitude of both the deconvolved traces as well as the raw traces as a function of the applied electric field. The lower biases were not included in the Hecht fit, since Hecht fitting cannot be performed with significant charge detrapping [19, 45]. Attempting to fit the Hecht equation to the maximum amplitudes of the raw traces yielded a linear trend rather than **1-*e***, which was previously shown to be due to ballistic deficit and indicated that Hecht fitting with this data was not appropriate for determining the mobility-lifetime product. Once the traces were deconvolved, however, the signal amplitudes were significantly higher and exhibited **1-*e*** behavior, which allowed the data to be fit to the Hecht equation and yielded a $\mu_h\tau_h$ of 1.06×10^{-4} cm^2 V^{-1}. The MAPB $\mu_h\tau_h$ values are consistent with other reported values for MAPB obtained via alpha particle irradiation [45, 57-59], and the results from Figures 3.1.4 and 3.1.5 collectively demonstrate the importance of improving the mobility of holes in MAPB and reducing the trap density to mitigate TCC.

$$V_c(i) = V_p(i) + (1 - e^{-\frac{s}{\tau_p}}) \sum_{j=0}^{i=1} V_p(j) \tag{3.1.1}$$

Following calculation of the mobility-lifetime product using the Hecht equation, the mobility was calculated through trace analysis by determining the rise time of the alpha radiation

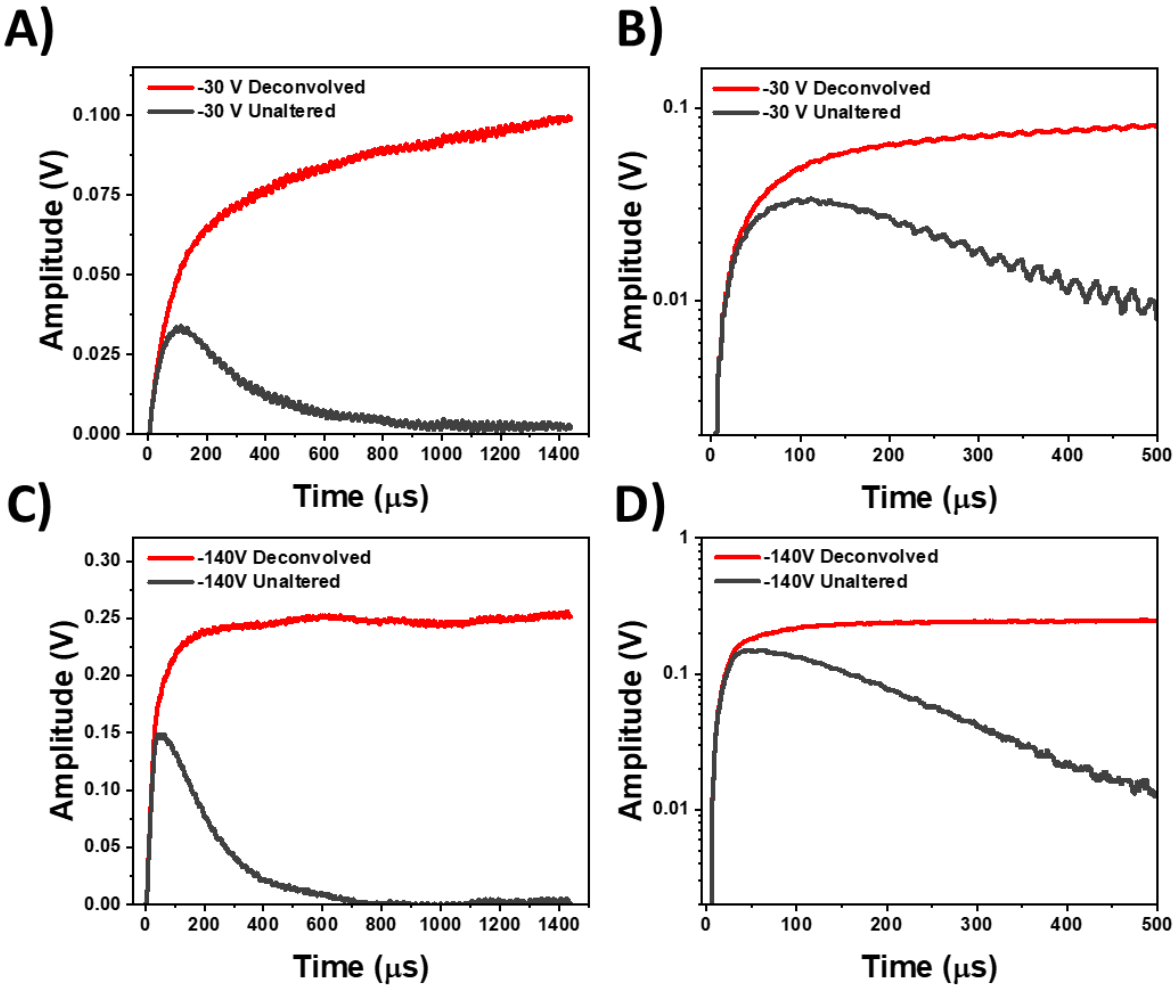

Figure 3.1.5. Raw and deconvolved alpha particle induced preamplifier traces collecting holes in $MAPbBr_{2.85}Cl_{0.15}$ at A) -30 V, B) -30 V with focus on the rise, C) -140 V, and D) -140 V with focus on the rise

induced signal from the time needed to rise from 5% to 95% of its maximum amplitude. Using the 5% to 95% rise time was necessary in order to mitigate any inaccuracies caused by fluctuations in the signal due to noise. The use of alpha particles for this purpose was particularly advantageous. As previously shown in Figure 1.2.2, placing the alpha radiation source near the anode ensured that the electron-hole pairs were generated very close to the non-collecting electrode due to the high energy deposition rate of alpha particles. Because the holes must traverse the entire bulk of the detector to reach the collecting electrode in MAPB, the velocity of the particle could be determined by dividing the thickness of the detector by the rise time of the signal. This method could be used for both holes and electrons as long as the collected carrier is generated as far from the collecting electrode as possible.

At this point, the mobility could be determined by one of two ways. The first was through single trace analysis by dividing the carrier velocity by the electric field applied using Equation 3.1.2 where μ is the carrier mobility, v is the velocity, E is the electric field, d is the thickness of the detector, V is the applied bias voltage, and t is the rise time of the signal [58]. This method, though simple, required that the carriers be below the saturation velocity in order to avoid undervaluing the mobility. As shown in Figure 3.1.6B, a more accurate method of determining the mobility could be utilized by plotting carrier velocity against the applied electric field and finding the slope of the linear portion of the curve prior to reaching the saturation velocity. This yielded a mobility of 4.25 $cm^2\ V^{-1}\ s^{-1}$ for the $MAPbBr_{2.85}Cl_{0.15}$ detector from Figures 3.1.5 and 3.1.6A, which is similar in order of magnitude to other reported values using space charge limited current methods or Hall measurements [45, 146], while also being significantly lower than time-of-flight (ToF) techniques, which is potentially due to the trap passivation that occurs in ToF [50]. The mobility value along with the previously determined $\mu_h\tau_h$ of 1.06×10^{-4} $cm^2\ V^{-1}$ resulted in a hole lifetime of 24.9 μs, which was in agreement with values reported using similar methods [45].

$$\mu = \frac{v}{\vec{E}} = \frac{d^2}{V * t} \tag{3.1.2}$$

The second group of methods to determine the charge transport properties is via photoconductive methods, which use a continuous flux of radiation to induce a stable current that

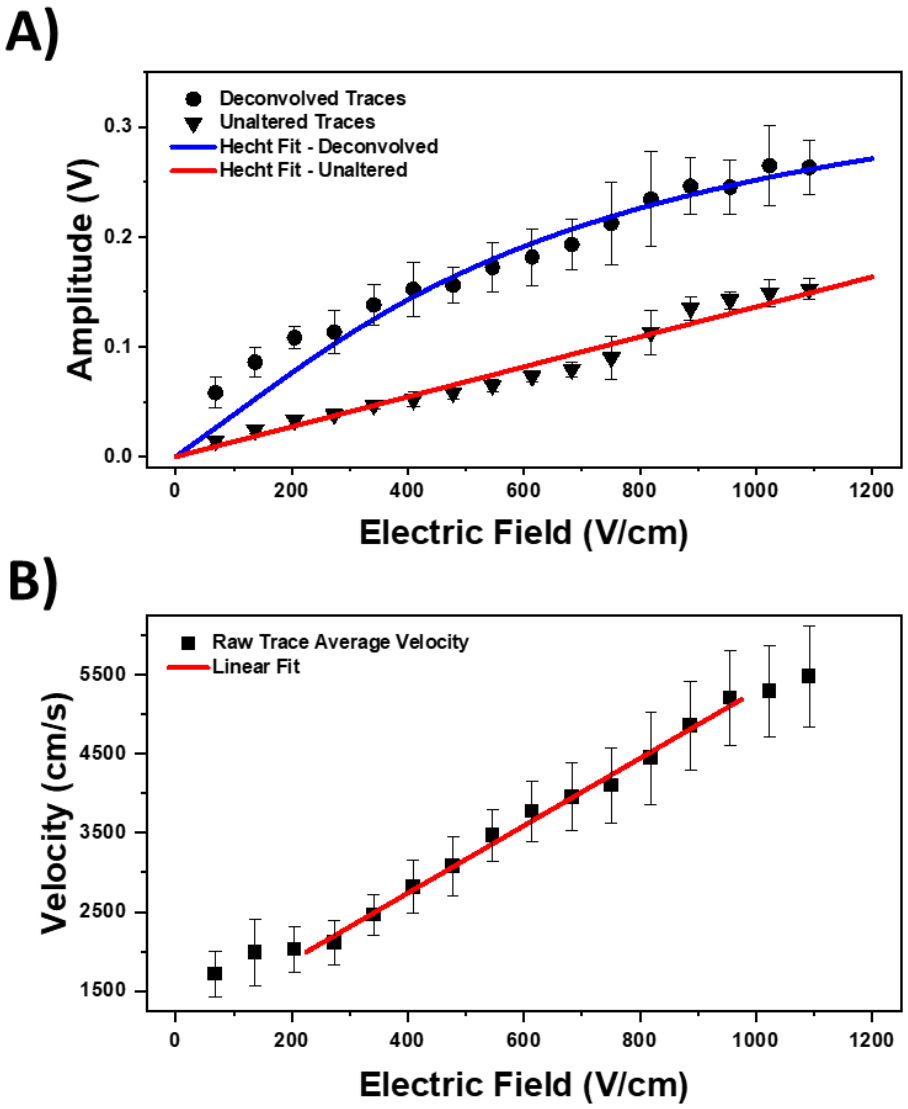

Figure 3.1.6. A) Maximum amplitude of raw and deconvolved traces from $MAPbBr_{2.85}Cl_{0.15}$ as a function of electric field along with an accurate Hecht fit for the deconvolved traces and an inaccurate fit for the raw traces, B) Velocity as a function of electric field in $MAPbBr_{2.85}Cl_{0.15}$, with a fit to the linear region to determine mobility

can be plotted as a function of the electric field. As stated in Chapter 1.3, the radiation is typically produced via X-rays or a continuous light source [42, 43, 47, 49-53], and previously reported $\mu_h\tau_h$ values for methylammonium lead halide single crystal detectors using these methods are on the order of 10^{-2} cm^2 V^{-1} while single quanta sensing methods report $\mu_h\tau_h$ values on the order of 10^{-4} cm^2 V^{-1}. As previously mentioned, the reason for the difference in order of magnitude is that the high event rate in photoconductive methods passivate traps which result in higher $\mu_h\tau_h$ values that would not be an appropriate characterization of charge transport properties for low count rate environments, though still useful for high event rate applications. This method was used to characterize two minimally polished 3D polycrystalline MAPB wafers (referred to MAPB A and B in this section) to evaluate their X-ray imaging capabilities. Exposing the detectors to a tungsten anode X-ray tube at a 40 kV potential while applying bias voltages between -2 V and -400 V yielded $\mu_h\tau_h$ values of 3.9×10^{-4} and 2.2×10^{-4} cm^2 V^{-1} for MAPB A and B respectively as show in Figures 3.1.7A and B. These values are several orders of magnitude lower than previously reported $\mu_h\tau_h$ values for methylammonium lead halide perovskite SCs obtained via photoconductive methods [42, 43, 49, 51, 52]. Instead, the order of magnitude for the $\mu_h\tau_h$ values more closely resemble those acquired via alpha particle irradiation [45, 57-59]. This discrepancy can be attributed to the recombination of carriers at the surface due to defect sites from surface inhomogeneities that trap the carriers and decrease the apparent charge collection efficiency [19, 42, 50, 58, 81]. The effect of surface quality in limiting surface recombination will be described in the following section.

3.2. Improving Surface Quality

As discussed in Chapter 1.4, high surface quality is desired in single crystal detectors to mitigate charge carrier traps from broken or strained bonds and impurities, as well as ensuring a homogenous connection between the detector surface and the electrode to maintain a constant electric field profile within the single crystal [19, 58, 147]. An extreme example of poor surface quality can be seen in Figure 3.2.1, which show the two polycrystalline MAPB detectors used to generate the photoconductive CCE curves in the previous section. The polycrystalline nature of the MAPB wafers coupled with the inability to perform mechanical polishing due to their brittle

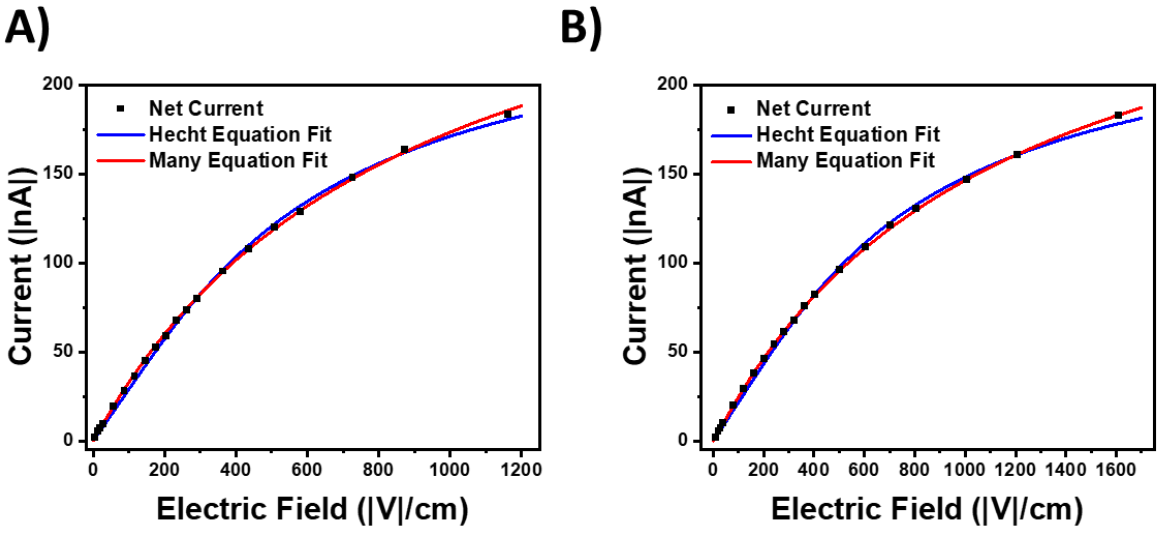

Figure 3.1.7. Hecht and Many fits for X-ray induced current as a function of electric field in 3D polycrystalline MAPB wafers A) MAPB A and B) MAPB B

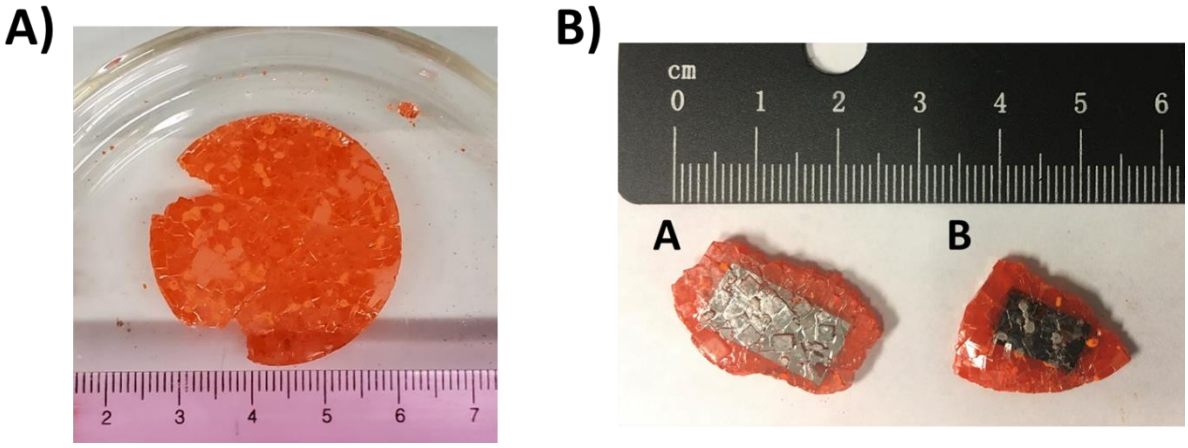

Figure 3.2.1. A) Harvested polycrystalline MAPB monolith with a diameter of 3.5 cm, B) Two detectors fabricated from the monolith

nature resulted in inhomogeneous detector surfaces that could be observed visually as shown in Figure 3.2.1B. The physical inhomogeneity also resulted in position-dependent electronic behavior, as I-V measurements from 0 V to ±80 V in ±10 V increments at three different points on MAPB A and MAPB B showed markedly different I-V characteristics depending on the position as shown in Figure 3.2.2. Three I-V measurements were taken at each position to potentially observe hysteresis. The I-V curves showed a dependence of the readout pin location on the observed curve shape (Schottky or Ohmic) and different dark current levels at a given bias, which indicated that the contact characteristics were not uniform across the surface of the MAPB mosaic wafers [19].

As previously described in Chapter 1.4, high quality surfaces are required in order to mitigate the effects of charge carrier recombination at the surface trap sites that decrease the observe charge collected and increase the surface recombination velocity. From the CCE curves in Figure 3.1.7, the $\mu_h\tau_h$ values from the Hecht equation fit obtained for the polycrystalline MAPB detectors via photoconductive methods were several orders of magnitude below reported values in methylammonium lead halide perovskite single crystals [42, 43, 49, 51, 52]. However, fitting the same data to the single polarity Many equation (Equation 1.4.1) yielded $\mu_h\tau_h$ values of 6.1×10^{-2} and 3.4×10^{-2} cm^2 V^{-1} for MAPB A and B respectively, with the former being the highest reported values in methylammonium lead halide perovskites. The S/μ_h values were determined to be 887 and 1112 V cm^{-1} for MAPB A and B, respectively, which are 3-5 orders of magnitude greater than those reported in Table 1.4.1 and indicated that the $\mu_h\tau_h$ values obtained via the Hecht equation were low due to high levels of recombination occurring at the surface. The inconsistent I-V characteristics and significant underestimation of $\mu_h\tau_h$ values in the unpolished polycrystalline MAPB detectors demonstrated that producing high quality surfaces is a critical component of single crystal detector fabrication.

DMF Polishing

While single crystal detector fabrication typically began with mechanical polishing after growth to ensure that the electrode surfaces are parallel and uniform, the polishing process itself, which used 1 μm diamond lapping pads to achieve the desired shape, could introduce microcracks, scratches, point defects, and overall roughness on the order of microns. To remove these effects

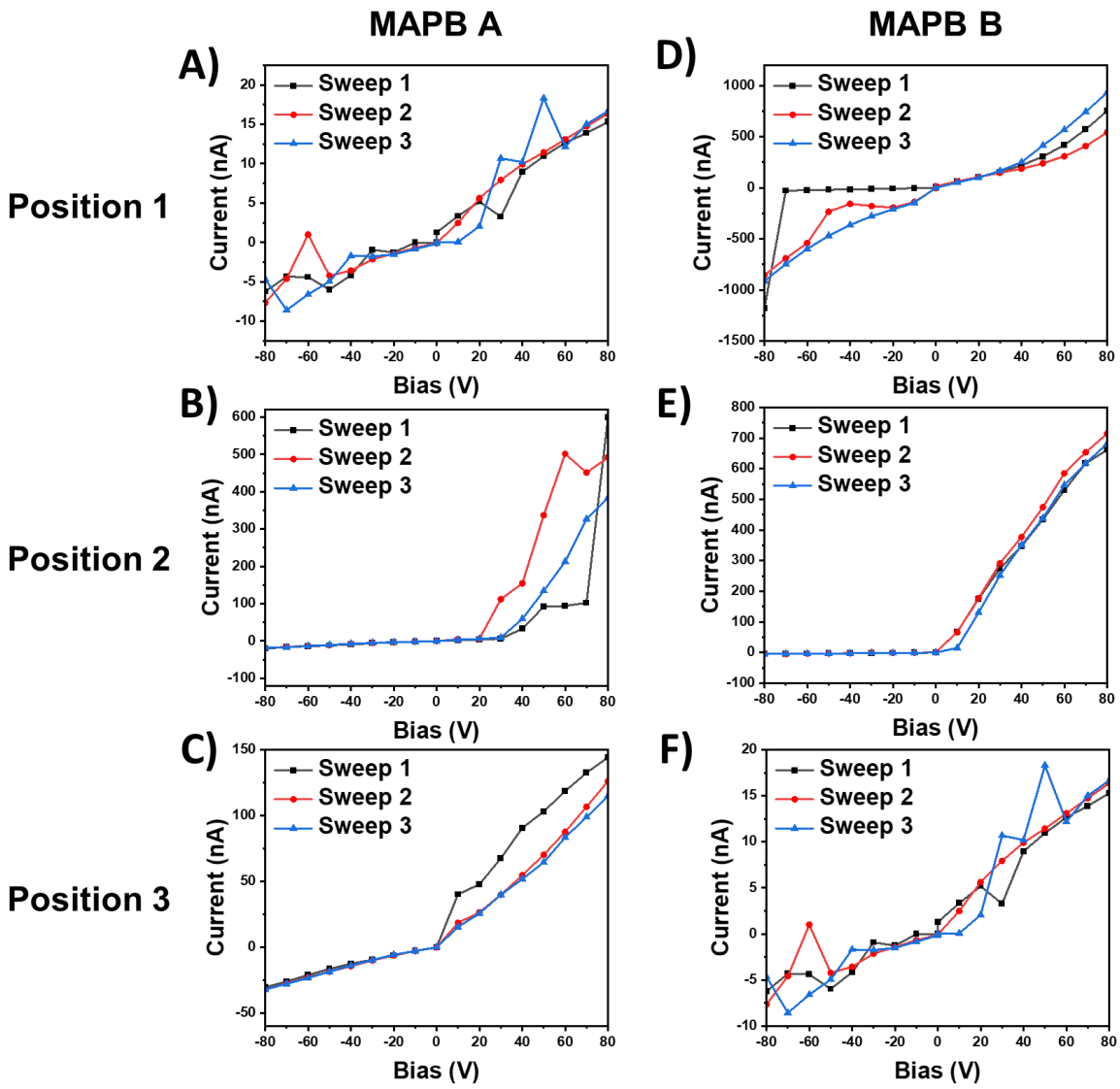

Figure 3.2.2. I-V Curves at 3 different locations on each polycrystalline MAPB detector. "Position #" refers to the first, second, or third position measured, and there is no correlation between the left and right columns of figures

and achieve a more pristine finish, a chemomechanical polishing process using DMF was implemented as a finishing step following mechanical polishing [58, 134]. The optical images of a MAPB SC surface before and after DMF polishing in Figure 3.2.3 show the removal of cracks and scratches which can be visually observed. These physical improvements were further verified by profiling the detector surface with a white light interferometer. Prior to the surface treatment, the mechanically polished crystal surface had an average root-mean-square (RMS) roughness value of 413 nm. Following the DMF surface treatment, the RMS roughness reduced by nearly fivefold down to 84 nm, indicating that the physical quality of the surface had been significantly improved [58].

In addition to improvements to the physical surface quality, the DMF polishing was effective in increasing the carrier lifetime. As previously described, poor surface quality can lead to a lower observed carrier lifetime due to trap states at the surface that serve as recombination centers [81]. The time-resolved photoluminescence (TRPL) spectra in Figure 3.2.4 show a faster carrier decay time following mechanical polishing as compared to the decay time after growth and prior to polishing. Although mechanical polishing was still a necessary step, the TRPL spectra indicated that it did indeed introduce defects that acted as trap sites for carriers, leading to a shorter PL lifetime. After DMF polishing, however, the slower decay time indicated that at least non-radiative recombination centers on the surface had been reduced. Because MAPB is a direct bandgap semiconductor, the TRPL results suggested a reduction in trap states that can be correlated with the fivefold reduction in RMS surface roughness [58].

Further, the detector response after chemomechanical polishing was dramatically improved both in apparent charge collection efficiency as well as stability. Figure 3.2.5 shows the comparison of the alpha response from three $MAPbBr_{2.85}Cl_{0.15}$ samples that were tested before and after chemomechanical polishing, with the samples referenced as Sample A, B, and C. The applied bias voltage, which is provided in Table 3.2.1, was increased in -10 V increments for each detector. Prior to chemomechanical polishing, the three samples were unstable at bias greater than -90 V as shown in the spectra taken prior to DMF polishing, and showed evidence of electrical breakdown beyond these voltages. Following chemomechanical polishing, an apparent increase in the charge collection efficiency by as much as a factor of 4 was observed due to the enhanced bias stability,

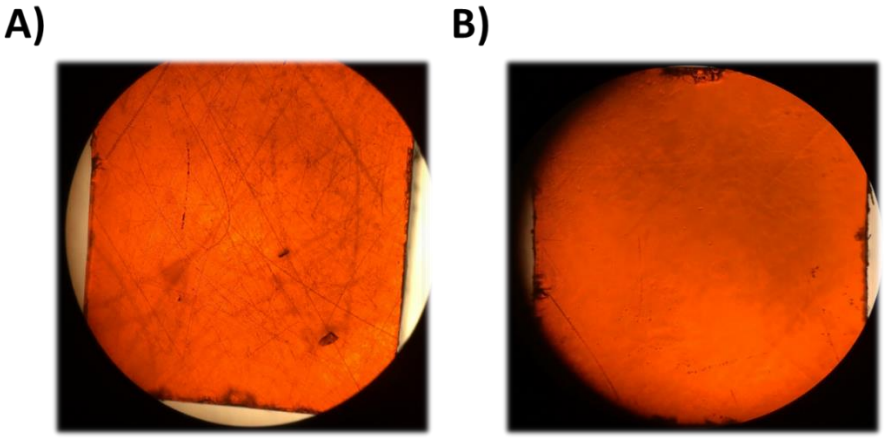

Figure 3.2.3. Optical images of a MAPB crystal surface A) before DMF polishing, and B) after DMF polishing

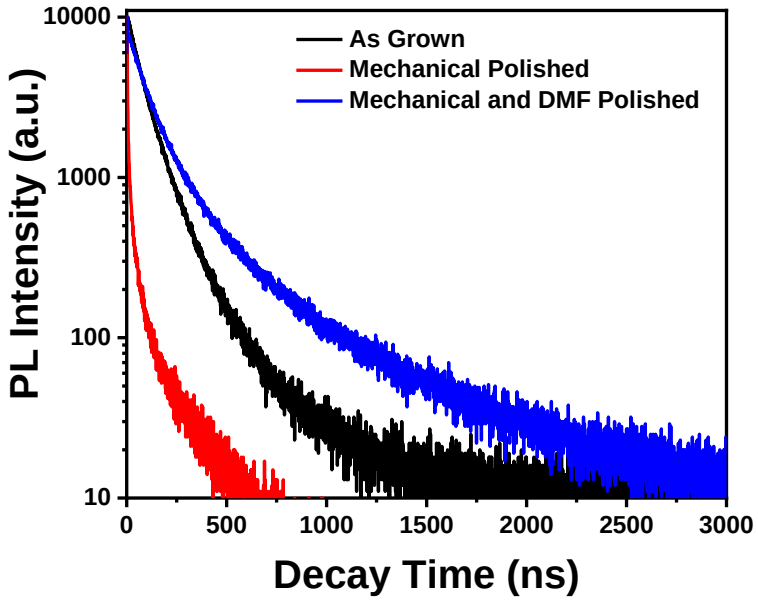

Figure 3.2.4. TRPL spectra of MAPB crystals before, and after mechanical and chemomechanical polishing. The slower decay time suggests an increased carrier lifetime following DMF polishing, while samples that were only mechanically polished show a faster PL decay

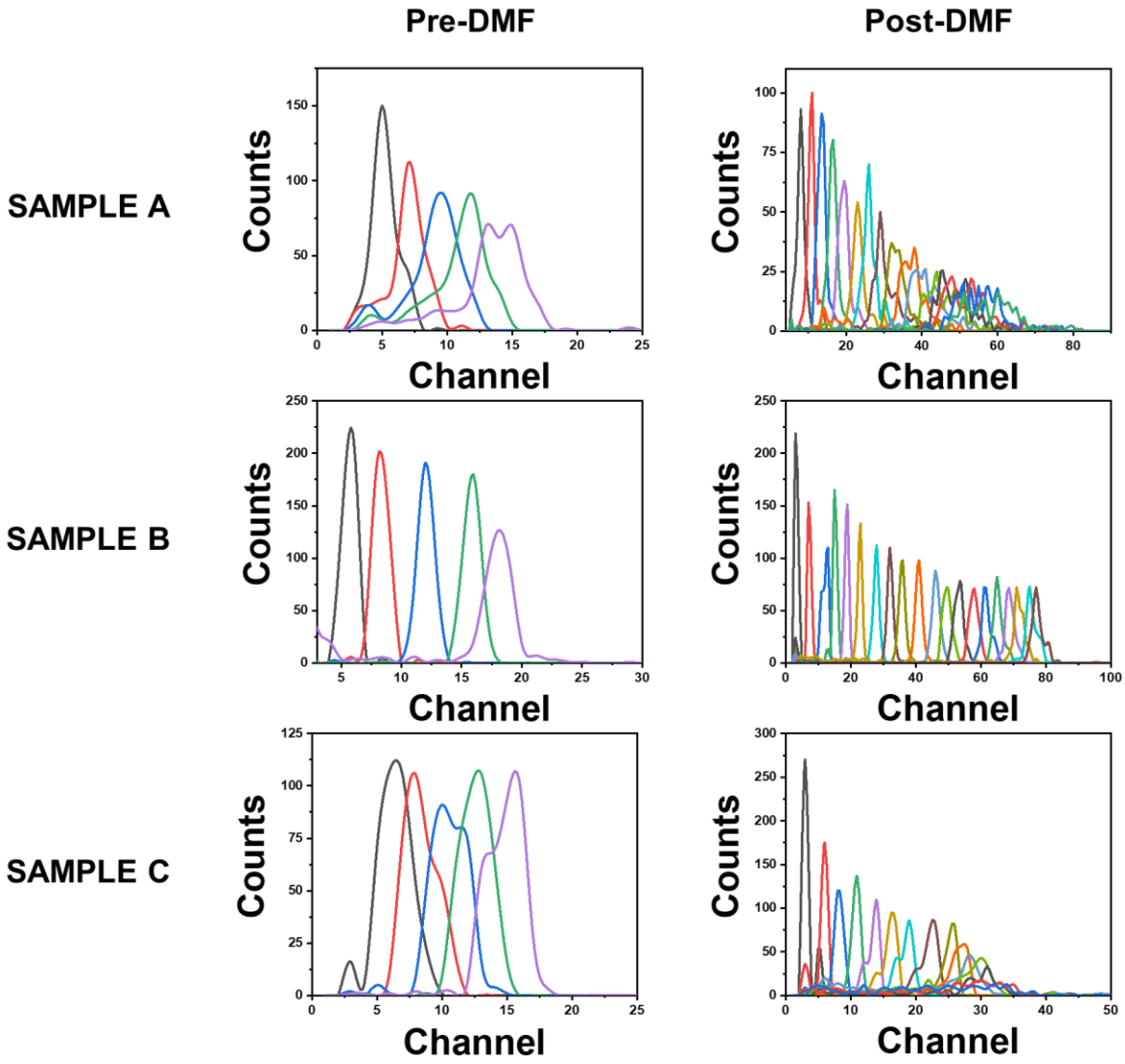

Figure 3.2.5. Spectral comparison between three $MAPbBr_{2.85}Cl_{0.15}$ samples exposed to a ^{210}Po radiation source before and after DMF Polishing. The bias range used for each plot are provided in Table 3.2.1

Table 3.2.1. Bulk resistivity and bias voltage range comparison before and after chemomechanical polishing of three $MAPbBr_{2.85}Cl_{0.15}$ SCs. No DMF/DMF refers to whether the sample had been chemomechanically polished with DMF [58].

Sample ID	**Size (mm^3)**	**Bulk Resistivity (Ω-cm)**	**Bias Voltage Range ($\|V\|$)**
A-No DMF	5.97 × 5.88 × 3.11	2.41×10^8	40-80
A-DMF	5.97 × 5.88 × 3.09	2.60×10^8	30-180
B-No DMF	7.61 × 6.27 × 3.20	3.43×10^8	40-80
B-DMF	7.61 × 6.27 × 2.28	3.52×10^8	20-210
C-No DMF	5.23 × 5.71 × 2.30	2.83×10^8	50-90
C-DMF	5.23 × 5.71 × 2.02	3.20×10^8	30-170

which is shown in the spectra taken post-DMF polishing. Here, apparent refers to signal passed through the pulse processing chain, which does not take into account ballistic deficit [45]. This is evident in that the alpha peaks in the spectra did not shift as predicted the Hecht equation, which was discussed in previous sections. However, assuming that the bulk mobility did not change due to chemomechanical polishing, this direct comparison provided quantitative evidence of improved surface quality and stability under bias. Additionally, a slight increase in the apparent bulk resistivity was observed after chemomechanical polishing, as shown in Table 3.2.1. The origin of the increased apparent bulk resistivity could be attributed to a reduction of surface leakage current or current injection through surface defect states due to a more uniform contact deposition.

Additionally, if a higher quality surface limits the surface recombination velocity, this should result in a closer agreement between the $\mu\tau$ values obtained via the Hecht and Many equations, since the additional term in the Many equation would converge to 1 as S/μ approached 0. As previously shown with the polycrystalline MAPB samples, a high surface recombination velocity from a very low-quality surface resulted in a difference in hole $\mu\tau$ by two orders of magnitude. For the recrystallized $MAPbBr_{2.85}Cl_{0.15}$ detector from Figure 3.1.4A and B which had been DMF polished, there was a minimal increase of $\mu_h\tau_h$ from 1.31×10^{-4} cm^2 V^{-1} using the Many equation to 1.82×10^{-4} cm^2 V^{-1} with the Many equation along with an S/μ_h value of 71.08 V cm^{-1} [58]. These results collectively demonstrate that implementing the DMF polishing step to improve surface quality and limit the surface recombination velocity yields improvements to charge collection efficiency, carrier lifetime, stability under bias, and observed bulk resistivity, which led to this method being an integral part of the detector fabrication process.

Finally, although the benefits of DMF polishing have been clearly demonstrated, the process itself could lead to physical deteriorations if not carefully controlled. Since DMF is the same solvent used for MAPB SC growth, excessive use of DMF could lead to the undesired degradation of the surface. It was also observed that DMF would preferentially etch at any defect sites, indicating that this process could only be used as a finishing step after the vast majority of surface defects had been mitigated through mechanical polishing. Collectively, these phenomena serve as the motivation for the chemomechanical polishing methods described in Chapter 2 that

occur after the completion of mechanical polishing and only involve brief periods of crystal contact with the DMF saturated polishing paper.

Argon Plasma Cleaning

In addition to the surface passivation techniques described in Chapter 1.4, removal of organic contaminants using Ar/O_2 plasma is a well-documented technique for passivating the surface of a detector [148-150]. However, several minutes of plasma cleaning resulted in significant surface damage to a pure MAPB crystal chemomechanically polished with DMF as shown in Figure 3.2.6A. X-ray Photoelectron Spectroscopy (XPS) analysis was carried out on the MAPB sample before and after plasma cleaning with 95% Ar/5% O_2 to determine the nature of the plasma induced damage. Figures 3.2.6B and 3.2.6C show the XPS spectra with and without plasma treatment for the Pb 4f emission region and the survey scan respectively. These spectra show a much higher concentration lead following plasma cleaning compared to before when the sample had only been treated with DMF. Since the plasma cleaning is designed to remove organic contaminants, it was hypothesized that significant amounts of the organic components of the MAPB sample itself (such as methylammonium) were also inadvertently removed during the process, which supports the findings from Xiao *et al* that plasma treatments generate lead-rich surfaces on hybrid perovskite materials [148]. There was also a clear broadening of the Pb peaks and centroid shifts in Figure 3.2.6B as shown in Table 3.2.2, which indicated the presence of an increased number of lead species within MAPB following plasma cleaning and was potentially brought about by the strong presence of oxygen in the plasma environment. Moreover, the small peaks that appeared around 138 eV and 143 eV following plasma cleaning indicated the presence of metallic Pb^0 defects that acted as nonradiative recombination centers, which have a negative effect on charge carrier transport [151]. These results build on the previously reported success with plasma cleaning on perovskite surfaces by demonstrating that plasma cleaning to remove organic contaminants can result in degradations rather than enhancements if the treatment time is not carefully controlled.

This section evaluated DMF polishing and plasma cleaning to meet the need for proper preparation of crystal surfaces. The results demonstrated that both processes must be well

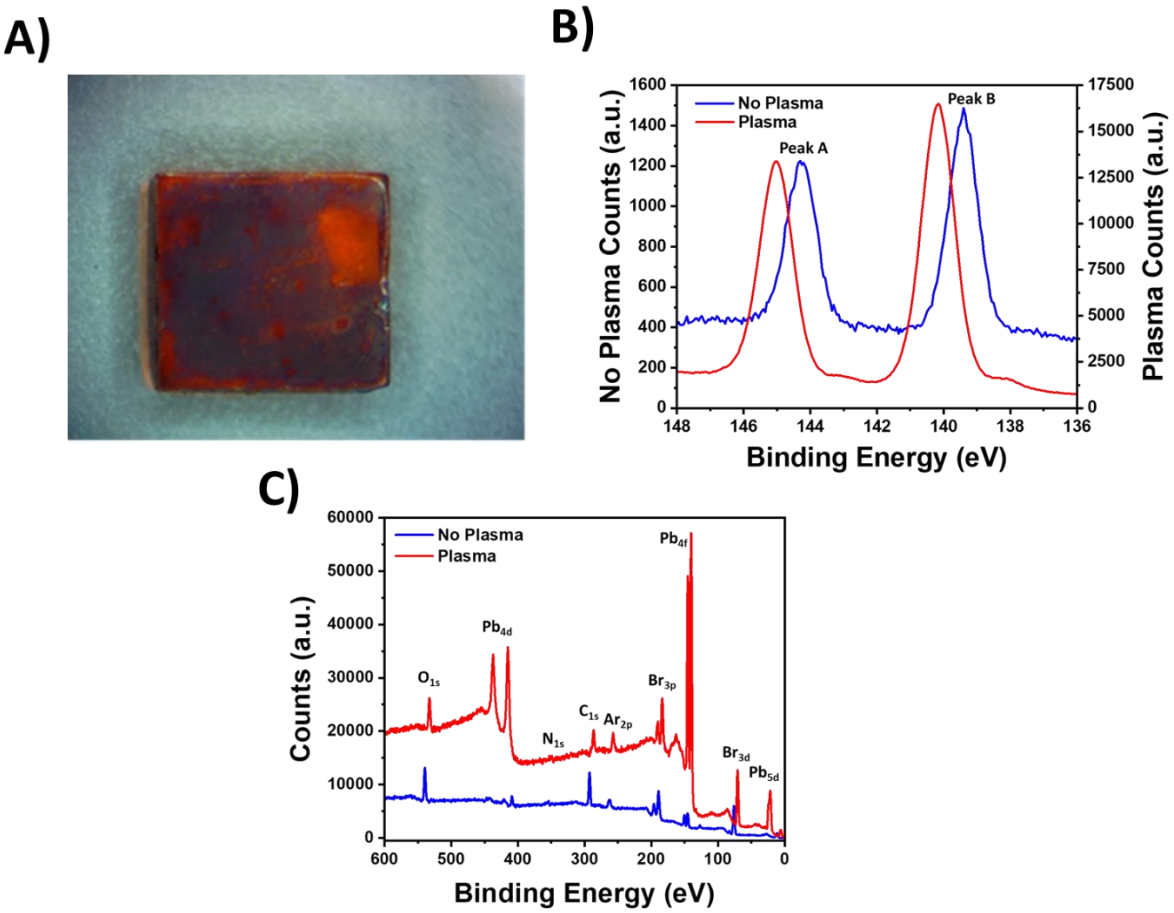

Figure 3.2.6. A) Image of a MAPB sample after 95% Ar/5% O_2 plasma cleaning in a Harrick Plasma Cleaner for several minutes, B) High resolution XPS scan of the Pb 4f region for MAPB with and without plasma cleaning, C) XPS survey scan of MAPB with and without plasma cleaning

Table 3.2.2. Parameters for the two peaks within the Pb 4f XPS high resolution scan in MAPB before and after plasma treatment

Peak ID	FWHM (eV)		Centroid (eV)	
	No Plasma	***Plasma***	***No Plasma***	***Plasma***
Peak A	1.025	1.15	144.3	145.05
Peak B	0.975	1.125	139.4	140.15

controlled in order to decrease the risk of crystal degradations. However, these methods were also shown to lead to significant improvements to surface quality and radiation detection performance when properly implemented. As previously stated, the mitigation of defect states at the surface also helps to improve the quality of the electrode interface with the crystal. The following section will elaborate further on the MAPB radiation detector fabrication process by describing the electrode designs implemented.

3.3. Tin Oxide Interface

As stated in Chapter 1.4, ionic conductivity within MHP detectors under bias has been previously observed and reported to have a negative effect device performance [45, 46, 152-155]. Specifically, the migration of bromine ions has been shown to form metal-bromine complexes at the anode interface in the absence of interfacial layers to mitigate the effect, which causes distortions to the electric field [110]. As described in Chapter 2, previous electrode designs utilized within the research group had a Cr/MAPB/C_{60}/BCP/Cr contact scheme, with the organic electron extraction layers at the anode consisting of 20 nm of C_{60} and 8 nm of bathocuproine (BCP), and capped with 60 nm of chromium on each side. This design is shown in Figure 3.3.1B and will be referred henceforth as E1. While there have been reports of success using the E1 contact scheme with MAPB [45, 50, 53], it was observed that detectors fabricated with this method failed to consistently produce radiation induced signals in many samples, which could be attributed to the lack of any interfacial layers to mitigate the effect of bromine migration induced electrochemical reactions at the interface. As a result, a new electrode scheme utilizing a tin oxide (SnO_2) layer was developed and evaluated. While several metal oxide options were available, SnO_2 was ultimately selected due to the corrosion resistance of tin. The new contact scheme, which is shown in Figure 3.3.1C and will be referred to as E2, was fabricated through RF sputtering with 4 nm of SnO_2 on one face and capped on both ends with 60 nm of Cr. All tests were designed with the face containing SnO_2 as the anode and electron extraction layer.

Switching to the E2 contact scheme led to a significant increase in device responsivity to alpha particles. This was evident through a series of MAPB alpha radiation tests that responded with the E2 contact scheme while the same detector substrates did not respond with the E1 contact

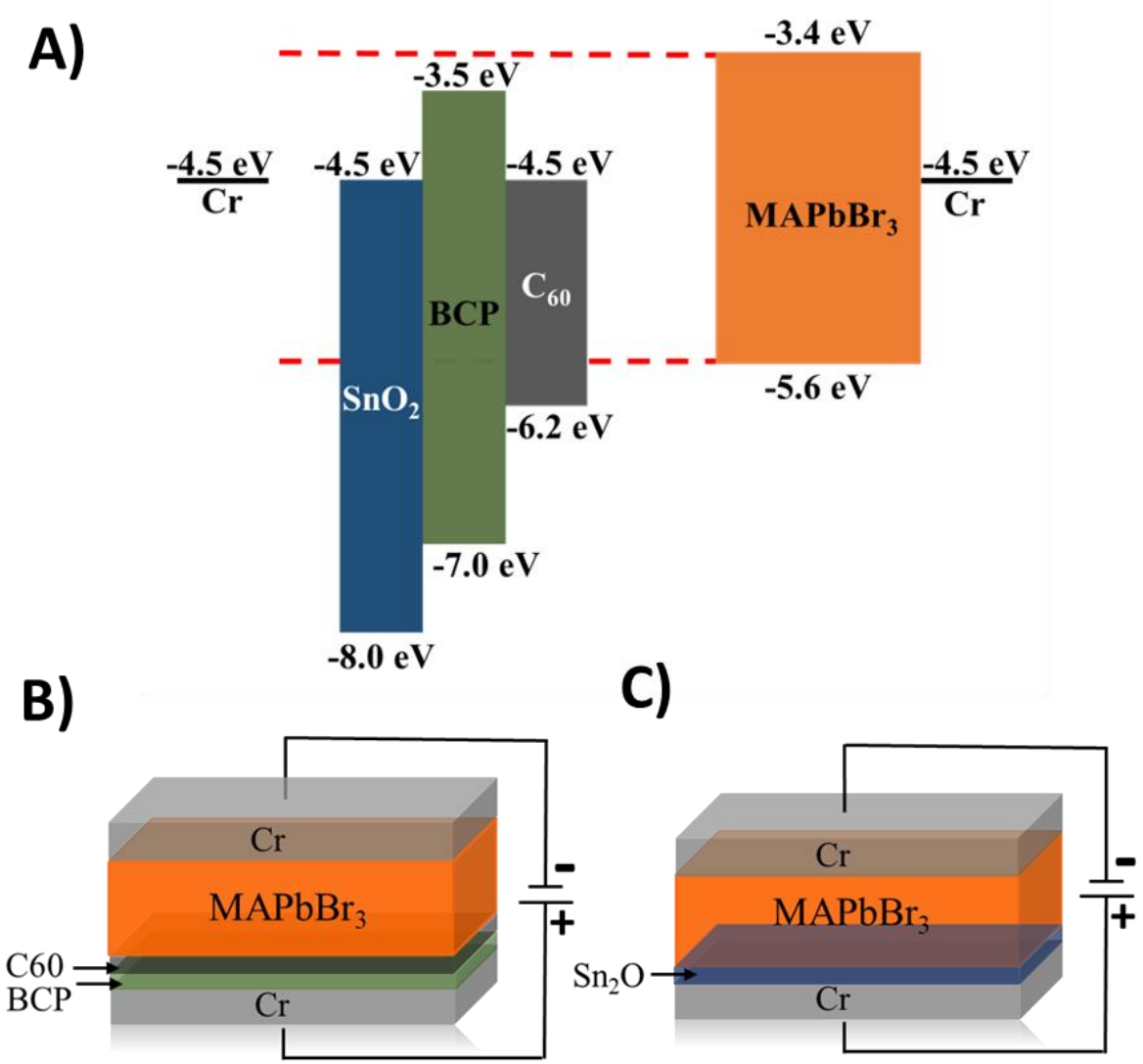

Figure 3.3.1. A) Band structure comparison between MAPB and several interfacial materials. Pictorial representation of the contact scheme B) E1 and C) E2

scheme, which are presented in Table 3.3.1. While no pattern of bulk resistivity was observed following the change of electrode material, it was nonetheless successful in extracting alpha particle-induced signals [58].

As previously mentioned, electrons are known to have relatively poor charge transport properties compared to holes in MAPB, which results in very few reports of using alpha particle induced signals to characterize $\mu_e\tau_e$. However, after switching to the E2 contact scheme with the SnO_2 electron extraction layer, the "MAPB 1" detector from Table 3.3.1 demonstrated electron response to alpha particles, which is shown in Figure 3.3.2. Although this particular device did not exhibit extraordinary response from hole collection, its electron collection is notable. Using the Hecht equation, the $\mu_e\tau_e$ was estimated to be 2.79×10^{-4} cm^2 V^{-1}. By taking into account the effect of surface recombination via the Many equation, $\mu_e\tau_e$ was then estimated to be 4.59×10^{-4} cm^2 V^{-1}, with an S/μ_e value of 57.82 V cm^{-1}. The single trace analysis shown in Figure 3.2.2C at a bias of +100 V showed a 5%-95% rise time of 6.9 μs, which could be interpreted as the electron drift time through the crystal bulk. Solving for mobility via the standard drift velocity equation (Equation 3.1.2), the electron mobility was determined to be 14.51 cm^2 V^{-1} s^{-1}. Using this electron mobility, the measured lifetimes using the Hecht and Many equations were calculated to be 19.23 μs and 31.63 μs, respectively, which were in agreement with electron lifetimes measured through ToF experiments [156]. Finally, using the apparent electron mobility to solve for the surface recombination velocity, S was determined to be 8.39×10^2 cm s^{-1}, which is still significantly higher than those reported in Table 1.4.1 and is likely a result of polishing by hand out of necessity due to the brittle nature of the crystals [58]. The electron response along with improvements in device fabrication success rate and stability collectively demonstrate the benefit of implementing the SnO_2 electron extraction layer. Due to the observed success, this contact scheme was incorporated into all detectors presented in this work except for the polycrystalline MAPB wafers.

3.4. Low Energy Gamma Ray and X-ray Sensing

The high photon stopping power due to a high effective atomic number along with the possibilities for low-cost, large-volume growths give MAPB significant potential for X-ray radiation detection, and this section will describe work the notable results this work has achieved

Table 3.3.1. Comparison of bulk resistivity using the previous electrode configuration at the anode E1 (Cr/MAPB/C_{60}/BCP/Cr) and new electrode configuration E2 (Cr/MAPB/SnO_2/Cr) [58].

Sample Type	Surface Dimensions (mm^2)	E1 Resistivity (Ω-cm)	E1 Detector Thickness (mm)	E2 Resistivity (Ω-cm)	E2 Detector Thickness (mm)
$MAPbBr_{2.85}Cl_{0.15}$ Recrystallized	5.66 × 5.88	4.18×10^8	1.66	3.33×10^8	1.47
MAPB 1	4.16 × 5.53	3.52×10^8	1.82	9.87×10^8	1.00
MAPB 2	6.70 × 5.41	8.23×10^8	2.14	7.18×10^8	1.57

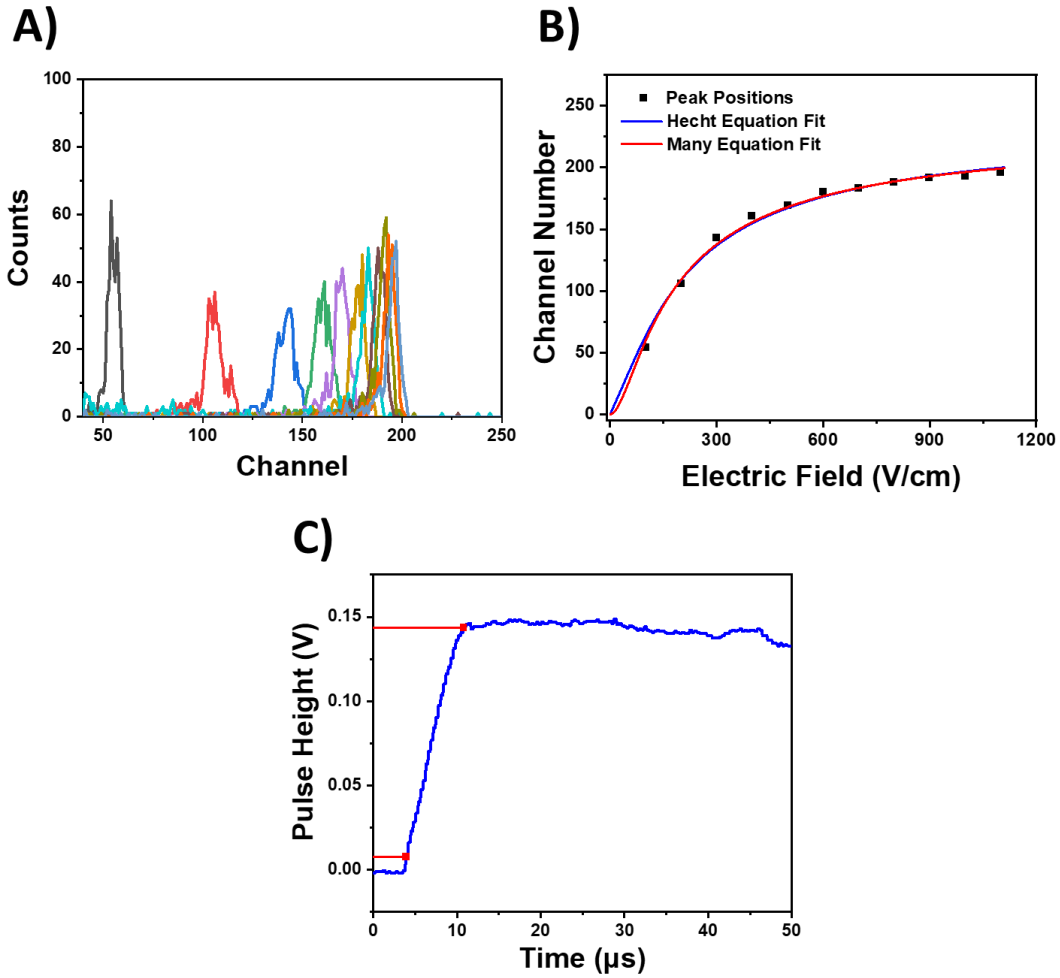

Figure 3.3.2. Electron collection from pure $MAPbBr_3$ with SnO_2 layer. A) Alpha spectrum and B) peak positions as a function of electric field for Hecht and Many fits with bias increasing from +40 V to +110 V in +10 V increments (Gain: 25, Shaping Time: 10 µs, Count Time: 60 s), C) Single trace analysis of radiation induced signal at +100V for calculation of MAPB electron mobility

in demonstrating the low energy X-ray and gamma ray sensing capabilities of MAPB.

Due to the imbalanced charge carrier properties in MAPB described in Chapter 1.2, the spectroscopic capability is severely hindered by highly penetrating radiation such as gamma rays and neutrons that deposit their energy stochastically throughout the detector and generate depth-dependent charge. As demonstrated in Chapter 3.1 however, depth dependence is minimal when sensing alpha particles, whose range is much smaller than the detector and yields a very narrow range of near surface signals (without variable ballistic deficit) that still allows for peaks to be resolved in the spectrum. While this is not the case for high energy gamma rays, it is possible for low energy X-rays and gamma rays to have a short enough penetration depth to where the effects of depth dependent charge generation and variable ballistic deficit can be reduced. The spectrum from a non-spectroscopic ^{241}Am smoke detector source is shown in Figures 3.4.1A and B, which show the LiMAPB response to the 5.48 MeV alpha particle and the 59.5 keV gamma ray. The resolution of 82% at 59.5 keV was poor in this particular LiMAPB sample, which could be attributed to the poor carrier properties described in previous sections. However, Figures 3.4.1C and D show the response of a 5% Cl doped ITC grown MAPB SC detector, where the gamma ray photopeak had a resolution of 15% at 59.5 keV. This value is comparable to the resolution achieved by He *et al*., who achieved a resolution of 12% at 59.5 keV in MAPI, which is the best resolution achieved with MHPs at this energy [56]. These results demonstrate the potential of MAPB for high resolution spectroscopic low-energy X-ray and gamma ray sensing without any correction techniques.

MAPB has also demonstrated potential to be used as an X-ray imaging detector. The polycrystalline MAPB from Chapter 3.1 was able to resolve a radiograph of a brass key using soft X-rays from a tungsten anode X-ray tube at a 40 kV potential. The radiograph of the brass key in Figure 3.4.2B was produced using electron collection for MAPB A, which was 3-4 times thicker than any reported polycrystalline perovskite X-ray detectors, and the response proved to be sufficient for resolving the general features of the key. Previously published literature has already demonstrated that electron transport in MAPB is significantly poorer than holes and as a result, this image potentially represents baseline capabilities of the MAPB material for X-ray imaging applications. To determine how sensitivity changed under different applied biases as well as

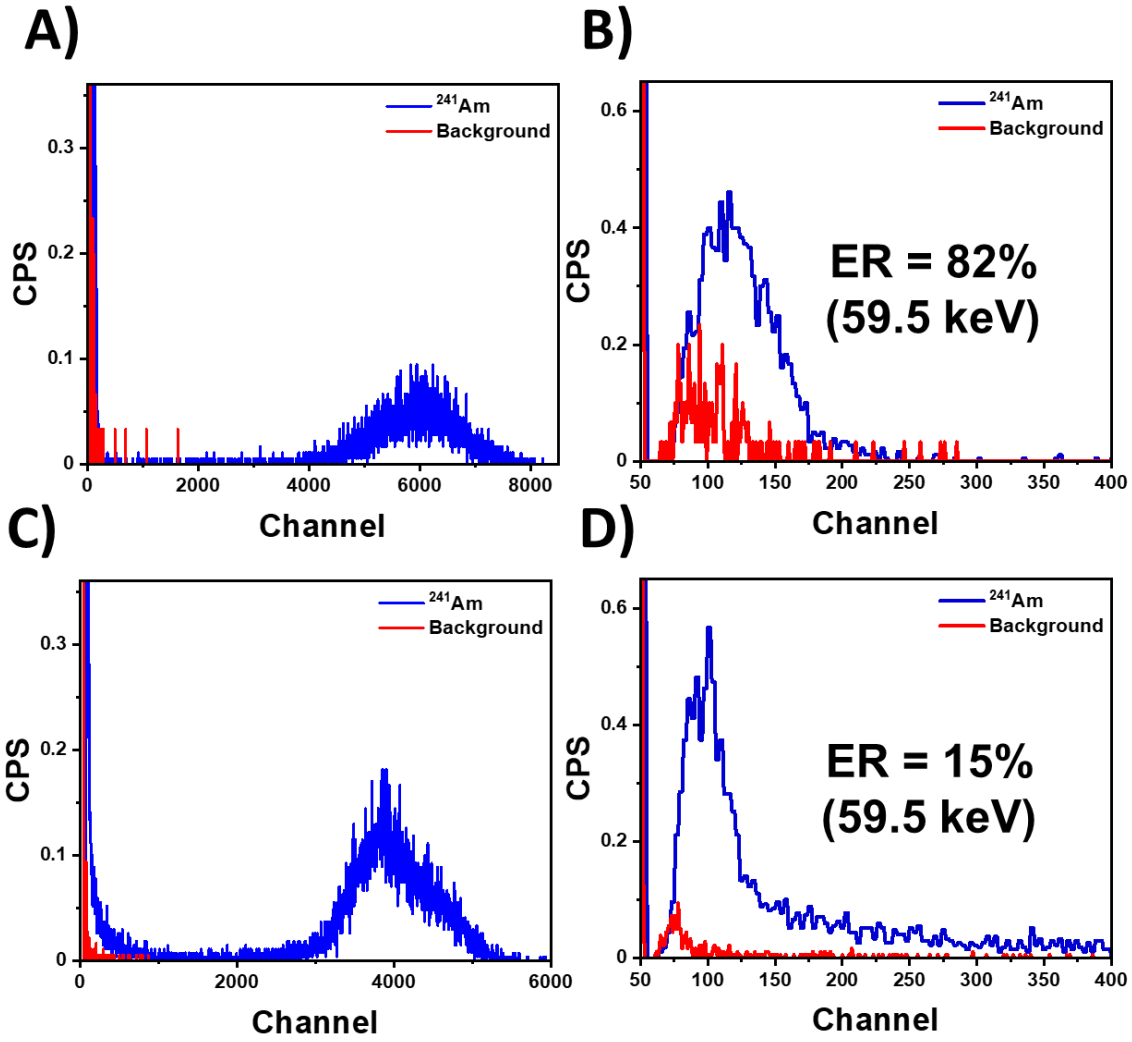

Figure 3.4.1. Alpha peak and 59.5 keV gamma ray photopeak respectively from a non-spectroscopic ^{241}Am smoke detector source in A-B) LiMAPB (Gain: 50, Shaping Time: 10 µs, Bias: -150 V) and C-D) $MAPbBr_{2.85}Cl_{0.15}$ (Gain: 50, Shaping Time: 10 µs, Bias: -200 V). Due to LiMAPB being the thinner of the two detectors, different biases were utilized to maintain similar electric fields strengths

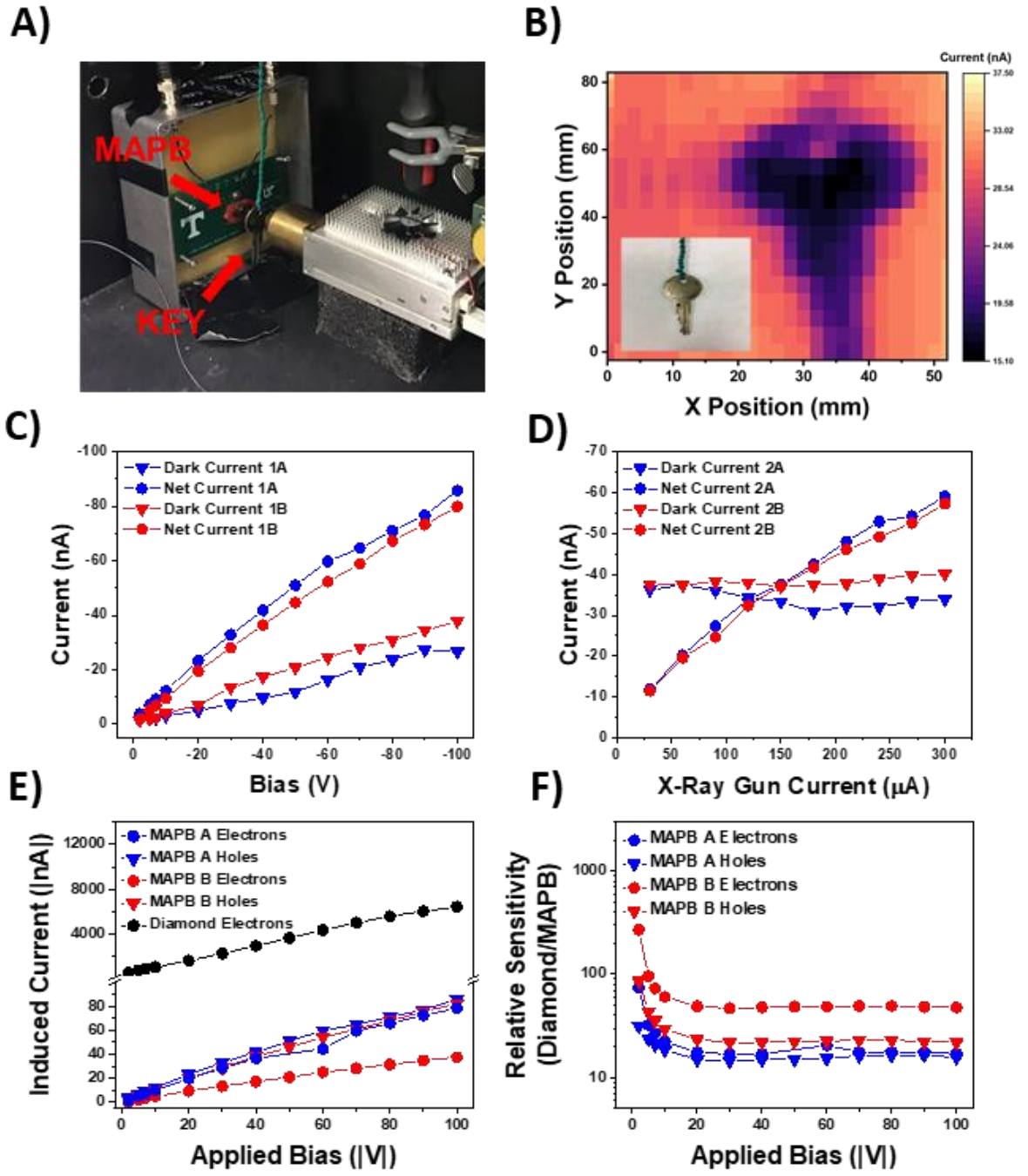

Figure 3.4.2. A) X-ray imaging of a brass key moved by a stepper motor, B) Radiograph of a brass key (insert) captured by collecting electrons from MAPB A, C) Repeated current vs. bias experiments (Tube settings: 40 kV and 300 μA) showing hysteresis and a decrease in sensitivity, D) Repeated current vs. X-ray flux experiments showing relatively stable sensitivity at -50 V bias, E) Net induced current vs. X-ray flux while collecting diamond electrons and MAPB holes and electrons (Tube settings: 40 kV and 300 μA). Current and bias is listed as absolute value, F) MAPB sensitivity relative to diamond for each carrier (Tube settings: 40 kV and 300 μA). Bias is listed as absolute value

evaluate MAPB stability during irradiation, two sets of experiments were performed on MAPB A, which each set consisting of a pair of repeated experiments. Sensitivity is defined by Equation 3.4.1, where S is the sensitivity, I_0 is the total induced current, I_d is the dark current, and A is the active area defined by either area of the radiation fluence or the area of the detector if it is small relative to the fluence. The position of the readout pin to the picoAmmeter on the detector was not changed between the two sets of experiments, which were conducted one week apart. The results of the first experimental set (referred to as experiments 1A and 1B) in Figure 3.4.2C showed the dark current and net induced current with the X-ray tube set at maximum power (40 kW, 300 μA) while the applied bias was gradually increased from -2 V to -100 V. Here, an increase in dark current was clearly observed along with a decrease in net current across all biases following experiment 1A, which lasted 25 minutes. Given that the dose rate and detector area remained constant across both experiments, the decrease in net current is synonymous with a decrease in sensitivity. Particularly toward the higher biases, the dark current increased by between 5-10 nA on average in experiment 1B, which resulted in sensitivity reductions by 1-2 nC Gy^{-1} cm^{-2} at each bias.

$$S = \frac{(I_0 - I_d)}{D \times A} \tag{3.4.1}$$

Figure 3.4.2D shows the dark current and net currents induced on MAPB A between the two experiments in the second experimental set (referred to as experiments 2A and 2B) with the bias set to -50 V throughout and the current to the X-ray tube decreased in 30 μA increments from the maximum current. The sensitivities were calculated by performing linear fits to the net induced current density across the entirety of each experiment as a function of dose rate, which is correlated with the current applied to the X-ray tube as previously shown in Table 2.1. Following experiment 2A, which lasted approximately 11 minutes, a higher dark current was observed during experiment 2B, which lasted 6 minutes. Although this increase in dark current may have been evidence of hysteresis, the net current remained very similar, resulting in a minimal decrease in sensitivity from 13.42 to 13.00 nC Gy^{-1} cm^{-2} in experiments 2A and 2B respectively.

There were several notable features in these results. First, experiments 2A and 2B demonstrated that sensitivity levels could be maintained under constant bias for significant

irradiation times, which is critical to ensuring stable radiographs over the course of an imaging procedure. Additionally, as previously stated, experiment sets 1 and 2 were conducted one week apart, with the detectors stored in a dark and dry environment under vacuum. Based on the experiment 1B net current at -50 V, the sensitivity at that point was calculated to be 11.83 nC Gy^{-1} cm^{-2}. Following one week of storage, the sensitivity from experiment 2A had nearly returned to the original value calculated for experiment 1A at -50 V (13.49 nC Gy^{-1} cm^{-2}). This observed self-healing supported the phenomenon reported by Gao *et al* [131] and indicated that some of the detrimental phenomena that hindered the radiation response of MAPB appeared to be passively reversible. It is possible that long-term storage in a dark, dry, and vacuum environment resulted in redistribution of mobile ions to remove the spatially dependent charge distribution that caused polarization, thermal excitation of trapped charges, and/or lattice expansion that stabilized the perovskite [120, 155, 157, 158]. At the same time, while the sensitivity was improved after a period of non-operation, the dark current in experiments 2A and 2B are higher than experiment 1B, which could be indicative of some passively irreversible mechanisms that, while observable, did not significantly degrade MAPB's radiation sensing capabilities.

While the results in Figures 3.4.2B-D collectively demonstrated that MAPB is capable of quasi-stable X-ray sensitivity, the dose rate utilized for the imaging was 0.368 Gy s^{-1}, which was relatively high compared to medical or security applications as described in Chapter 1.1. The high dose rate used in this study enabled the observation of the sensitivity of MAPB mosaic wafers A and B, where we found that the electron/hole sensitivities were 9.59/13.42 and 3.32/11.01 nC Gy^{-1} cm^{-2} for MAPB A and B respectively at ±50 V, which are much lower than other reported MAPB sensitivity values as listed in Table 1.3.1 [42, 49-52]. For additional comparison, an experiment using a diamond sensor was conducted and compared to MAPB A and B to determine how the sensitivities of MAPB compare to a well-established radiation sensing material [159, 160]. As shown in Figures 3.4.2E and F, the responses of MAPB A and B for both holes and electrons were orders of magnitude lower than that of diamond across all experiments. Noting that the diamond detector was thinner and has a Z_{eff} of 6, it is clear that the fabricated MAPB mosaic wafer detectors in this report possessed very low sensitivities. For comparison, CsI:Tl scintillators formed on

amorphous silicon photodetector arrays and amorphous selenium possess sensitivities of 0.3 and 0.44 μC Gy^{-1} cm^{-2} respectively [13].

As discussed in Chapter 1.4, much effort within the perovskite development community has been devoted toward identifying and characterizing inherent or induced mechanisms that limit degrade MHP device performance. This work has already presented surface quality and ionic conductivity as hindering mechanisms, and Chapter 3.7 will also present the effects of radiation damage as another potential explanation for the extremely low X-ray sensitivity values observed in the MAPB mosaic wafers.

3.5. Computational Methods of Improving Gamma Ray Sensing

As previously stated in Chapters 1.2 and 2, the consequence of semiconductor detectors with charge carrier properties that are both imbalanced and low is twofold. Since the $\mu\tau$ and drift length of electrons in MAPB are significantly lower than holes, little spectroscopic information can be obtained from highly penetrating radiation such as gamma rays and neutrons due to the depth dependence of the interaction region. Variable ballistic deficit also plays a significant role in hindering spectroscopic performance when the mobility of the dominant carrier is also low [45, 58]. The manifestation of these effects can be seen in Figure 3.5.1A, where the same LiMAPB sample from Chapters 3.1 and 3.4 was exposed to gamma rays from ^{57}Co, ^{133}Ba, and ^{137}Cs. As expected, none of the characteristic peaks from these sources could be resolved due to the depth dependent interactions coupled with poor charge transport properties. The upper bounds of the spectra still increased in a manner corresponding to the maximum energy of the source used (122 keV, 300-400 keV, and 662 keV respectively), but this limited degree of spectroscopic information was the extent of what could be obtained without correction techniques.

Several electrode patterns or fabrication techniques such as Frisch grids, hemispherical, pixel, and coplanar geometries discussed in Chapter 1.2 utilize the near field effect to discard the contributions of the slower carrier and manipulate the weighting field so that no charge is induced on the electrodes until the dominant carrier is close to the collecting electrode, greatly reducing the positional dependence of the signal amplitude [23-31]. Other methods, such as rise time discrimination or bi-parametric techniques apply corrections during post-processing to mitigate

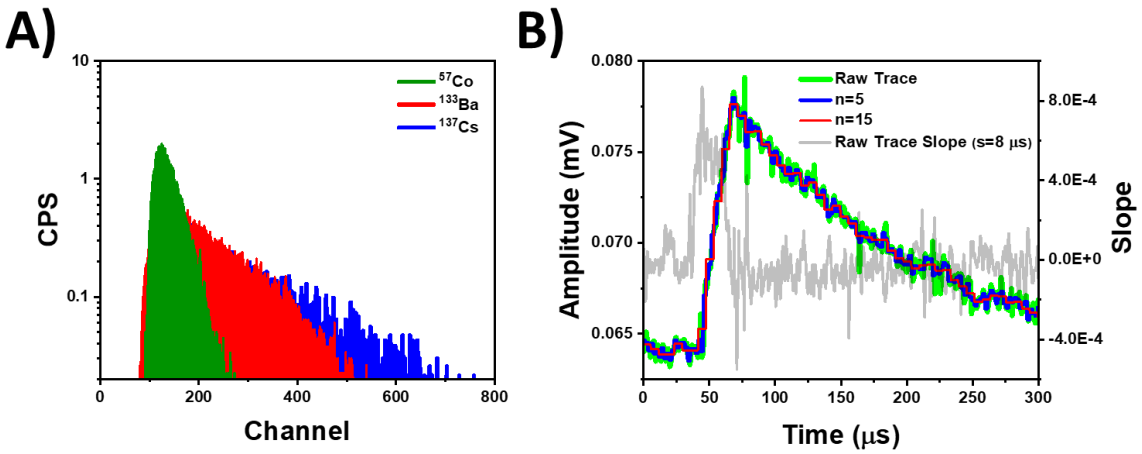

Figure 3.5.1. A) Background subtracted spectra from various gamma ray sources with a 5.1 × 4.7 × 1.2 mm LiMAPB detector biased at -120 V (Gain: 50, Shaping Time: 10 μs), B) The effect of smoothing on a raw radiation induced trace, with the slope between two points on the signal spaced 8 μs shown in gray, which was used to set the threshold for determining the start of the rise

the negative effects from the slower carrier [32-35]. The remainder of this section will describe a program that was developed in Python that corrected for charge losses due to imbalanced and low charge carrier properties. A Bridgman grown $CsPbBr_3$ detector with a thickness of 3.1 mm, a surface area of 85.4 mm^2, a $\mu_h\tau_h$ of 5.5×10^{-4} cm^2 V^{-1}, and a S/μ_h value of 20 was used to evaluate the program through exposure to a ^{137}Cs source at a bias of -120 V and a distance of 6 mm over a 52-minute period. The program consisted of three main components: preparation of the set of traces for processing and analysis, correction for charge losses during hole drift, and mitigating charge losses due to depth dependent gamma ray interactions.

Preparing Traces for Analysis

The presence of significant noise fluctuations within the trace complicates any analytical techniques, making the removal of these fluctuations an important component of the analysis process. The use of Fast Fourier Transform filters (FFT) for this purpose will be discussed in Chapter 3.8, while this section discusses a simpler method of removing noise fluctuations and smoothing traces through the use of a moving average. The moving average calculates the mean value of a subset of data points, which is then assigned to all data points within the subset before repeating the process on subsequent subsets. This is shown in Equation 3.5.1, where *n* is the spacing between each subset to be smoothed and *k'* represents the new subset of *n+1* data points all having the same value from the mean of data points *k* from the original subset. As shown in Figure 3.5.1B, although a greater value of *n* would remove more of the noise fluctuations, it also results in the loss of trace information, making it desirable to minimize the value of *n* where possible.

$$[k_i' k_{i+1}', \ldots k_{i+n}'] = \frac{k_i + k_{i+1} + \ldots k_{i+n}}{n+1} \tag{3.5.1}$$

The second portion of trace preparation involves determining when the rise of the signal begins, which is critical for determining the signal rise time and amplitude. This is often achieved visually with a small number of traces, as has been shown in Chapter 3.1 to determine the carrier mobility through single trace analysis. With a large dataset, computationally finding the start of the signal rise was achieved by determining whether the slope between two points exceeded a

threshold slope value that could only be representative of a signal rise. The first parameter to be optimized for this component of the program was the distance between the two points. A smaller spacing could be more sensitive to noise fluctuations that return an incorrect identification for the start of the rise, while too great of a spacing between points could miss the rise entirely. The second parameter to be optimized was the threshold slope value itself. Figure 3.5.1B also shows the slope between two points on the trace 8 μs apart, with the abscissa representing the timestamp of the initial point. Even in the presence of significant noise fluctuations, the slope between two points is largely dependent on whether both points are before the rise, one point is on the rise and one is far from the rise start, or one point is on the rise and one is close to the rise start or on the rise as well. The slope can also vary based on the rise time of the signal as well as the amplitude, however those variations are less significant than the positioning of the two points. As a result, the general range for the slope threshold was on the order of the slope for the rise itself, which meant that the threshold could only be reached if the first point was very close to the start of the rise. As seen in Figure 3.5.1B, the slope does not sharply increase until the rise begins, which allows for identification of the start of the rise when the threshold slope criterion was met. Following determination of the start of the rise, all voltage values prior to the rise start were set equal to the rise start voltage to establish a clear baseline. The entire trace was then shifted so that the baseline was set at zero.

Trace Filter

At this stage, it was necessary to apply a filter that could reject any traces of insufficient quality for processing and analysis. Ideally, the true radiation induced traces would have a fast initial rise followed by an exponential decay. However, the trace collection can still be triggered by phenomena such as electronic noise or pulse pileup as shown in Figure 3.5.2B, resulting in imperfect traces being included in the dataset. To identify traces containing these artifacts, an artificial trace was simulated by fitting the piecewise function from Equation 3.5.2 to each real trace and optimizing the fit, where t is the timestamp, m is the slope of the rise, and τ is the fall time of the preamplifier. The coefficient of determination (commonly referred to as R^2 in statistics)

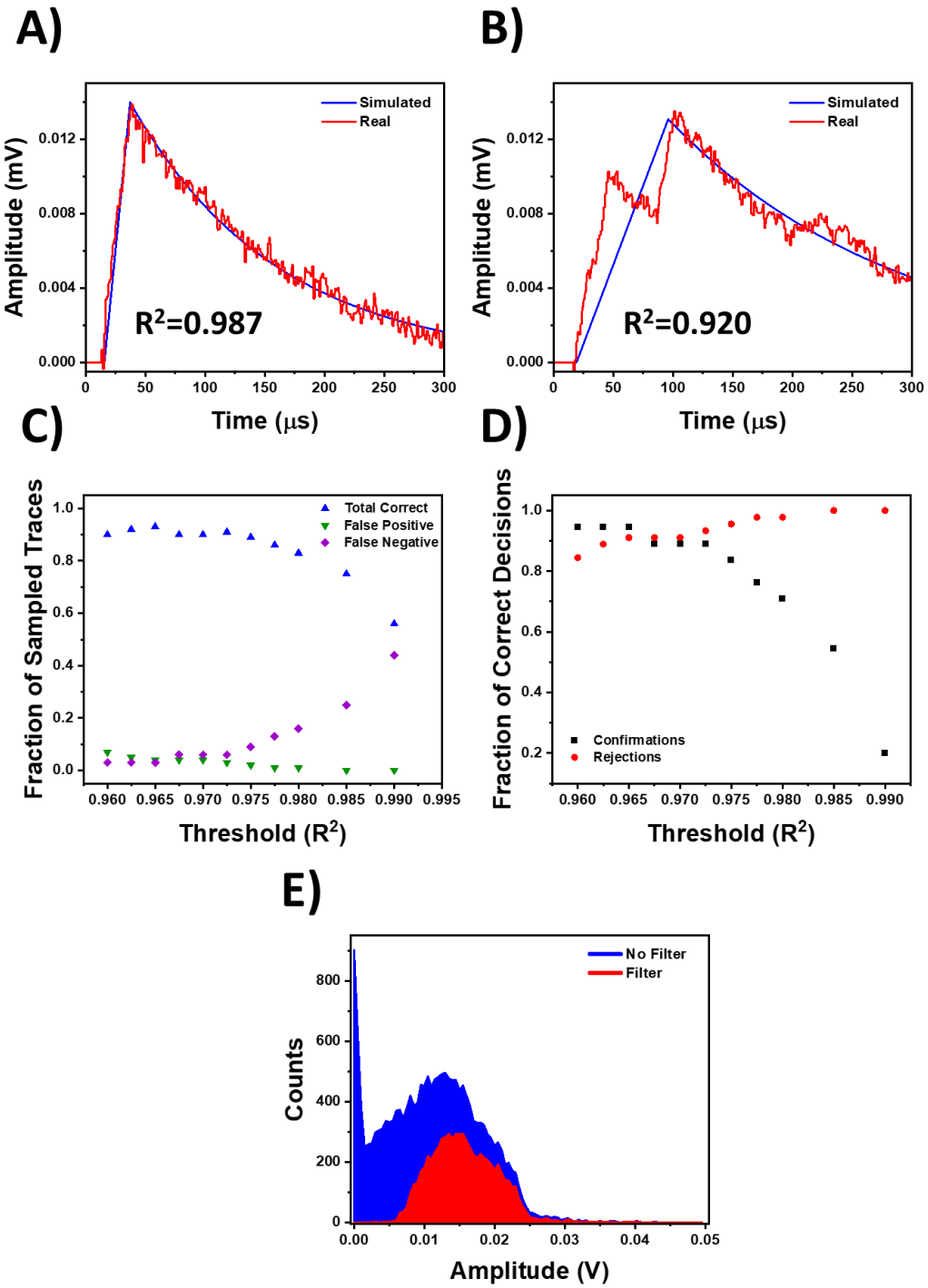

Figure 3.5.2. Simulated traces (blue) optimized to the raw trace from ^{137}Cs (red) with corresponding coefficient of determination for A) suitable trace for processing and B) unsuitable trace for processing due to pileup, Results of various R^2 thresholds from 100 spot checks C) Accuracy of trace filter, and D) Breakdown of correct confirmations and rejections. The threshold was ultimately set at 0.965 to maximize the accuracy of decisions, E) Spectral differences before and after applying the trace filter

between each artificial and real trace was then calculated, resulting in a metric that measured how well the real trace matched the ideal simulated trace shape.

$$f(t) = \begin{cases} 0 & t \leq Rise\ Start \\ mt & Rise\ Start < t \leq Rise\ End \\ f(Rise\ End) \times e^{-\frac{t}{\tau}}, & t > Rise\ End \end{cases} \quad (3.5.2)$$

As shown in Figure 3.5.2A, a coefficient close to 1 is indicative of a trace that is suitable for processing, while a lower value is likely to be nonideal. Setting an appropriate threshold below which the traces are rejected was achieved by visually confirming or rejecting traces through random spot checks and comparing against the filter's acceptance or rejection verdict. Figures 3.5.2C and D show that after 100 spot checks, the threshold to maximize accuracy and reduce the false negative and false positive rates was set to 0.965 for this particular dataset taken from a Bridgman grown $CsPbBr_3$ crystal exposed to ^{137}Cs gamma rays. Following the implementation of the trace filter, the total number of traces used to build the spectrum was reduced from 18,097 to 6,941. Figure 3.5.2E shows the original unfiltered spectrum along with the filtered spectrum, which show that the filter was effective in removing much of the noise that saturated the lower energy bins. However, doing so discarded over 60% of the acquired data, indicating that the efficiency of data collection was severely hindered by electronic noise and pulse pileup, which were not properly mitigated by the data collection settings.

Corrections for Charge Losses During Transport

After the traces had been processed and filtered for analysis, the rise times and amplitudes were calculated using the same methods described in Chapter 3.1, and deconvolution using Equation 3.1.1 was subsequently applied to the traces as well to remove ballistic deficit from the preamplifier output. The spectral differences with and without the deconvolution can be seen in Figure 3.5.3A, and show a shift to higher channel numbers that further demonstrates how this technique can mitigate charge losses from slow signal rise times relative to the fall time of the preamplifier. After deconvolution, the second correction implemented in the program was a charge loss correction factor (CLCF) to account for charge losses during hole transport to the cathode.

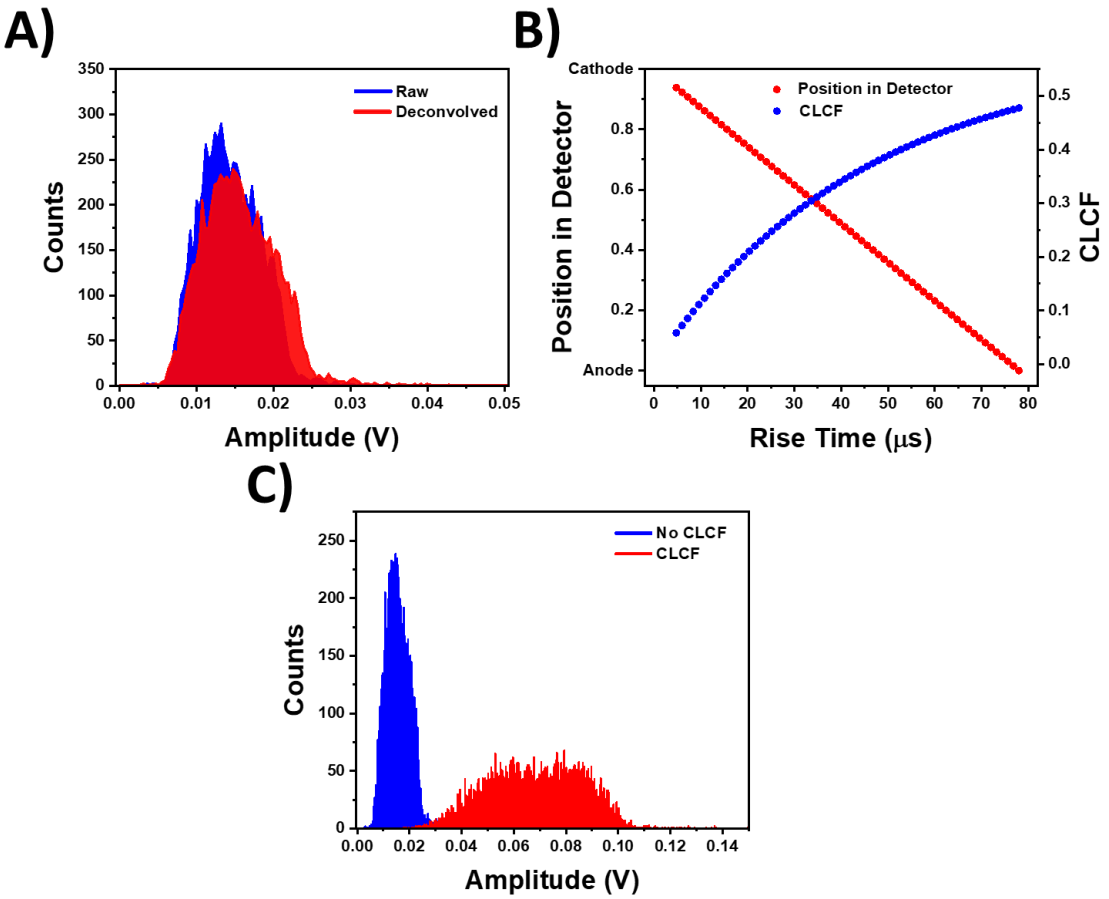

Figure 3.5.3. A) Spectra before and after applying deconvolution to the raw traces using Equation 3.1.1, B) Correlation of position within the detector and CLCF values to signal rise time, C) Post-deconvolution spectra before and after the CLFC was applied

The CLCF is derived from the Hecht equation that describes losses in charge collection efficiency due to trapping, and is shown in Equation 3.5.3 where Q_{0h} is the corrected charge induced by holes, Q is the charge generated that is assumed to be proportional to the pulse amplitude following deconvolution, λ_h is the hole drift length, d is the detector thickness, and x is the position within the detector. After correlating the depth of interaction with the rise time as shown in Figure 3.5.3B, the CLCF was calculated for each trace and applied to produce the charge induced on the electrode without charge trapping. Figure 3.5.3C shows that there is a noticeable effect in increasing the observed charge when the CLCF is applied, although no significant enhancement to spectroscopic performance was observed. While the deconvolution corrects for signal loss in the preamplifier output due to slow hole mobility and the CLCF corrects for depth dependent charge losses during hole transport, these two corrections do not address the primary issue causing the poor spectroscopic performance in MAPB, which is the depth dependent loss of electron contributions to the radiation induced signals. As stated in Chapter 1.2, the depth dependence of hole signal induction as a result of poor electron transport is the primary reason for the lack of spectroscopic response to highly penetrating radiation in compound semiconductors with a linear weighting field. Therefore, accounting for this effect in the spectrum requires either minimization or compensation for the lost electron signal.

$$Q_{0h} = \frac{Q}{CLCF} = \frac{Q}{\frac{\lambda_h}{d}\left(1 - e^{-\frac{(d-x)}{\lambda_h}}\right)} \tag{3.5.3}$$

Compensating for Lost Electron Contributions to Radiation Induced Signals

Two methods were evaluated to minimize and compensate for the effect of lost electron contributions to the signal from the spectra. The first was by simply building the spectra with only the traces with the longest rise times. From the correlation of rise time to depth of interaction in Figure 3.5.3B, the longest rise times represented the interactions that occurred furthest from the collecting cathode. As discussed in Chapter 1.2, the induced signal from interactions near the non-collecting anode would be due almost exclusively to the drift of holes, which minimizes the signal losses from the lack of electron induced signals and is a more accurate representation of the true

charge generated Q_0 [19]. Figure 3.5.4A shows minimal spectral differences without a photopeak when the spectrum was built with only the traces that were in the top 10% longest rise times prior to the application of the CLCF. While this method is computationally simple and the fraction of traces can be decreased in order to narrow the range to be closer to the non-collecting anode, it is not suitable for two reasons. First, the counting efficiency is lowered since the vast majority of traces are discarded, which would require significantly longer count times in order to mitigate this effect. Secondly, decreasing the detection volume reduces the likelihood of full energy deposition of the 662 keV ^{137}Cs gamma ray, which is a detriment to spectroscopic performance. As a result, post-processing methods that did not result in significant losses to detection volume and efficiency were desired.

The second method avoids the efficiency losses with the first method by applying a depth correction factor (DCF) that compensates for the variation in lost electron contributions due to the depth dependence of the gamma ray interactions, as shown in Equation 3.5.4 where d is the detector thickness and x is the position within the detector. For example, holes spawned from a gamma ray interaction in the center of the detector traverse half the distance compared to holes spawned at the non-collecting anode and as such, induce half the charge. Assuming a linear weighting field within the planar detectors, the same relationship holds for holes spawned anywhere within the detector. The DCF compensates for the reduced induced charge from the shorter drift distance by scaling the magnitude of the induced charge relative to the induced charge from holes spawned the non-collecting anode, which is assumed to be the signal with the longest rise time. The DCF as a function of the depth of interaction is shown in Figure 3.5.4B. Applying the DCF to the signal amplitude after the CLCF had been applied resulted in the spectrum shown in Figure 3.5.4C, which resulted in a drastic difference in spectral shape that had several notable features. The two small peaks between 0.1 V and 0.4 V were potentially the backscatter peak and Compton edge. However, the 32 keV X-ray peak was not identifiable within the lower channel numbers as expected. A possible explanation for this occurrence can be found in Figure 3.5.2E, which shows that the majority of traces unsuitable for processing due to noise and pileup were in the lower channel regions. As a result, the collection of low energy radiation induced signals was in competition with the electronics triggering off of noise, which significantly decreased the

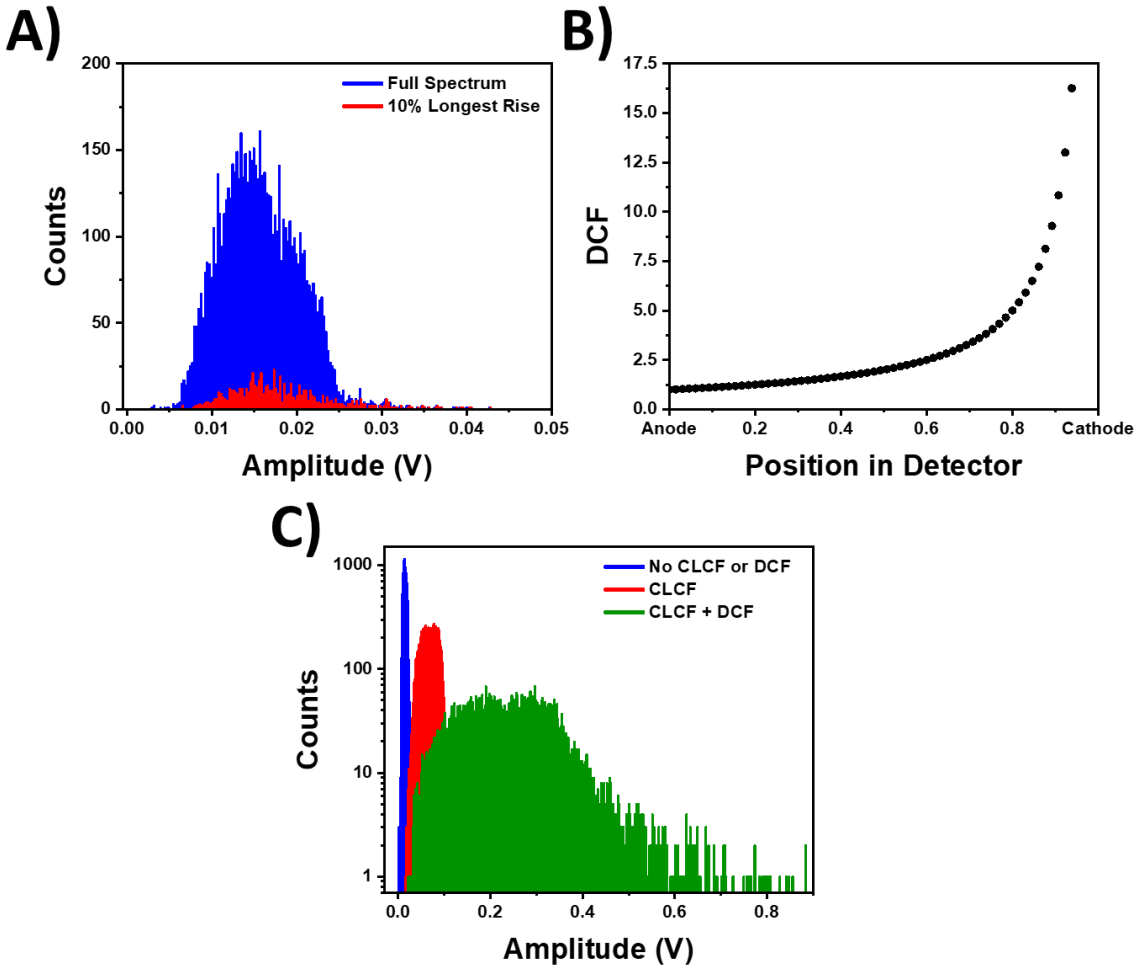

Figure 3.5.4. A) Comparison between the full spectrum and the spectrum generated from signals with the 10% longest rise times, B) DCF as a function of position within the detector, C) Post-deconvolution spectral comparisons with no CLCF or DCF applied, only CLCF applied, and both CLCF and DCF applied

efficiency of collecting low energy signals. Most importantly, however, the spectrum still lacked both a clear 662 keV full energy peak (FEP) along with the Pb escape peak, although there did appear to be a number of counts beyond the Compton edge that could have resolved into a photopeak with a greater quantity of counts. While it was possible that poor energy resolution resulted in the FEP being spread out over too many channels, the counts beyond the Compton edge only accounted for less 1.1% of the total counts in the spectrum, whereas the number should be approximately 10 times higher according to MCNP simulations. Given the long duration of this experiment, it is possible that transient effects within the detector during operation such as ionic conductivity and polarization contributed to decreasing the CCE over time, which would not be mitigated by deconvolution, CLCF or DCF [45, 131, 155].

$$Q_0 = Q_{0h} \times DCF = Q_{0h} \times \frac{d}{d-x} \tag{3.5.4}$$

While the combination of deconvolution, CLCF, and DCF was shown to mitigate, at least in part, the effects of charge loss due to slow rise time, trapping during transport, and depth dependent interactions respectively, the lack of a clear photopeak within these results indicated several areas in need of improvement to increase the efficiency of the MAPB detection systems for gamma ray sensing using the processing described in this section. First, a significant quantity of the collected traces had to be discarded since they were of poor quality and contained noise and pileup. Improvements to the pulse processing chain to include faster electronics and properly set trigger thresholds are relatively easy to achieve and can increase efficiency of data collection. Second, detector stability under longer collection times is a necessity for both collecting a sufficient number of radiation-induced signals to observe a photopeak as well as minimizing transient effects that decrease CCE over time. Finally, if larger detection volume is desired in MAPB to increase the interaction probability, the hole transport values must increase as well. Subsequent sections will further discuss detector stability and improvements to hole transport in MAPB, as well as the effect that both have on detector performance.

3.6. Neutron Sensing

While fast neutron sensing had been previously demonstrated in MAPB due to the 50% atomic fraction of hydrogen [45], the incorporation of lithium directly into the MAPB perovskite structure allowed for the detection of thermal neutrons through the $^{6}Li(n,\alpha)^{3}H$ thermal neutron capture reaction. Natural lithium, however, is only 7% ^{6}Li and 93% ^{7}Li. As a result, a 2.5% substitution with natural LiCl precursors resulted in a LiMAPB detector with a ^{6}Li atomic fraction less than 0.015% (less than 150 ppm) as shown in Table 3.6.1. Despite the low fraction of thermal neutron sensitive constituents, exposure of the LiMAPB sensor to a moderated 2 Ci plutonium beryllium (^{239}Pu/Be, hereafter referred to as PuBe) neutron source yielded positive results for thermal neutron sensing.

The experimental setups utilized are shown in Figure 3.6.1 and depict the various shielding configurations implemented to isolate the thermal neutron component of the acquired spectra. For neutron sensing, the detector was biased at -60 V throughout all experiments, and a ten-minute background radiation measurement was taken before 30-minute radiation measurements for each of the three configurations. The first configuration, shown in Figure 3.6.1A, moderated the PuBe fast neutrons via high-density polyethylene (HPDE) and observed the changes in the spectral response of the LiMAPB sample with and without a 1.6 mm thick cadmium thermal neutron shield. The second measurement configuration in Figure 3.6.1B incorporated lead to shield the detector from the 4.44 MeV gamma ray emitted by the PuBe source, and 2.1 MeV gamma rays from hydrogen capture. Each lead brick was 2 inches thick, and a “cage” was created by placing one layer of lead bricks above and on the sides of the aluminum test box, while two layers of bricks were placed between the HDPE and the bottom of the test box. Finally, the third measurement configuration in Figure 3.6.1C placed the cadmium shield between the double layer of lead bricks to shield the detector from the neutron-induced capture gamma rays from the cadmium shield. The various shielding configurations illustrated in Figure 3.6.1 were designed with the intent of isolating the spectral components that could be attributed to thermal neutrons. Specifically, it was expected that there would be four main components to the spectra in addition to background: unmoderated fast neutrons, moderated thermal neutrons, and gamma rays from the PuBe source and $^{113}Cd(n,\gamma)^{114}Cd$ and $^{1}H(n,\gamma)^{2}H$ neutron capture reactions. The shielding configurations were

Table 3.6.1. LiMAPB Atomic Fractions

H	^{6}Li	^{7}Li	C	N	Cl	Br	Pb
49.5%	0.0148%	0.197%	8.25%	8.25%	0.21%	25.2%	8.46%

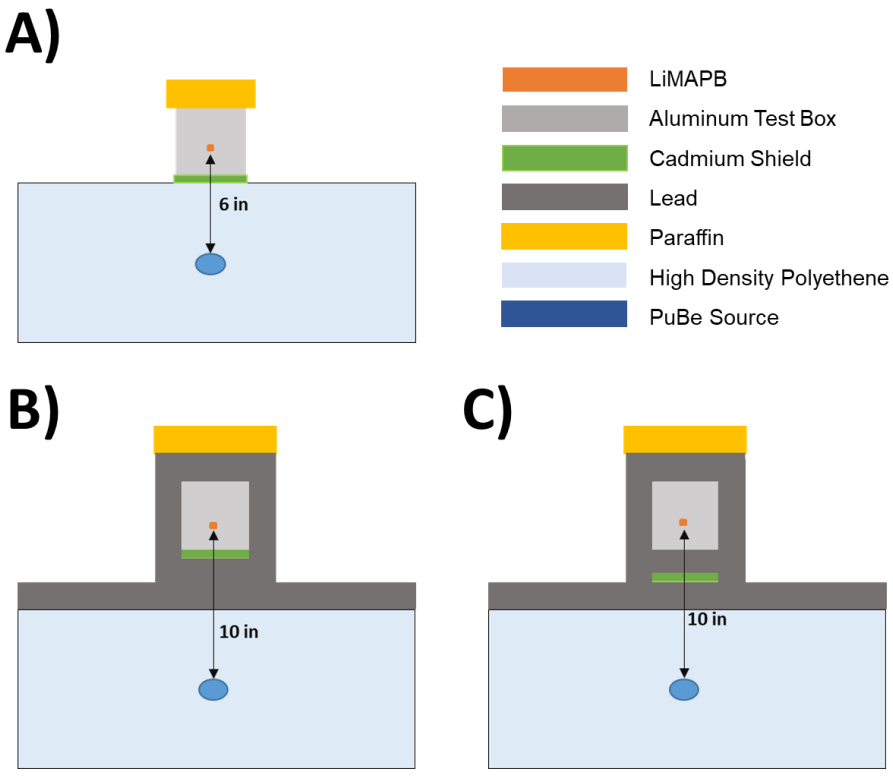

Figure 3.6.1. Shielding arrangement for thermal neutron sensing with the PuBe neutron source: A) Setup A: No lead shielding, B) Setup B: Addition of lead shielding, and C) Setup C: Cadmium shield between lead shielding

designed with the intention of methodically minimizing the contributions from each radiation component, and the results demonstrated that thermal neutron sensing is possible in LiMAPB, even at a very low atomic fraction.

The LiMAPB sample was first exposed to the PuBe source with and without the cadmium shield in the configuration from Figure 3.6.1A. Cadmium (specifically ^{113}Cd which makes up 12.22% of natural cadmium) has a large cross section, making it an effective thermal neutron absorber. The resulting spectra from this experiment are shown in Figure 3.6.2A, where a significantly smaller fraction of counts was observed in the higher channels following the addition of a cadmium shield. It was likely that the $^{6}Li(n,\alpha)^{3}H$ reaction fully deposited 4.78 MeV in the detector volume distributed between the two heavy charged particles, however, no spectral features would be observed due to the neutron penetration depth and poor carrier properties. Regardless, the difference in spectral shape indicated that the nature of radiation interactions with and without the cadmium shield were different as well. While this could have potentially been attributed to the removal of thermal neutrons through the cadmium shield, the thermal neutron contribution could not be definitively isolated due to the gamma ray cascade that was also produced by the $^{113}Cd(n,\gamma)^{114}Cd$ thermal neutron capture. Moreover, the gamma rays produced by the PuBe source itself contributed significantly to the signal and could have potentially masked any thermal neutron interactions. Figure 3.6.2B shows that the incorporation of 4 inches of lead shielding (two rows of 2-inch lead bricks) had a significant impact in attenuating energetic gamma rays from the PuBe source, as the fraction of counts outside of the lowest energy region is clearly lower. This drop off was not due to a lower geometric efficiency from increasing the total source-to-detector distance from 6 inches to 10 inches. Since no decrease in total count rate was observed upon adding the lead shielding, it could be concluded that the radiation flux from the PuBe source was significantly high enough to overcome the approximately threefold decrease in geometric efficiency.

The final neutron test applied the conclusions from the previous tests to construct a shielding configuration that would minimize contributions from both PuBe and ^{113}Cd gamma rays, which was shown in Figure 3.6.1C. This test consisted of three trials summarized in Table 3.6.2, with the shaded regions identifying the shielded radiation. The red shading in Trial 1 indicates that there were no ^{113}Cd gamma rays present which is not due to any shielding design, but simply

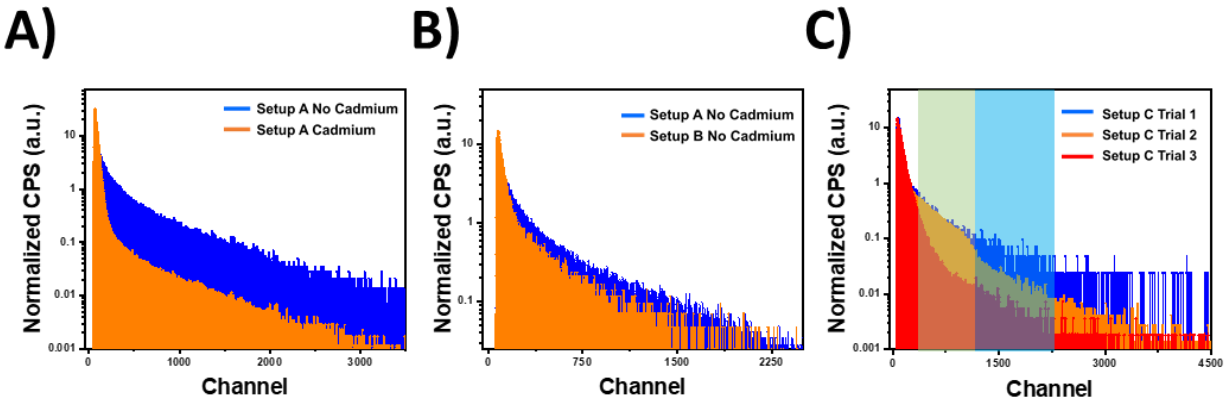

Figure 3.6.2. A) Response to PuBe with and without the cadmium shield with the setup from Figure 3.6.1A, B) Response to PuBe with and without 4 inches of lead shielding, C) Response to PuBe with configurations as summarized in Table 3.6.2

Table 3.6.2. Summary of PuBe Neutron Tests

Trial Number	Description	Shielded Radiation Component			
		PuBe γ	Thermal n	^{113}Cd γ	Fast n
1	No Cd Shield				
2	Cd Shield Below Sample				
3	Cd Shield Between Two Lead Bricks				

because there was no Cd present at all. Comparing the spectra in Figure 3.6.2C with the descriptions provided in Table 3.6.2 yielded two notable results. First, Trials 2 and 3 showed a slight difference in normalized counts in the lower to middle regions of the spectra (gray shaded region) when the detector was not shielded from the ^{113}Cd gamma rays. The gamma rays from the capture reaction have a maximum energy of 9.20 MeV, which are much too high to be stopped within the detector. However, a very large fraction of the gamma ray cascade has energies below 600 keV [161, 162]. While no spectroscopic peaks were resolved (similar to the discussion on Figure 3.5.1A), these relatively lower energy gamma rays still produced spectral features that could be identified. The second result was more notable, which was that comparison of the spectra from Trials 1 and 3 potentially showed a thermal neutron component. Trial 3 shielded, at least to some degree, each of the radiation components of interest except fast neutrons. The spectrum from Trial 1, on the other hand, showed the response to both fast and thermal neutrons. The difference in normalized count rates between these two spectra were most notable in the higher channel regions (blue shielded region), which was similar to the spectra in Figure 3.6.2A. Since the gamma ray contributions from ^{113}Cd had already been identified to reside in the lower regions and the PuBe gamma rays had been significantly shielded, the count rate differences in the higher channels of Figure 3.6.2C could be identified as potential thermal neutron contributions with a higher degree of confidence.

To further demonstrate that LiMAPB was sensitive to thermal neutrons, the sensor was exposed to the Ohio State University Research Reactor (OSURR) thermal neutron beam. OSURR is a light water research reactor capable of reaching 500 kW-thermal power levels, and its thermal neutron beam is formed by collimation with a series of borated aluminum and lead disks, all with a 3.0 cm diameter aperture. Fast neutrons are filtered with a single-crystal sapphire 12.7 cm in length and 10.16 cm in diameter, and gamma rays are filtered with a single block of polycrystalline bismuth 10.0 cm in length and 12.82 cm in diameter. Additionally, the beam can be turned on and off using an external shutter made of borated aluminum, borated polyethylene, and lead [163]. With sufficient gamma ray shielding, 97% attenuation of fast neutrons [164], and a thermal neutron flux of 3.4×10^6 n cm^{-2} s^{-1} at 450 kW-thermal at the sample location, changes in response of LiMAPB with the shutter opened and closed could be primarily attributed to thermal neutrons with

a high degree of confidence. For the experiments at OSURR, the detector was placed approximately 4 cm from the beam port, and the current was measured and -85 V bias applied with a Keithley 2612A Source Measure Unit.

Figure 3.6.3 shows the transient current response of LiMAPB to the OSURR thermal neutron beam with the reactor power at 450 kW-thermal as well as the shutdown period. With the shutter in the open position (green shading), there was a clear increase in the induced current above the current observed when the shutter was closed (red shading). This difference was also observed when the shutter was closed for a short period during the reactor shutdown procedure. The fact that the closed shutter current was virtually identical to the observed current after reactor shutdown indicated that the LiMAPB response with the shutter open was primarily due to the thermal neutron beam, which was designed and shown to contain low levels of fast neutron and gamma ray contamination [163, 164]. Both the OSURR thermal neutron beam exposure results and the PuBe exposure pulse height spectrum in Figure 3.6.2C show observable differences in detector response when the thermal neutron components are isolated, even with less than 0.015% atomic fraction of ^{6}Li. Moreover, the I-V measurements shown in Figure 3.6.3B before and after the 7 minutes of measurements in Figure 3.6.3A do not show an increase in dark current. On the contrary, the dark current and bulk resistivity appear to improve following exposure to the OSURR thermal neutron beam, which demonstrates the stability of LiMAPB under thermal neutron irradiation. This could potentially be due to the coexistence of deep traps and both donor and acceptor shallow energy levels from radiation induced point defects that act as dopants, which has been shown in proton irradiated $MAPbI_3$ to result in partial self-compensation that would result in increased resistivity [42, 116]. These results demonstrate the stability of LiMAPB under irradiation and indicate that LiMAPB holds significant potential for thermal neutron sensing if incorporation of ^{6}Li can be increased, whether by potentially utilizing precursors enriched in ^{6}Li during growth or by directly increasing the lithium content without significantly degrading structural and electronic stability or radiation sensing performance.

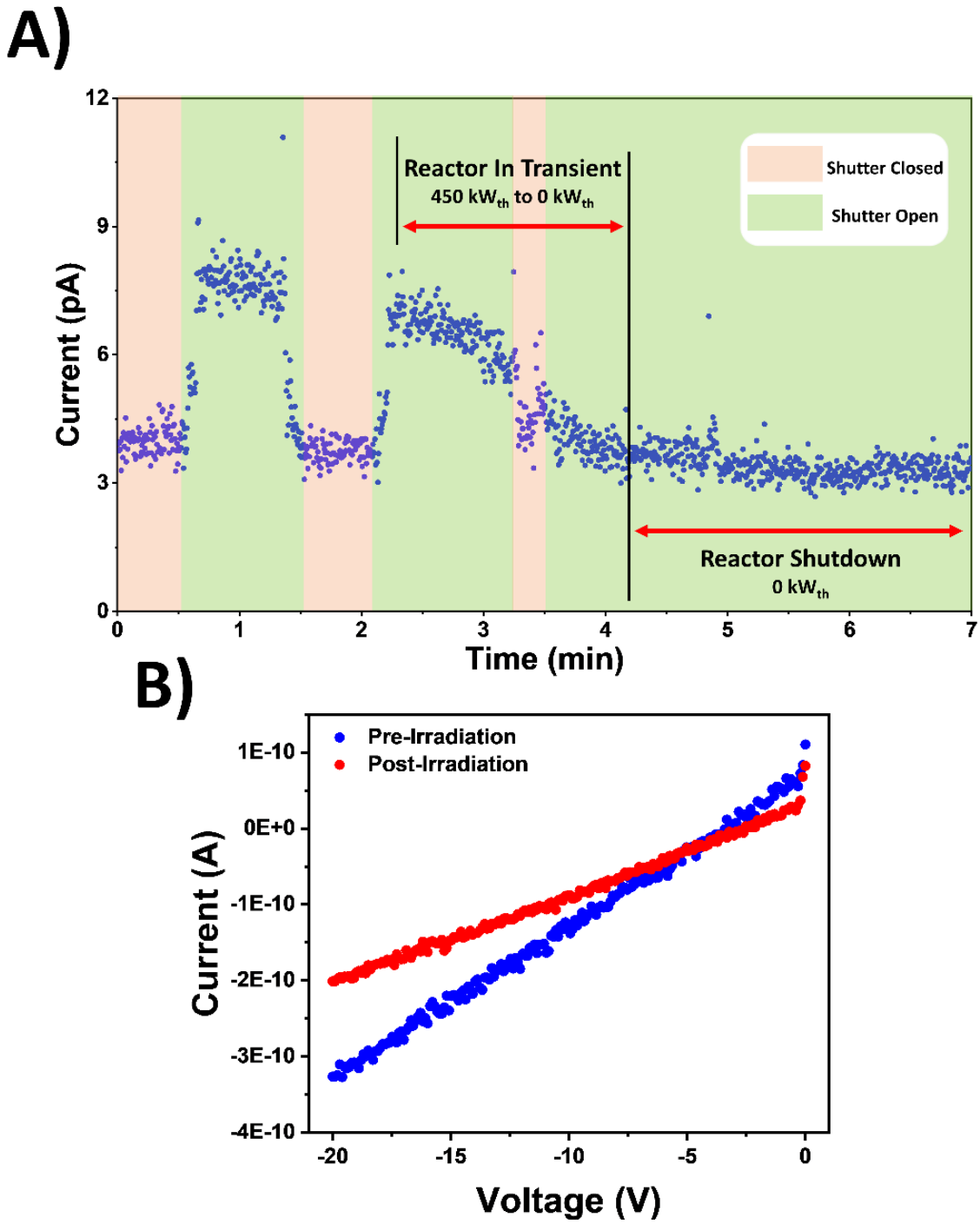

Figure 3.6.3. A) Transient current response of LiMAPB to thermal neutrons from OSURR with shutter in the open and closed position, B) I-V measurements of LiMAPB before and after the measurements in Figure A

3.7. Mitigating Performance Degradation

Understanding the mechanisms by which the radiation sensing capabilities of MHP detectors degrade over time is critical in developing mitigation strategies to prolong detector lifetime, enhance stability, and maintain performance. This section will present radiation damage as a source of detector degradation, followed by annealing and low temperature operation to both mitigate losses in radiation detection capabilities and improve detector performance in general.

Radiation Damage

Ionic conductivity as a performance degrading phenomenon had been previously introduced in the section discussing the implementation of tin oxide interfacial layers into the electrode scheme, where mobile bromine ions in MAPB could react with metallic contacts to form metal-halide complexes that distort the electric field in the absence of any blocking layers [45, 46, 110, 152-155]. Another phenomenon to consider when operating detectors in high count rate environments is radiation damage, which can induce traps and defects that limit detector performance. To qualify the effect that radiation damage had on the performance of MAPB perovskite material, the charge transport properties of a 5.1×5.4×1.8 mm^3 $MAPbBr_{2.85}Cl_{0.15}$ SC via ^{210}Po alpha particle irradiation were evaluated at -50 V bias before and after exposure to X-rays incident on the cathode at a distance of 0.5 mm with a dose rate of 2.22 Gy s^{-1} for a period of 5 minutes, resulting in a total dose of 6.65 kGy. The alpha spectra in Figure 3.7.1A show a nearly 17-fold decrease in apparent charge collection efficiency based on the alpha peak channel number following X-ray irradiation, and trace analysis showed that the apparent (effective) hole mobility [45] had decreased by over half from an average value of 27.4 to 15.1 cm^2 V^{-1} s^{-1} before and after irradiation as shown in Figure 3.7.1B. From these results, it can be concluded that the exceedingly high dose rate for this experiment caused the accumulated dose to quickly exceed the reported thresholds at which significant damage begins to occur in perovskites, which led to the rapid degradation in radiation detection performance. Although the results from Figures 3.4.2C and D from Chapter 3.4 showed that the sensitivity of the MAPB wafer detectors remained relatively robust when operated at more reasonable dose rates, which bodes well for its potential use for imaging applications, the long-term accumulation of dose can still induce performance

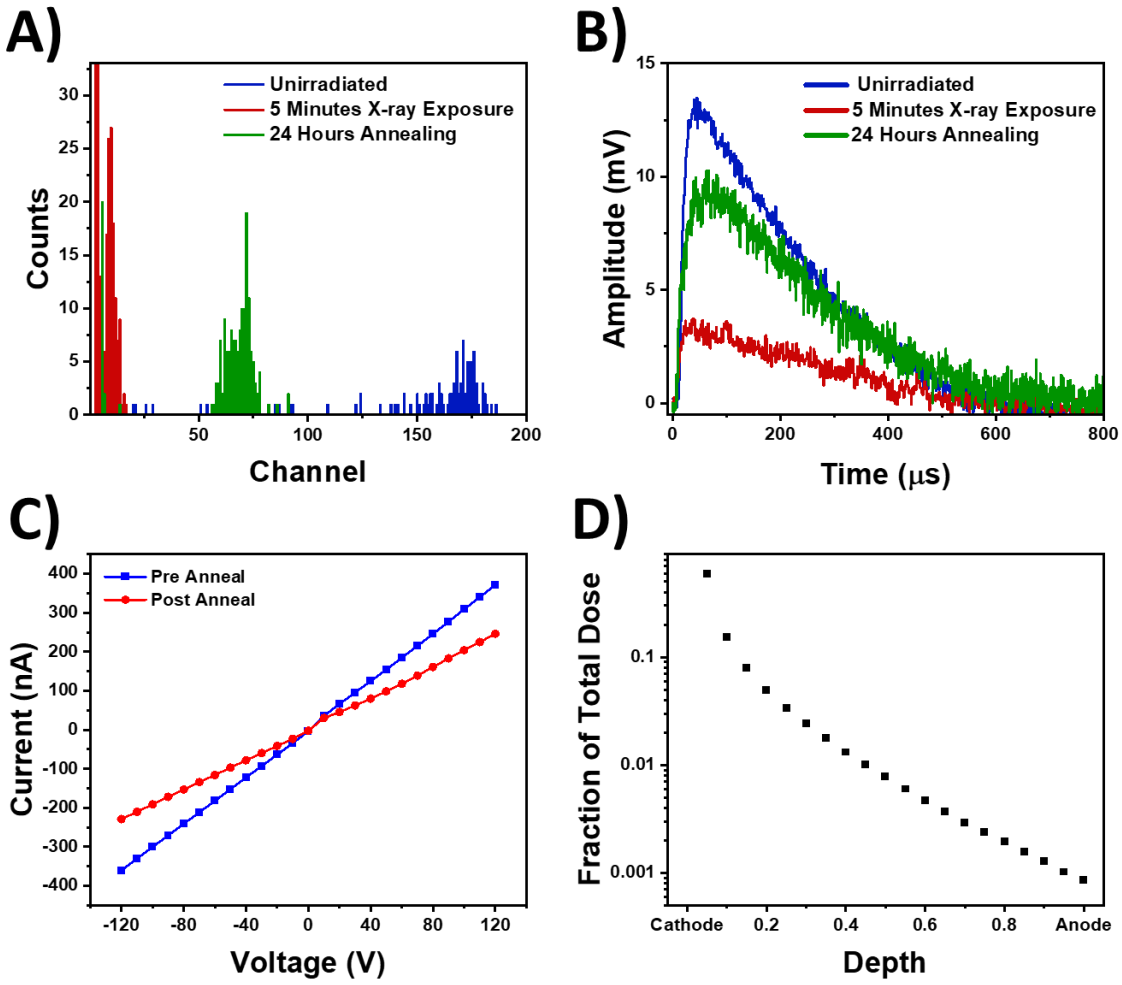

Figure 3.7.1. Alpha response of $MAPBBr_{2.85}Cl_{0.15}$ at -50 V. A) Alpha spectra before and after 5 minutes of X-ray irradiation at 2.22 Gy s^{-1} showing decreased CCE, with a partial restoration of CCE following annealing (Gain: 100, Shaping Time: 10 μs, 120 s), B) Traces from alpha radiation before and after X-ray irradiation, as well as after annealing, C) I-V measurements of $MAPbBr_{2.85}Cl_{0.15}$ before and after annealing, D) MCNP simulation of the X-ray dose received by the $MAPBBr_{2.85}Cl_{0.15}$ as a function of detector depth

degradations. The remainder of this section will present the evaluation of annealing and low temperature testing as potential methods to both mitigate radiation induced degradations as well as enhance radiation detection performance in general.

Annealing

Annealing of perovskites has been reported to be instrumental in reducing defect density, dark current, leading to healing of radiation damage and improvements to detector performance and stability [165-167]. To observe these effects, the performance of the irradiated $MAPbBr_{2.85}Cl_{0.15}$ SC detector was evaluated before and after annealing for 24 hours at 125°C in an N_2 environment within an oven. As shown in Figure 3.7.1C, annealing the sample resulted in a bulk resistivity increase from 5.03×10^8 Ω-cm to 7.77×10^8 Ω-cm, which was correlated with a lower dark current through the bulk of the detector. The alpha spectrum after annealing in Figure 3.7.1A also shows a clear increase in apparent CCE by nearly 7-fold following the annealing, although the restoration is only 41% of the apparent CCE prior to irradiation. There are two potential explanations for this phenomenon. First, annealing may have led to improvements in mobility by reducing ionized impurity scattering [166], which would explain the nearly 15% in apparent mobility following annealing from 15.1 to 17.6 $cm^2\ V^{-1}\ s^{-1}$. It is also possible that the annealing, which is known to also reduce antisite defect density and reorder ions within the perovskite structure [166], mitigated radiation induced traps that produced polarization effects within the detector. According to MCNP simulations of the experiment, nearly 75% of the total dose was absorbed within the first 10% of the detector and 90% absorbed within the first 25% as shown in Figure 3.7.1D. Given that the collecting cathode was also the irradiated face of the detector, it is reasonable to assume that the majority of the radiation induced defects existed in this region and acted as traps. Similar to the polarization effects observed in CZT detectors under intense X-ray irradiation [168-170], the increased trapping of holes near the cathode during transport resulted in an accumulation of positive space charge that competed with the externally applied electric field, resulting in a diminished CCE due to the decreased internal electric field. Annealing the detector potentially reversed these polarization effects to a certain extent by reducing the defect density, which led to the partial restoration of CCE.

While these results demonstrate the potential benefits of annealing in reducing defects and trap states, control over the annealing process is critical in ensuring its effectiveness. Previous reports of annealing perovskites have shown increase to the SRV by nearly threefold as a result of the annealing, as well as degradation of MHPs into their lead halide constituents [166, 171]. Figures 3.7.2A-D show two pure MAPB SCs (referred to as MAPB SC 1 and 2 within this section) before and after 2 hours of annealing at 125°C in an argon environment within a tube furnace. Upon removal from the tube furnace, it was observed that the detectors were coated with a yellow particulate, which can be seen in Figure 3.7.2E with the original red hue seen in the cleaved section for comparison. It was assumed that the particulate was $PbBr_2$ based on previous reports of MHP surface degradations [171]. Polishing off the majority of the particulate with DMF revealed that the crystal surfaces had significantly degraded as well through the formation of inclusions that made removal of the particulate difficult, which can be seen in Figures 3.7.2B and D.

Figure 3.7.3A shows the I-V behavior of MAPB SC 2 before and after annealing, with the abscissa and ordinate as electric field and current density respectively instead of voltage and current in order to account for the difference in dimensions ($7.2\times7.0\times3.0$ mm^3 before annealing and $7.1\times7.0\times2.7$ mm^3 after annealing) given that the crystals required significant repolishing to remove the particulates. The trends show an increase in dark current density after annealing, which could potentially be due to increased leakage current at the surface due to physical defects [58]. Meanwhile, alpha spectra taken before and after annealing at -110 V and -100 V respectively to maintain similar electric field strengths showed a 40% decrease in apparent CCE after annealing based on the peak locations in Figure 3.7.3B. Trace analysis at electric field strengths of 530 V/cm and 660 V/cm in Figures 3.7.3C and D respectively show a significant decrease in pulse amplitude after annealing as expected from the alpha spectra. At the same time, however, the TCC that was extremely prominent in the traces prior to annealing appeared to be significantly reduced after annealing. Additionally. the fast component of the traces prior to the onset TCC, which represents the transport of the untrapped charge cloud through the detector [45], decreased in rise time by 64% and 57% after annealing at electric field strengths of 530 V/cm and 660 V/cm respectively. These results suggest two things. First, the annealing was effective in reducing defect states within the crystal bulk that both contributed to TCC and acted as scattering centers during hole transport,

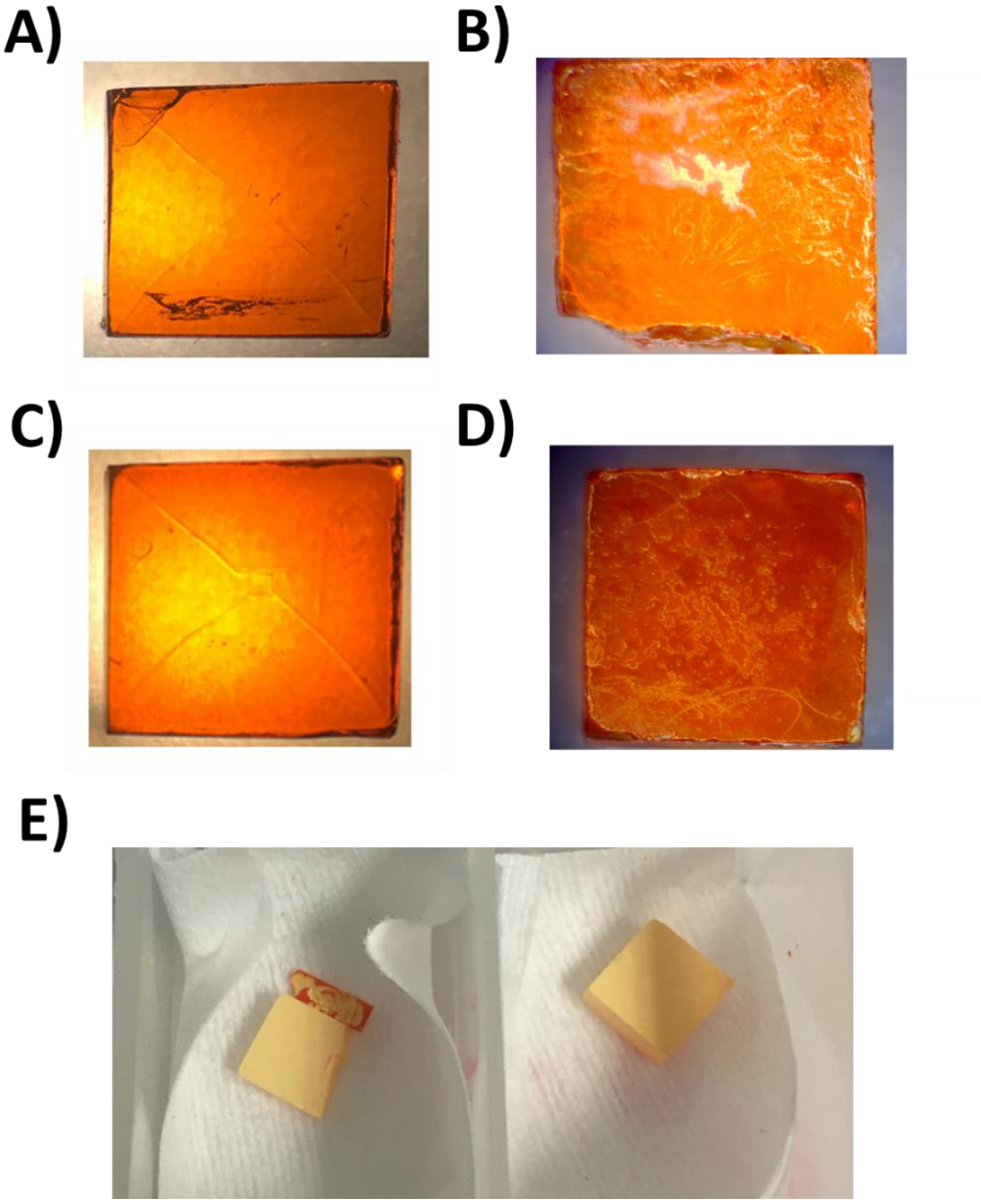

Figure 3.7.2. Images taken before annealing and after annealing with DMF polishing for A-B) MAPB SC 1 and C-D) MAPB SC 2, E) MAPB SC 1 (left) and 2 (right) immediately after removal from tube furnace with yellow particulate coating the surface

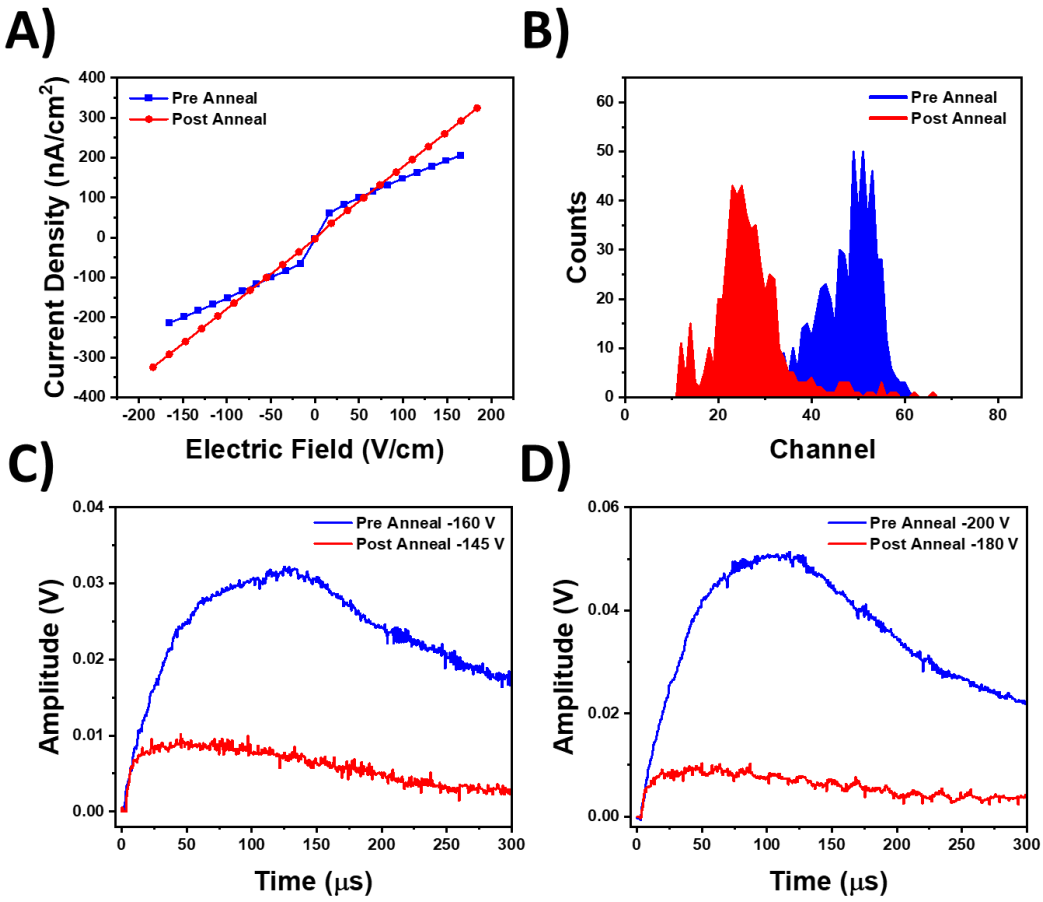

Figure 3.7.3. A) Current-voltage behavior of MAPB SC 2 before and after annealing, B) Alpha spectra before and after annealing at -110 V and -100 V respectively to maintain similar electric field strengths (Gain: 25, Shaping Time: 12 μs, 60 s), Alpha particle induced traces at electric field strengths of C) 530 V/cm and D) 660 V/cm

which led to the minimization of the slow component within the preamplifier pulse and increase in apparent mobility. At the same time, the decreased amplitude could have been due to the severe degradations to the crystal surface that acted as recombination centers and decreased the observed CCE [58, 81]. While the TCC hindered the ability to evaluate changes to SRV after annealing through Many equation fitting using the deconvolution techniques as described in Chapter 3.1, the results demonstrated the importance of controlling the annealing process in order to maximize the effectiveness of the process and minimize surface degradations that lead to decreased CCE.

Low Temperature Testing

In addition to annealing, operating devices at lower temperatures is another post-fabrication method for improving radiation sensing performance. It is understood that the level of phonon scattering decreases at lower temperatures, which leads to a higher mobility in the absence of significant trap concentrations [165, 172]. For high quality sensors, such as the LiMAPB sample shown in Figure 3.1.1B, the enhanced mobility at lower temperatures can lead to apparent increases in charge collection efficiency given that the level of ballistic deficit is reduced. Figure 3.7.4 shows the alpha particle induced radiation response at -60 V from the LiMAPB detector at room temperature (20°C) and at 0°C. From the traces in Figure 3.7.4A, the average hole mobility increased from 7.20 $cm^2\ V^{-1}\ s^{-1}$ to 9.29 $cm^2\ V^{-1}\ s^{-1}$ after lowering the detector temperature, which is an enhancement of nearly a 30%. As discussed in Chapter 2, the higher hole mobility results in both greater preamplifier pulse amplitudes as well as a larger component of the amplitude integrated within the shaping time of the amplifier. Figure 3.7.4B shows enhanced apparent charge collection efficiency of over 60% as evident by the alpha peak shift at lower temperatures.

Temperature dependent alpha peak shifting behavior was also observed to a lesser degree in the irradiated $MAPbBr_{2.85}Cl_{0.15}$ detector from previous sections section tested at 20°C, 0°C, and -20°C, which is shown in Figure 3.7.5A. However, the poor birefringence quality shown in Figure 3.7.5B along with the fact that this sample had been previously exposed to 6.65 kGy of X-ray radiation indicated that the bulk likely contained a greater defect density than the LiMAPB detector. Since this could be correlated with a greater trap concentration, another low temperature phenomenon in addition to decreased phonon scattering must be considered. It had been previously

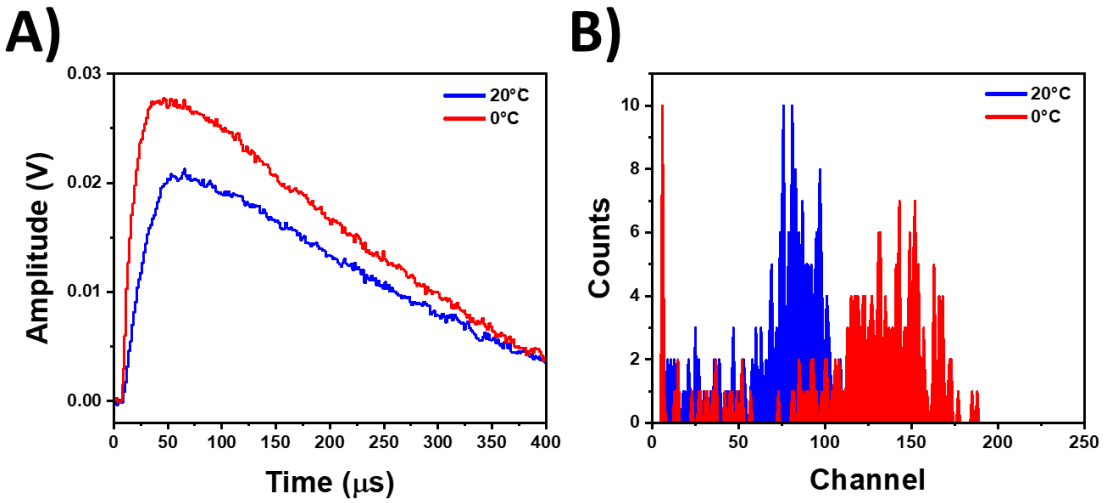

Figure 3.7.4. A) Preamplifier traces from LiMAPB detector exposed to ^{210}Po alpha particles at -60 V showing a faster rise time at 0°C compared to room temperature B) Alpha spectrum of the same experiment with ^{210}Po alpha source (Bias: -60 V, Gain: 50, Shaping Time: 10 μs, Count Time: 120 s)

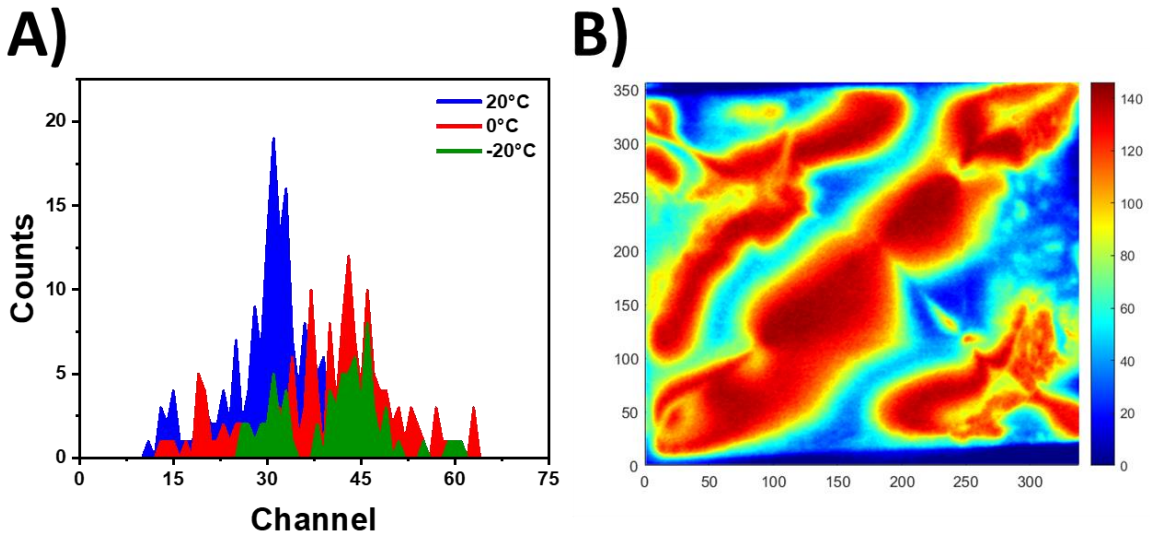

Figure 3.7.5. A) Alpha spectrum with noise floor removed at various temperatures in $MAPbBr_{2.85}Cl_{0.15}$ with ^{210}Po alpha source (Bias: -50 V, Gain: 100, Shaping Time: 10 μs, Count Time: 120 s) B) Birefringence image of the $MAPbBr_{2.85}Cl_{0.15}$ detector showing poor quality

reported in CVD diamond detectors that lowering the temperature increases the detrapping time constant by suppressing the rate of thermally activated detrapping from shallow traps [173, 174]. Since the detrapping time constant (τ_D) determines how long the carriers remain trapped, a smaller value for τ_D at higher temperatures indicates a more rapid detrapping process that leads to faster signal rise, improved pulse quality, and higher charge collection efficiency. Conversely, the increasing levels of TCC with decreasing temperature observed by Marinelli demonstrated that the lower temperatures were decelerating the detrapping process and deteriorating the alpha particle induced signals in CVD diamond [173]. Similar effects have been shown in MAPB, where enhancements to apparent mobility from decreased phonon scattering at low temperatures compete with carrier detrapping that lowers the effective mobility. Moreover, the same work reported that at temperatures below 250 K, the detrapping activity is essentially "frozen" in MAPB [172]. However, there have not yet been reports to date that demonstrate how these phenomena affect the ionizing radiation sensing performance of MAPB.

Table 3.7.1 shows the temperature dependent changes in both the average rise time and amplitude of the fast component of the alpha particle induced signal prior to the slow TCC component at 20°C, 0°C, and -20°C in the $MAPbBr_{2.85}Cl_{0.15}$ detector as determined through trace analysis. The fast component, which represents the motion of the un-trapped charge cloud being transported through the detector [45], allowed for observation of temperature dependent changes in charge transport when the effect of detrapping was largely removed. The clear trend of decreasing fast component rise times following decreasing temperature is evidence that carrier mobility increased in the absence of detrapping effects as expected [165, 172]. It should be noted here that the reason why signal rise times were reported instead of mobility values was that an FFT filter was used in this particular analysis to remove high frequency noise from the traces. Although FFT preserved much of the original signal and allowed for a clearer analysis of the different signal components as shown in Figure 3.7.6A, this analysis was concerned with the relative changes between FFT-processed traces at different temperatures to avoid potentially spurious comparisons of mobility values to other analyses that did not utilize FFT.

Meanwhile, the FFT-processed traces in Figures 3.7.6A-C show that the presence of TCC could be observed to some degree in the traces at all three temperatures, with the slow component

Table 3.7.1: Average Fast Component Trace Parameters at Different Temperatures in $MAPbBr_{2.85}Cl_{0.15}$ Before and After Annealing

Temperature (°C)	Annealing	Fast Component Rise Time (μs)	Fast Component Amplitude (mV)
20	Pre	61.7 ± 4.3	2.6 ± 0.2
20	Post	39.5 ± 3.6	8.3 ± 0.5
0	Post	36.5 ± 1.1	6.4 ± 0.5
-20	Post	31.8 ± 3.3	5.6 ± 0.5

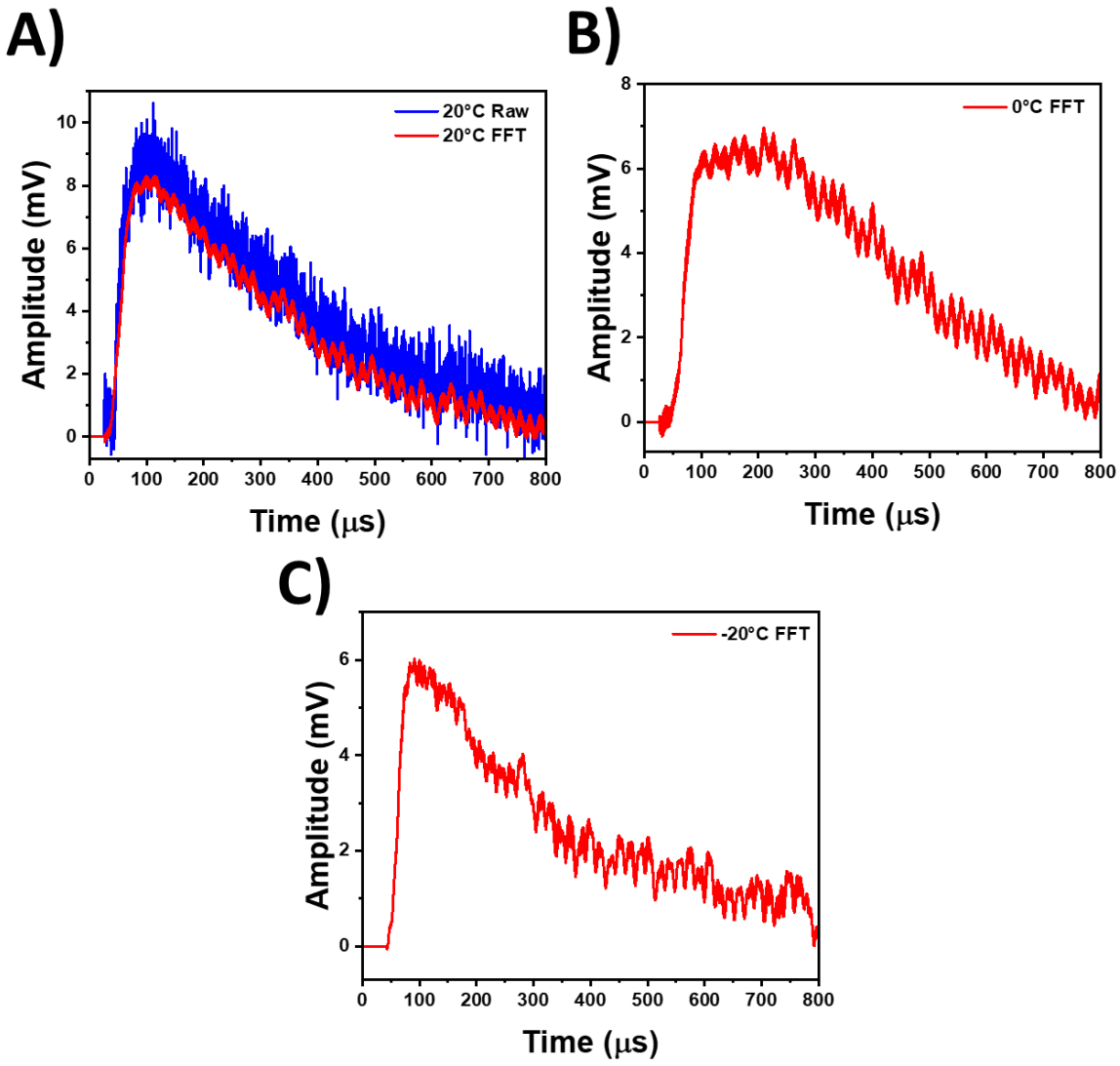

Figure 3.7.6. ^{210}Po alpha particle induced traces at -50 V bias in $MAPbBr_{2.85}Cl_{0.15}$ A) Comparison of unaltered trace and FFT-processed trace at 20°C, B) FFT-processed trace at 0°C, C) FFT-processed trace at -20°C

of the rise becoming more prominent at 0°C before becoming significantly less pronounced at -20°C. Although seemingly inconsistent, a potential explanation for the disappearance of TCC could be that lowering the temperature to approximately 250 K crossed a threshold where there was no longer enough thermal energy to de-trap the carriers that contribute to the signal, effectively removing the slow TCC component from the observed signals. As a result, the temperature dependent changes in the traces demonstrated the effects of both the suppressed thermal detrapping rate leading to a more pronounced slow component at lower temperatures as shown in CVD diamond [173, 174], as well as the "freezing" of detrapping activity in MAPB around 250 K [172]. The suppression of detrapping was also supported by the systematic decrease in fast component amplitude with decreasing temperature, as this could indicate that fewer and fewer carriers are de-trapped quickly enough to still be collected within the initial charge cloud, although decreasing pulse amplitude due to polarization cannot be ruled out. The shift in alpha peaks to higher channels in Figure 3.7.5A despite the decrease in pulse amplitude at lower temperatures could be reconciled by a greater amount of charge integrated within the 10 μs amplifier shaping time due to the faster rise of the fast component from the reduction in phonon scattering. Collectively, these results demonstrate that merely observing changes in the pulse height spectrum is insufficient to qualify the temperature dependence of MAPB radiation detection performance, as the interplay between decreased phonon scattering and suppressed charge carrier detrapping rate at lower temperatures can be masked by the pulse processing chain.

In summary, the results from the LiMAPB detector show that the temperature dependence of the mobility in high quality MPH SCs without high defect concentrations follows the phonon scattering dominated models, where mobility is increased at low temperatures from decreased phonon scattering and signal degradations from a suppressed detrapping rate are not significant. Meanwhile, the radiation response from the $MAPbBr_{2.85}Cl_{0.15}$ detector showed that when the trap concentrations are significant, the suppressed detrapping rate has a more prominent effect on the slow TCC component of the radiation induced signals, although the TCC component could potentially disappear once a temperature threshold is reached where there is not enough thermal energy to de-trap carriers that contribute to the signal. As a result, while other semiconductor radiation detectors such as CZT have previously shown mixed results with low temperature

performance [175, 176], the level of enhancement in MAPB at low temperatures has been shown to be strongly influenced by defect and trap concentrations.

Chapter 4: Summary

This dissertation presents the development of metal halide perovskites for radiation sensing in four sequential components. First, methods of improving detector fabrication processes were presented, followed by determination of charge carrier properties. The radiation sensing capabilities were then benchmarked, followed by the observed degradations to device performance and the post-fabrication techniques evaluated as mitigation strategies.

Detector Fabrication

Prior to detector fabrication, birefringence was shown to be an effective tool for rapid evaluation of bulk macroscopic crystal quality. Because the defects observed via birefringence were correlated with trap controlled conductivity at both room temperature and at lower temperature, the early identification of these features improved the rate of success in fabricating high quality sensors and improved the efficiency of the process. Improving the surface quality was the next step, as inhomogeneous surfaces were shown to lead to position dependent I-V behavior, large surface recombination values, and significant discrepancies between the charge transport properties derived from the Hecht and Many equations. Chemomechanical polishing with dimethylformamide (DMF) was shown to be effective in producing a mirror finish on MHP SCs and removing surface defects induced by essential mechanical polishing steps. These improvements to the surface led to fivefold reductions in surface roughness, as well as enhancements to operational stability, bulk resistivity, and apparent charge collection efficiency by as much as a factor of four. Meanwhile, surface passivation via Ar/O_2 plasma cleaning did not result in enhancements to the crystal, with XPS confirming the formation of metallic Pb^0 defects that act as nonradiative recombination centers. Although plasma cleaning has been reported to be effective, the results here indicate the need for significant control over the process in order to avoid such degradations. Finally, the implementation of an electrode design that incorporated a tin oxide (SnO_2) interfacial layer at the anode increased the success rate of MHP device fabrication. Based on the known ionic conductivity of halides in MHP and the corrosion resistance of metal oxides,

it was concluded that the SnO_2 layer acted as a barrier against electrochemical reactions between halides and the metallic contact.

Determining Charge Transport Properties

The fabricated MHP sensors had $\mu_h\tau_h$ values on the order of 10^{-4} and 10^{-2} cm^2 V^{-1} as determined via CCE curve fitting with alpha particle irradiation and X-ray induced photocurrents respectively, which are both in agreement with values reported in literature. Due to ballistic deficit from both the finite shaping time of the amplifier and the fall time of the preamplifier, it was not always possible to fit CCE curves to the Hecht and Many equations. However, the ***1-e*** behavior of the CCE curve could be restored following a series of partial deconvolutions of the preamplifier traces that reconstructed the ballistic signal and restored the lost signal amplitude, which allowed for determination of charge transport properties. Mobility could be calculated via single trace analysis if the carriers had not yet reached their saturation velocity under the electric field applied. However, a more accurate method of determining mobility was demonstrated by plotting carrier velocity against the applied electric field and finding the slope of the linear portion of the curve prior to reaching the drift saturation velocity. A hole mobility in $MAPbBr_{2.85}Cl_{0.15}$ was determined with this method to be 4.25 cm^2 V^{-1} s^{-1}, which was on par with mobilities calculated with space charge limited current techniques or Hall measurements. Moreover, the SnO_2 layer also acted as an electron extraction layer in producing an alpha-particle induced electron response in MAPB. The $\mu_e\tau_e$ was estimated to be 4.59×10^{-4} cm^2 V^{-1}, with an S/μ_e value of 57.82 V cm^{-1}, which at the time, represented the first reports of electron charge transport properties in MAPB determined via single quanta sensing. An electron mobility of 14.51 cm^2 V^{-1} s^{-1} was determined from single trace analysis, which is in agreement with similar values derived via ToF techniques. Finally, the lifetimes for holes and electrons were on the order of 20-30 μs as determined through CCE curve fitting and trace analysis.

Radiation Sensing

A radiograph of a brass key was produced via soft X-ray irradiation with polycrystalline MAPB, which also showed stable net current output and sensitivity under irradiation with the

highest reported hole transport properties to date determined with photoconductive methods. However, a high dose rate of 0.368 Gy s^{-1} was required, likely due to a combination of surface inhomogeneity, hysteresis, and radiation damage.

Meanwhile, a resolution of 15% at 59.5 keV was achieved in $MAPbBr_{2.85}Cl_{0.15}$ using a non-spectroscopic ^{241}Am source, which was on par with the best reported resolutions at that energy in MHPs. However, spectroscopic gamma ray sensing was not possible with higher energy gamma rays from ^{133}Ba, ^{137}Cs, and ^{60}Co due to insufficient charge transport properties and variable ballistic deficit. A bi-parametric program was developed in Python to improve the gamma ray sensing performance in MHPs during post-processing. Prior to the implementation of correction factors, the program smoothed traces via moving average, determined the start of the rise based on the slope between two points on the trace, and filtered out traces unsuitable for processing by setting a threshold for the R^2 value between an artificial and real trace. After the pole of the preamplifier was removed through deconvolution, the charge loss correction factor (CLCF) was implemented to account for charge losses during hole transport to the collecting electrode, which was derived from the single polarity Hecht equation. Following the CLCF, the depth correction factor (DCF) compensates for the variation in induced charge due to the depth dependence of gamma ray interactions. The combination of deconvolution, DCF, and CLCF resolved a spectrum that resembled a Compton continuum without the characteristic photopeak from ^{137}Cs, indicating that the effectiveness of the program also depends on the speed of the pulse processing electronics, stability of the detector, and detection efficiency.

Finally, thermal neutron sensing was achieved by incorporating lithium in the form of natural LiCl into the MAPB crystal structure at a 2.5% doping concentration as verified by ICP-OES, EDX, and Raman spectroscopy. Despite containing less than 150 ppm of ^{6}Li, the LiMAPB was shown to be sensitive to thermal neutrons through a series of exposures to a 2 Ci $^{239}Pu/Be$ source, as well as the thermal neutron beam at the Ohio State University Research Reactor (OSURR). Moreover, no increase in dark current in the LiMAPB detector was observed after the OSURR irradiation, which demonstrates its remarkable stability for thermal neutron sensing.

Degradations and Improvements to Detector Performance

After receiving a total dose of 6.65 kGy delivered via X-ray irradiation over 5 minutes, a $MAPbBr_{2.85}Cl_{0.15}$ single crystal showed a nearly 17-fold reduction in apparent charge collection efficiency, while hole mobility decreased by over half. Although this demonstrated that radiation damage is a factor to consider during operation, the X-ray sensitivity of MAPB was also shown to be relatively stable over time with dose rates that that more closely resemble those used in imaging operations.

Finally, improvements to detector performance via annealing and low temperature operation were evaluated. Annealing of the irradiated $MAPbBr_{2.85}Cl_{0.15}$ single crystal for 24 hours at 125°C in an N_2 environment within an oven led to improvements in bulk resistivity, a nearly 15% increase in apparent mobility, and a 7-fold increase in apparent charge collection efficiency, which was potentially due to a reduction in defect states that decreased scattering and mitigated polarization from the accumulation of space charge as a result of radiation induced traps near the collecting electrode. On the other hand, annealing MAPB single crystals for 2 hours at 125°C in an argon environment within a tube furnace resulted in the formation of inclusions and $PbBr_2$ particulates on the crystal surfaces. Increased dark current, decreased signal pulse amplitudes, and reduced apparent charge collection efficiency were observed after annealing due to the degradation of surface quality. At the same time, trap controlled conductivity was significantly reduced along with the rise times of the fast component of the signals. These results suggest that annealing is capable of reducing defects within the crystal bulk, and greater control over the annealing process is required to prevent losses in charge collection efficiency due to surface degradations.

For low temperature operation, the LiMAPB detector, which had been shown to have high bulk quality through birefringence imaging, showed nearly a 30% increase in hole mobility and enhanced charge collection efficiency at 0°C compared to 20°C, which was attributed to reduced phonon scattering at lower temperatures. However, a $MAPbBr_{2.85}Cl_{0.15}$ with poor internal quality showed some degree of TCC at 20°C, 0°C, and -20°C, with the TCC becoming more prominent at 0°C before disappearing at -20°C. This was due to two simultaneous effects. First, the slow

component of the signal rise becomes more pronounced at lower temperatures as the detrapping rate decreases. Second, it had been reported in MAPB that detrapping activity essentially “freezes” below 250K, which led to the disappearance of TCC at -20°C. At the same time, the fast component rise time continued to systematically decrease at low temperatures due to reduced phonon scattering. This indicates that the competition between these three effects is complex, and the effectiveness of low temperature operation is strongly influenced by crystal quality and trap concentration.

Chapter 5: Outlook

Solution grown metal halide perovskites carry significant potential to be developed and deployed as a versatile and low-cost per volume radiation sensor for a variety of nuclear security and X-ray imaging applications. Their ease of fabrication, large resistivity, high detection efficiency, radiation tolerance, and ability to modify its stoichiometry to achieve desired capabilities such as thermal neutron sensing are attractive qualities to the detector development community. However, there still remain significant challenges to overcome in its development, and this dissertation has presented a number of notable achievements in identifying and addressing those obstacles. As a soft material, the development of surface passivation methods such as DMF polishing remains a critical step in limiting charge losses from surface recombination and ensuring that judiciously selected electrode materials form a stable interface. Maintaining device stability is also a significant challenge, as the effects of ionic conductivity can limit the sensitivity of X-ray imaging devices or produce spectral inconsistencies in an RIID. Perhaps the most important issue to address, however, is the charge carrier properties, either by improving the hole transport properties to reduce the level of variable ballistic deficit or by improving the electron transport properties to mitigate the need for complex single carrier charge sensing techniques. Much of this effort involves optimizing the growth process to improve internal crystal quality, as it was demonstrated that the effectiveness of low temperature operation to improve carrier mobility is strongly affected by defect concentration. The use of birefringence to screen for crystal quality is a significant step in the selection of high-quality crystals for fabrication, and the implementation of the SnO_2 to extract electron signals highlights the need for effective interfacial layers to both protect metallic contacts and extract charge. Despite the challenges identified, however, the notable radiation sensing achievements presented in this dissertation such as the high resolution observed for low energy gamma rays, X-ray radiograph produced with a low-quality sensor, development of a bi-parametric program that avoids significant efficiency losses, and thermal neutron sensing with lithium dopants show promise for the continued development of MHP detectors to meet the need for high performing and low cost detection systems for imaging and nuclear security applications.

Bibliography

[1] R. T. Kouzes *et al.*, "Naturally Occurring Radioactive Materials and Medical Isotopes at Border Crossings," in *2003 IEEE Nuclear Science Symposium. Conference Record (IEEE Cat. No.03CH37515)*, 19-25 Oct. 2003 2003, vol. 2, pp. 1448-1452 Vol.2, doi: 10.1109/NSSMIC.2003.1351967.

[2] R. C. Runkle, L. E. Smith, and A. J. Peurrung, "The Photon Haystack and Emerging Radiation Detection Technology," *Journal of Applied Physics*, vol. 106, no. 4, 2009, doi: 10.1063/1.3207769.

[3] P. M. Johns and J. C. Nino, "Room Temperature Semiconductor Detectors for Nuclear Security," *Journal of Applied Physics*, vol. 126, no. 4, 2019, doi: 10.1063/1.5091805.

[4] M. Sanjoy, M. Richard, G. Paul, and K. Craig, "Review of Current Neutron Detection Systems for Emergency Response," vol. 9213, pp. 140 -- 149, 2014, doi: 10.1117/12.2058165.

[5] "Handheld Radionuclide Identification Devices (RIDs) Market Survey Report," in "System Assessment and Validation for Emergency Responders (SAVER)," National Urban Security Technology Laboratory, 2015.

[6] "American National Standard for Determination of the Imaging Performance of X-Ray and Gamma-Ray Systems for Cargo and Vehicle Security Screening," *ANSI N42.46-2008*, pp. 1-35, 2008, doi: 10.1109/ANSI.2008.4606807.

[7] J. Bendahan, "Review of Active Interrogation Techniques," *Nucl. Instrum. Methods Phys. Res. A: Accel. Spectrom. Detect. Assoc. Equip.*, vol. 954, 2020, doi: 10.1016/j.nima.2018.08.079.

[8] J. Glodo *et al.*, "New Developments in Scintillators for Security Applications," *Phys. Procedia*, vol. 90, pp. 285-290, 2017, doi: 10.1016/j.phpro.2017.09.012.

[9] T. J. Hajagos, C. Liu, N. J. Cherepy, and Q. Pei, "High-Z Sensitized Plastic Scintillators: A Review," *Adv Mater*, vol. 30, no. 27, p. e1706956, Jul 2018, doi: 10.1002/adma.201706956.

[10] M. J. Murphy *et al.*, "The Management of Imaging Dose During Image-Guided Radiotherapy: Report of the AAPM Task Group 75," *Med. Phys.*, vol. 34, no. 10, pp. 4041-4063, 2007/10/01 2007, doi: 10.1118/1.2775667.

[11] D. L. Miller, "Interventional Fluoroscopy: Reducing Radiation Risks for Patients and Staff," *Journal of Vascular Interventional Radiology*, vol. 20, no. 7, S274, 2009, doi: 10.1016/j.jvir.2009.04.057.

[12] P. N. McDermott and C. G. Orton, *The Physics and Technology of Radiation Therapy*. Madison, WI: Medical Physics Publishing, 2018.

[13] Y. C. Kim *et al.*, "Printable Organometallic Perovskite Enables Large-Area, Low-Dose X-ray Imaging," *Nature*, vol. 550, no. 7674, pp. 87-91, Oct 4 2017, doi: 10.1038/nature24032.

[14] C. Ronda, H. Wieczorek, V. Khanin, and P. Rodnyi, "Review—Scintillators for Medical Imaging: A Tutorial Overview," *ECS J. Solid State Sci. Technol.*, vol. 5, no. 1, pp. R3121-R3125, 2015, doi: 10.1149/2.0131601jss.

[15] I. G. Valais *et al.*, "Luminescence Emission Properties of (Lu, Y)(2)SiO5:Ce (LYSO:Ce) and (Lu,Y)AlO3:Ce (LuYAP:Ce) Single Crystal Scintillators Under Medical Imaging Conditions," *IEEE Trans. Nucl. Sci.*, vol. 55, no. 2, pp. 785-789, 2008, doi: 10.1109/tns.2008.918737.

[16] M. Daum *et al.*, "Self-Healing Cs3Bi2Br3I6 Perovskite Wafers for X-Ray Detection," *Adv. Funct. Mater.*, vol. 31, no. 47, 2021, doi: 10.1002/adfm.202102713.

[17] H. Wei and J. Huang, "Halide Lead Perovskites for Ionizing Radiation Detection," *Nat Commun*, vol. 10, no. 1, p. 1066, Mar 6 2019, doi: 10.1038/s41467-019-08981-w.

[18] B. D. Milbrath, A. J. Peurrung, M. Bliss, and W. J. Weber, "Radiation Detector Materials: An Overview," *J. Mater. Res.*, vol. 23, no. 10, pp. 2561-2581, 2011, doi: 10.1557/jmr.2008.0319.

[19] A. Owens, *Compound Semiconductor Radiation Detectors* (Series in Sensors). Boca Raton, FL: Taylor & Francis, 2012.

[20] A. Owens and A. Peacock, "Compound Semiconductor Radiation Detectors," *Nucl. Instrum. Methods Phys. Res. A: Accel. Spectrom. Detect. Assoc. Equip.*, vol. 531, no. 1-2, pp. 18-37, 2004, doi: 10.1016/j.nima.2004.05.071.

[21] S. Ramo, "Currents Induced by Electron Motion," *Proc. IRE,* vol. 27, no. 9, pp. 584-585, 1939, doi: 10.1109/JRPROC.1939.228757.

[22] Z. He, "Review of the Shockley-Ramo Theorem and its Application in Semiconductor Gamma-ray Detectors," *Nucl. Instrum. Methods Phys. Res. A: Accel. Spectrom. Detect. Assoc. Equip.,* vol. 463, no. 1-2, pp. 250-267, 2001.

[23] D. S. McGregor, Z. He, H. A. Seifert, D. K. Wehe, and R. A. Rojeski, "Single Charge Carrier Type Sensing With a Parallel Strip Pseudo-Frisch-Grid CdZnTe Semiconductor Radiation Detector," *Appl. Phys. Lett.,* vol. 72, no. 7, pp. 792-794, 1998, doi: 10.1063/1.120895.

[24] D. S. Bale *et al.,* "Design of High-Performance CdZnTe Quasi-Hemispherical Gamma-Ray CAPture Plus Detectors," presented at the Hard X-Ray and Gamma-Ray Detector Physics and Penetrating Radiation Systems VIII, 2006.

[25] L. A. Franks *et al.,* "Fabrication of High-Performance CdZnTe Quasi-Hemispherical Gamma-Ray CAPture Plus Detectors," presented at the Hard X-Ray and Gamma-Ray Detector Physics and Penetrating Radiation Systems VIII, 2006.

[26] H. Malm, C. Canali, J. Mayer, M. A. Nicolet, K. Zanio, and W. Akutagawa, "Gamma-Ray Spectroscopy with Single-Carrier Collection in High-Resistivity Semiconductors," *Appl. Phys. Lett.,* vol. 26, pp. 344-346, 04/01 1975, doi: 10.1063/1.88158.

[27] J. C. Kim *et al.,* "Charge Sharing in Common-Grid Pixelated CdZnTe Detectors," *Nucl. Instrum. Methods Phys. Res. A: Accel. Spectrom. Detect. Assoc. Equip.,* vol. 654, no. 1, pp. 233-243, 2011, doi: 10.1016/j.nima.2011.06.038.

[28] B. G. L. R. A. Sareen, *Semiconductor X-Ray Detectors* (Series in Sensors). Boca Raton, FL: CRC Press, 2013.

[29] H. H. Barrett, J. D. Eskin, and H. B. Barber, "Charge Transport in Arrays of Semiconductor Gamma-Ray Detectors," *Phys. Rev. Lett.,* vol. 75, no. 1, pp. 156-159, 07/03/ 1995, doi: 10.1103/PhysRevLett.75.156.

[30] Y. Ma, S. Xiao, G. Yang, and L. Zhang, "Design and Study of a Coplanar Grid Array CdZnTe Detector for Improved Spatial Resolution," *Appl. Radiat. Isot.,* vol. 94, pp. 314-318, 2014/12/01/ 2014, doi: 10.1016/j.apradiso.2014.09.003.

[31] P. N. Luke, "Single-Polarity Charge Sensing in Ionization Detectors Using Coplanar Electrodes," *Appl. Phys. Lett.*, vol. 65, no. 22, pp. 2884-2886, 1994, doi: 10.1063/1.112523.

[32] V. T. Jordanov, J. A. Pantazis, and A. C. Huber, "Compact Circuit for Pulse Rise-Time Discrimination," *Nucl. Instrum. Methods Phys. Res. A: Accel. Spectrom. Detect. Assoc. Equip.*, vol. 380, no. 1, pp. 353-357, 1996/10/01/ 1996, doi: 10.1016/S0168-9002(96)00357-9.

[33] R. Redus, M. Squillante, and J. Lund, "Electronics for High Resolution Spectroscopy With Compound Semiconductors," *Nucl. Instrum. Methods Phys. Res. A: Accel. Spectrom. Detect. Assoc. Equip.*, vol. 380, no. 1, pp. 312-317, 1996/10/01/ 1996, doi: 10.1016/S0168-9002(96)00307-5.

[34] T. Tada *et al.*, "Digital Pulse Processing and Electronic Noise Analysis for Improving Energy Resolutions in Planar TlBr Detectors," *Nucl. Instrum. Methods Phys. Res. A: Accel. Spectrom. Detect. Assoc. Equip.*, vol. 638, no. 1, pp. 92-95, 2011, doi: 10.1016/j.nima.2011.02.070.

[35] M. Richter and P. Siffert, "High Resolution Gamma Ray Spectroscopy with CdTe Detector Systems," *Nucl. Instrum. Methods Phys. Res. A: Accel. Spectrom. Detect. Assoc. Equip.*, vol. 322, no. 3, pp. 529-537, 1992/11/15/ 1992, doi: 10.1016/0168-9002(92)91227-Z.

[36] Z. Zhang and G. Yang, "Recent Advancements in Using Perovskite Single Crystals for Gamma-Ray Detection," *J. Mater. Sci.: Mater. Electron.*, 2020, doi: 10.1007/s10854-020-03519-z.

[37] L. Gao and Q. Yan, "Recent Advances in Lead Halide Perovskites for Radiation Detectors," *Sol. RRL*, 2019, doi: 10.1002/solr.201900210.

[38] P. P. Boix, K. Nonomura, N. Mathews, and S. G. Mhaisalkar, "Current Progress and Future Perspectives for Organic/Inorganic Perovskite Solar Cells," *Mater. Today*, vol. 17, no. 1, pp. 16-23, 2014, doi: 10.1016/j.mattod.2013.12.002.

[39] Y. He *et al.*, "CsPbBr3 Perovskite Detectors with 1.4% Energy Resolution for High-Energy γ-Rays," *Nat. Photonics*, vol. 15, no. 1, pp. 36-42, 2020, doi: 10.1038/s41566-020-00727-1.

[40] H. J. Snaith, "Perovskites: The Emergence of a New Era for Low-Cost, High-Efficiency Solar Cells," *The Journal of Physical Chemistry Letters,* vol. 4, no. 21, pp. 3623-3630, 2013, doi: 10.1021/jz4020162.

[41] J. T. Tisdale, "Development of Organometallic Hybrid Perovskite Single Crystals Towards Radiation Sensing and Optoelectronic Applications," PhD, Materials Science and Engineering, University of Tennessee, University of Tennessee, 2018. [Online]. Available: https://trace.tennessee.edu/utk_graddiss/5250

[42] H. Wei *et al.*, "Dopant Compensation in Alloyed CH3NH3PbBr3-xClx Perovskite Single Crystals for Gamma-ray Spectroscopy," *Nat Mater,* vol. 16, no. 8, pp. 826-833, Aug 2017, doi: 10.1038/nmat4927.

[43] S. Yakunin *et al.*, "Detection of Gamma Photons Using Solution-Grown Single Crystals of Hybrid Lead Halide Perovskites," *Nat. Photonics,* vol. 10, no. 9, pp. 585-589, 2016, doi: 10.1038/nphoton.2016.139.

[44] C. C. Stoumpos *et al.*, "Crystal Growth of the Perovskite Semiconductor CsPbBr3: A New Material for High-Energy Radiation Detection," *Cryst. Growth Des.,* vol. 13, no. 7, pp. 2722-2727, 2013/07/03 2013, doi: 10.1021/cg400645t.

[45] E. Lukosi *et al.*, "Methylammonium Lead Tribromide Semiconductors: Ionizing Radiation Detection and Electronic Properties," *Nucl. Instrum. Methods Phys. Res. A: Accel. Spectrom. Detect. Assoc. Equip.,* vol. 927, pp. 401-406, 2019, doi: 10.1016/j.nima.2019.02.059.

[46] J. T. Tisdale *et al.*, "Dynamic Impact of Electrode Materials on Interface of Single-Crystalline Methylammonium Lead Bromide Perovskite," *Adv. Mater. Interfaces,* vol. 5, no. 18, 2018, doi: 10.1002/admi.201800476.

[47] O. Nazarenko, S. Yakunin, V. Morad, I. Cherniukh, and M. V. Kovalenko, "Single Crystals of Caesium Formamidinium Lead Halide Perovskites: Solution Growth and Gamma Dosimetry," *NPG Asia Mater.,* vol. 9, no. 4, pp. e373-e373, 2017, doi: 10.1038/am.2017.45.

[48] K. Hecht, "Zum Mechanismus des lichtelektrischen Primärstromes in isolierenden Kristallen," *Z. Phys.,* vol. 77, no. 3, pp. 235-245, 1932/03/01 1932, doi: 10.1007/BF01338917.

[49] S. Shrestha *et al.*, "High-Performance Direct Conversion X-ray Detectors Based on Sintered Hybrid Lead Triiodide Perovskite Wafers," *Nat. Photonics,* vol. 11, no. 7, pp. 436-440, 2017, doi: 10.1038/nphoton.2017.94.

[50] H. Wei *et al.*, "Sensitive X-Ray Detectors Made of Methylammonium Lead Tribromide Perovskite Single Crystals," *Nat. Photonics,* vol. 10, no. 5, pp. 333-339, 2016, doi: 10.1038/nphoton.2016.41.

[51] X. Geng *et al.*, "High-Quality Single Crystal Perovskite for Highly Sensitive X-Ray Detector," *IEEE Electron Device Lett.,* vol. 41, no. 2, pp. 256-259, 2020, doi: 10.1109/led.2019.2960384.

[52] W. Li *et al.*, "Fine-Control-Valve of Halide Perovskite Single Crystal Quality for High Performance X-ray Detection," *Sci. Bull.,* vol. 66, no. 21, pp. 2199-2206, 2021, doi: 10.1016/j.scib.2021.06.016.

[53] W. Wei *et al.*, "Monolithic Integration of Hybrid Perovskite Single Crystals with Heterogenous Substrate for Highly Sensitive X-Ray Imaging," *Nat. Photonics,* vol. 11, no. 5, pp. 315-321, 2017, doi: 10.1038/nphoton.2017.43.

[54] Y. He *et al.*, "High Spectral Resolution of Gamma-Rays at Room Temperature by Perovskite CsPbBr3 Single Crystals," *Nat Commun,* vol. 9, no. 1, p. 1609, Apr 23 2018, doi: 10.1038/s41467-018-04073-3.

[55] Y. He *et al.*, "Demonstration of Energy-Resolved gamma-Ray Detection at Room Temperature by the CsPbCl3 Perovskite Semiconductor," *J Am Chem Soc,* vol. 143, no. 4, pp. 2068-2077, Feb 3 2021, doi: 10.1021/jacs.0c12254.

[56] Y. He *et al.*, "Resolving the Energy of γ-Ray Photons with MAPbI3 Single Crystals," *ACS Photonics,* vol. 5, no. 10, pp. 4132-4138, 2018, doi: 10.1021/acsphotonics.8b00873.

[57] Q. Xu *et al.*, "Detection of Charged Particles With a Methylammonium Lead Tribromide Perovskite Single Crystal," *Nucl. Instrum. Methods Phys. Res. A: Accel. Spectrom. Detect. Assoc. Equip.,* vol. 848, pp. 106-108, 2017, doi: 10.1016/j.nima.2016.12.062.

[58] R. Tan, B. Dryzhakov, J. Charest, B. Hu, M. Ahmadi, and E. Lukosi, "Improved Radiation Sensing with Methylammonium Lead Tribromide Perovskite Semiconductors," *Nucl. Instrum. Methods Phys. Res. A: Accel. Spectrom. Detect. Assoc. Equip.,* vol. 986, 2021, doi: 10.1016/j.nima.2020.164710.

[59] X. Liu, H. Zhang, B. Zhang, J. Dong, W. Jie, and Y. Xu, "Charge Transport Behavior in Solution-Grown Methylammonium Lead Tribromide Perovskite Single Crystal Using α Particles," *The Journal of Physical Chemistry C,* vol. 122, no. 26, pp. 14355-14361, 2018, doi: 10.1021/acs.jpcc.8b03512.

[60] M. A. Lampert and P. Mark, *Current Injection in Solids*. New York: Academic Press, 1970.

[61] L. Pan, Y. Feng, P. Kandlakunta, J. Huang, and L. R. Cao, "Performance of Perovskite CsPbBr3 Single Crystal Detector for Gamma-Ray Detection," *IEEE Trans. Nucl. Sci.,* vol. 67, no. 2, pp. 443-449, 2020, doi: 10.1109/tns.2020.2964306.

[62] Q. Xu *et al.*, "CsPbBr3 Single Crystal X-ray Detector with Schottky Barrier for X-ray Imaging Application," *ACS Appl. Electron. Mater.,* vol. 2, no. 4, pp. 879-884, 2020/04/28 2020, doi: 10.1021/acsaelm.9b00832.

[63] X. Wang *et al.*, "PIN Diodes Array Made of Perovskite Single Crystal for X-Ray Imaging," *physica status solidi (RRL) – Rapid Research Letters,* vol. 12, no. 10, p. 1800380, 2018/10/01 2018, doi: 10.1002/pssr.201800380.

[64] Q. Xu *et al.*, "High-Performance Surface Barrier X-ray Detector Based on Methylammonium Lead Tribromide Single Crystals," *ACS Appl. Mater. Interfaces,* vol. 11, no. 10, pp. 9679-9684, 2019/03/13 2019, doi: 10.1021/acsami.8b21605.

[65] K. M. McCall *et al.*, "Fast Neutron Imaging with Semiconductor Nanocrystal Scintillators," *ACS Nano,* vol. 14, no. 11, pp. 14686-14697, Nov 24 2020, doi: 10.1021/acsnano.0c06381.

[66] J. Zheng *et al.*, "Hydrogen-Rich 2D Halide Perovskite Scintillators for Fast Neutron Radiography," *J Am Chem Soc,* vol. 143, no. 50, pp. 21302-21311, Dec 22 2021, doi: 10.1021/jacs.1c08923.

[67] F. Montanarella *et al.*, "Highly Concentrated, Zwitterionic Ligand-Capped Mn(2+):CsPb(Br x Cl1-x)3 Nanocrystals as Bright Scintillators for Fast Neutron Imaging," *ACS Energy Lett,* vol. 6, no. 12, pp. 4365-4373, Dec 10 2021, doi: 10.1021/acsenergylett.1c01923.

[68] P. Andricevic *et al.*, "Hybrid Halide Perovskite Neutron Detectors," *Sci Rep,* vol. 11, no. 1, p. 17159, Aug 30 2021, doi: 10.1038/s41598-021-95586-3.

[69] A. Xie *et al.*, "Lithium-Doped Two-Dimensional Perovskite Scintillator for Wide-Range Radiation Detection," *Commun. Mater.*, vol. 1, no. 1, 2020, doi: 10.1038/s43246-020-0038-x.

[70] F. Maddalena *et al.*, "Effect of Commensurate Lithium Doping on the Scintillation of Two-Dimensional Perovskite Crystals," *Journal of Materials Chemistry C,* vol. 9, no. 7, pp. 2504-2512, 2021, doi: 10.1039/d0tc05647b.

[71] L. Fernandez-Izquierdo *et al.*, "Cesium Lead Bromide (CsPbBr3) Thin-Film-Based Solid-State Neutron Detector Developed by a Solution-Free Sublimation Process," *Advanced Materials Technologies,* vol. 5, no. 12, p. 2000534, 2020/12/01 2020, doi: 10.1002/admt.202000534.

[72] J. A. Caraveo-Frescas, M. G. Reyes-Banda, L. Fernandez-Izquierdo, and M. A. Quevedo-Lopez, "3D Microstructured Inorganic Perovskite Materials for Thermal Neutron Detection," *Advanced Materials Technologies*, vol. n/a, no. n/a, p. 2100956, 2022, Art no. 2100956, doi: 10.1002/admt.202100956.

[73] L. El Bouanani *et al.*, "Solid-State Neutron Detection Based on Methylammonium Lead Bromide Perovskite Single Crystals," *ACS Appl Mater Interfaces,* vol. 13, no. 24, pp. 28049-28056, Jun 23 2021, doi: 10.1021/acsami.1c03580.

[74] T. R. Ochs, S. L. Bellinger, R. G. Fronk, L. C. Henson, R. M. Hutchins, and D. S. McGregor, "Improved Manufacturing and Performance of the Dual-sided Microstructured Semiconductor Neutron Detector (DS-MSND)," *Nucl. Instrum. Methods Phys. Res. A: Accel. Spectrom. Detect. Assoc. Equip.,* vol. 954, 2020, doi: 10.1016/j.nima.2018.12.011.

[75] D. S. McGregor, M. D. Hammig, Y. H. Yang, H. K. Gersch, and R. T. Klann, "Design Considerations for Thin Film Coated Semiconductor Thermal Neutron Detectors—I: Basics Regarding Alpha Particle Emitting Neutron Reactive Films," *Nucl. Instrum. Methods Phys. Res. A: Accel. Spectrom. Detect. Assoc. Equip.,* vol. 500, no. 1, pp. 272-308, 2003/03/11/ 2003, doi: 10.1016/S0168-9002(02)02078-8.

[76] P. Andričević *et al.,* "Three-Dimensionally Enlarged Photoelectrodes by a Protogenetic Inclusion of Vertically Aligned Carbon Nanotubes into CH3NH3PbBr3 Single Crystals," *The Journal of Physical Chemistry C,* vol. 121, no. 25, pp. 13549-13556, 2017, doi: 10.1021/acs.jpcc.7b03421.

[77] D. S. Lee *et al.,* "Passivation of Grain Boundaries by Phenethylammonium in Formamidinium-Methylammonium Lead Halide Perovskite Solar Cells," *ACS Energy Lett.,* vol. 3, no. 3, pp. 647-654, 2018, doi: 10.1021/acsenergylett.8b00121.

[78] F. Cai *et al.,* "Ionic Additive Engineering Toward High-Efficiency Perovskite Solar Cells with Reduced Grain Boundaries and Trap Density," *Adv. Funct. Mater.,* vol. 28, no. 34, 2018, doi: 10.1002/adfm.201801985.

[79] M. Sytnyk, S. Deumel, S. F. Tedde, G. J. Matt, and W. Heiss, "A Perspective on the Bright Future of Metal Halide Perovskites for X-ray Detection," *Appl. Phys. Lett.,* vol. 115, no. 19, 2019, doi: 10.1063/1.5125999.

[80] H.-H. Fang *et al.,* "Ultrahigh Sensitivity of Methylammonium Lead Tribromide Perovskite Single Crystals to Environmental Gases," *Sci. Adv.,* vol. 2, no. 7, p. e1600534, 2016, doi: 10.1126/sciadv.1600534.

[81] Y. Cui, G. W. Wright, X. Ma, K. Chattopadhyay, R. B. James, and A. Burger, "DC Photoconductivity Study of Semi-insulating Cd(1–x)ZnxTe Crystals," *J. Electron. Mater.,* vol. 30, no. 6, 2001.

[82] A. Many, "High-Field Effects in Photoconducting Cadmium Sulphide," *J. Phys. Chem. Solids,* vol. 26, no. 3, pp. 575-578, 1965/03/01/ 1965, doi: 10.1016/0022-3697(65)90133-2.

[83] N. Aristidou *et al.*, "Fast Oxygen Diffusion and Iodide Defects Mediate Oxygen-Induced Degradation of Perovskite Solar Cells," *Nat Commun,* vol. 8, p. 15218, May 11 2017, doi: 10.1038/ncomms15218.

[84] M. Wang, "Exploring Stability of Formamidinium Lead Trihalide for Solar Cell Application," *Sci. Bull.*, vol. 62, no. 4, pp. 249-255, 2017, doi: 10.1016/j.scib.2017.01.025.

[85] J. Pospisil, O. Zmeskal, J. Krajcovic, M. Weiter, and A. Kovalenko, "Light-Induced Non-Arrhenian Conductivity of the Single Crystal Methylammonium Lead Bromide Perovskites," *Solid State Commun.,* vol. 307, 2020, doi: 10.1016/j.ssc.2019.113777.

[86] J. Pospisil, O. Zmeskal, S. Nespurek, J. Krajcovic, M. Weiter, and A. Kovalenko, "Density of Bulk Trap States of Hybrid Lead Halide Perovskite Single Crystals: Temperature Modulated Space-Charge-Limited-Currents," *Sci Rep,* vol. 9, no. 1, p. 3332, Mar 4 2019, doi: 10.1038/s41598-019-40139-y.

[87] S. Yang *et al.*, "Stabilizing Halide Perovskite Surfaces for Solar Cell Operation with Wide-Bandgap Lead Oxysalts," vol. 365, no. 6452, pp. 473-478, 2019, doi: 10.1126/science.aax3294 %J Science.

[88] S. G. Joglekar, M. D. Hammig, and L. J. Guo, "High-Energy Photon Spectroscopy Using All Solution-Processed Heterojunctioned Surface-Modified Perovskite Single Crystals," *ACS Appl Mater Interfaces,* vol. 11, no. 36, pp. 33399-33408, Sep 11 2019, doi: 10.1021/acsami.9b09381.

[89] Z. Fan *et al.*, "Layer-by-Layer Degradation of Methylammonium Lead Tri-iodide Perovskite Microplates," *Joule,* vol. 1, no. 3, pp. 548-562, 2017, doi: 10.1016/j.joule.2017.08.005.

[90] W. Yu *et al.*, "Single Crystal Hybrid Perovskite Field-Effect Transistors," *Nat Commun,* vol. 9, no. 1, p. 5354, Dec 17 2018, doi: 10.1038/s41467-018-07706-9.

[91] R. Heiderhoff *et al.*, "Thermal Conductivity of Methylammonium Lead Halide Perovskite Single Crystals and Thin Films: A Comparative Study," *The Journal of Physical Chemistry C,* vol. 121, no. 51, pp. 28306-28311, 2017, doi: 10.1021/acs.jpcc.7b11495.

[92] W. Zhang *et al.*, "Ultrasmooth Organic-Inorganic Perovskite Thin-Film Formation and Crystallization for Efficient Planar Heterojunction Solar Cells," *Nat Commun,* vol. 6, p. 6142, Jan 30 2015, doi: 10.1038/ncomms7142.

[93] S. Brittman and E. C. Garnett, "Measuring n and k at the Microscale in Single Crystals of CH3NH3PbBr3 Perovskite," *The Journal of Physical Chemistry C,* vol. 120, no. 1, pp. 616-620, 2015, doi: 10.1021/acs.jpcc.5b11075.

[94] R. A. Kerner, L. Zhao, Z. Xiao, and B. P. Rand, "Ultrasmooth Metal Halide Perovskite Thin Films via Sol–Gel Processing," *Journal of Materials Chemistry A,* vol. 4, no. 21, pp. 8308-8315, 2016, doi: 10.1039/c6ta03092k.

[95] B. Wenger, P. K. Nayak, X. Wen, S. V. Kesava, N. K. Noel, and H. J. Snaith, "Consolidation of the Optoelectronic Properties of CH3NH3PbBr3 Perovskite Single Crystals," *Nat Commun,* vol. 8, no. 1, p. 590, Sep 19 2017, doi: 10.1038/s41467-017-00567-8.

[96] Y. Song *et al.*, "Atomistic Surface Passivation of CH3NH3PbI3 Perovskite Single Crystals for Highly Sensitive Coplanar-Structure X-Ray Detectors," *Research (Wash D C),* vol. 2020, p. 5958243, 2020, doi: 10.34133/2020/5958243.

[97] T. Kim *et al.*, "Confined Growth of High-quality Single-Crystal MAPbBr3 by Inverse Temperature Crystallization for Photovoltaic Applications," *Electron. Mater. Lett.,* vol. 17, no. 4, pp. 347-354, 2021/07/01 2021, doi: 10.1007/s13391-021-00288-7.

[98] N. Rybin *et al.*, "Effects of Chlorine Mixing on Optoelectronics, Ion Migration, and Gamma-Ray Detection in Bromide Perovskites," *Chem. Mater.,* 2020, doi: 10.1021/acs.chemmater.9b04244.

[99] Z. Fang, H. He, L. Gan, J. Li, and Z. Ye, "Understanding the Role of Lithium Doping in Reducing Nonradiative Loss in Lead Halide Perovskites," *Adv Sci (Weinh),* vol. 5, no. 12, p. 1800736, Dec 2018, doi: 10.1002/advs.201800736.

[100] S. Jiang *et al.*, "Balance Lead in Solution-Processed CH3NH3PbBrxCl(3−x) Single Crystals for High Performance X-ray Detection," *Mater. Lett.,* vol. 236, pp. 26-29, 2019, doi: 10.1016/j.matlet.2018.10.055.

[101] Y. Fang, Q. Dong, Y. Shao, Y. Yuan, and J. Huang, "Highly Narrowband Perovskite Single-Crystal Photodetectors Enabled by Surface-Charge Recombination," *Nat. Photonics,* vol. 9, no. 10, pp. 679-686, 2015, doi: 10.1038/nphoton.2015.156.

[102] H. S. Gill *et al.*, "Flexible Perovskite Based X-ray Detectors for Dose Monitoring in Medical Imaging Applications," *Physics in Medicine*, vol. 5, pp. 20-23, 2018/06/01/ 2018, doi: 10.1016/j.phmed.2018.04.001.

[103] C. H. Lin *et al.*, "Electrode Engineering in Halide Perovskite Electronics: Plenty of Room at the Interfaces," *Adv Mater,* vol. 34, no. 18, p. e2108616, May 2022, doi: 10.1002/adma.202108616.

[104] W. Chu, W. A. Saidi, J. Zhao, and O. V. Prezhdo, "Soft Lattice and Defect Covalency Rationalize Tolerance of β-CsPbI3 Perovskite Solar Cells to Native Defects," *Angew. Chem. Int. Ed.,* vol. 59, no. 16, pp. 6435-6441, 2020/04/16 2020, doi: 10.1002/anie.201915702.

[105] M. Lai *et al.*, "Intrinsic Anion Diffusivity in Lead Halide Perovskites is Facilitated by a Soft Lattice," *Proceedings of the National Academy of Sciences*, vol. 115, no. 47, pp. 11929-11934, 2018/11/20 2018, doi: 10.1073/pnas.1812718115.

[106] Y. Bai, X. Meng, and S. Yang, "Interface Engineering for Highly Efficient and Stable Planar p-i-n Perovskite Solar Cells," *Adv. Energy Mater.,* vol. 8, no. 5, 2018, doi: 10.1002/aenm.201701883.

[107] R. A. Kerner *et al.*, "Reactions at Noble Metal Contacts with Methylammonium Lead Triiodide Perovskites: Role of Underpotential Deposition and Electrochemistry," *APL Mater.*, vol. 7, no. 4, 2019, doi: 10.1063/1.5083812.

[108] C. C. Boyd, R. Cheacharoen, K. A. Bush, R. Prasanna, T. Leijtens, and M. D. McGehee, "Barrier Design to Prevent Metal-Induced Degradation and Improve Thermal Stability in Perovskite Solar Cells," *ACS Energy Lett.*, vol. 3, no. 7, pp. 1772-1778, 2018/07/13 2018, doi: 10.1021/acsenergylett.8b00926.

[109] H. Lei *et al.*, "A Solution-Processed Pillar[5]arene-Based Small Molecule Cathode Buffer Layer for Efficient Planar Perovskite Solar Cells," *Nanoscale*, vol. 10, no. 17, pp. 8088-8098, May 3 2018, doi: 10.1039/c8nr00898a.

[110] A. Datta, P. Becla, and S. Motakef, "Novel Electrodes and Engineered Interfaces for Halide-Semiconductor Radiation Detectors," *Sci Rep,* vol. 9, no. 1, p. 9933, Jul 9 2019, doi: 10.1038/s41598-019-46360-z.

[111] K. Wang *et al.,* "Novel Inorganic Electron Transport Layers for Planar Perovskite Solar Cells: Progress and Prospective," *Nano Energy,* vol. 68, 2020, doi: 10.1016/j.nanoen.2019.104289.

[112] J. T. Tisdale *et al.,* "Precursor Purity Effects on Solution-Based Growth of MAPbBr3 Single Crystals Towards Efficient Radiation Sensing," *CrystEngComm,* vol. 20, no. 48, pp. 7818-7825, 2018, doi: 10.1039/c8ce01498a.

[113] C. C. Boyd, R. Cheacharoen, T. Leijtens, and M. D. McGehee, "Understanding Degradation Mechanisms and Improving Stability of Perovskite Photovoltaics," *Chem Rev,* vol. 119, no. 5, pp. 3418-3451, Mar 13 2019, doi: 10.1021/acs.chemrev.8b00336.

[114] G. M. Paternò *et al.,* "Perovskite Solar Cell Resilience to Fast Neutrons," *Sustainable Energy Fuels,* vol. 3, no. 10, pp. 2561-2566, 2019, doi: 10.1039/c9se00102f.

[115] Y. Miyazawa *et al.,* "Tolerance of Perovskite Solar Cell to High-Energy Particle Irradiations in Space Environment," *iScience,* vol. 2, pp. 148-155, Apr 27 2018, doi: 10.1016/j.isci.2018.03.020.

[116] V. V. Brus *et al.,* "Defect Dynamics in Proton Irradiated CH3NH3PbI3Perovskite Solar Cells," *Adv. Electron. Mater.,* vol. 3, no. 2, 2017, doi: 10.1002/aelm.201600438.

[117] N. Klein-Kedem, D. Cahen, and G. Hodes, "Effects of Light and Electron Beam Irradiation on Halide Perovskites and Their Solar Cells," *Acc Chem Res,* vol. 49, no. 2, pp. 347-54, Feb 16 2016, doi: 10.1021/acs.accounts.5b00469.

[118] Y. Cheng *et al.,* "Revealing the Degradation and Self-Healing Mechanisms in Perovskite Solar Cells by Sub-Bandgap External Quantum Efficiency Spectroscopy," *Adv Mater,* vol. 33, no. 3, p. e2006170, Jan 2021, doi: 10.1002/adma.202006170.

[119] W. Nie *et al.,* "Light-Activated Photocurrent Degradation and Self-Healing in Perovskite Solar Cells," *Nat Commun,* vol. 7, p. 11574, May 16 2016, doi: 10.1038/ncomms11574.

[120] M. Holland, A. Ruth, K. Mielczarek, V. V. Dhas, J. J. Berry, and M. D. Irwin, "Metal Halide Perovskites Demonstrate Radiation Hardness and Defect Healing in Vacuum," *ACS Appl Mater Interfaces,* Feb 10 2022, doi: 10.1021/acsami.1c24709.

[121] F. Lang, O. Shargaieva, V. V. Brus, H. C. Neitzert, J. Rappich, and N. H. Nickel, "Influence of Radiation on the Properties and the Stability of Hybrid Perovskites," *Adv Mater,* vol. 30, no. 3, Jan 2018, doi: 10.1002/adma.201702905.

[122] Y. J. Tan, J. Wu, H. Li, and B. C. K. Tee, "Self-Healing Electronic Materials for a Smart and Sustainable Future," *ACS Appl Mater Interfaces,* vol. 10, no. 18, pp. 15331-15345, May 9 2018, doi: 10.1021/acsami.7b19511.

[123] G. Nan, X. Zhang, and G. Lu, "Self-Healing of Photocurrent Degradation in Perovskite Solar Cells: The Role of Defect-Trapped Excitons," *J Phys Chem Lett,* vol. 10, no. 24, pp. 7774-7780, Dec 19 2019, doi: 10.1021/acs.jpclett.9b03413.

[124] S. Latif, S. Amin, S. S. Haroon, and I. A. Sajjad, "Self-Healing Materials for Electronic Applications: An Overview," *Mater. Res. Express,* vol. 6, no. 6, p. 062001, 2019/03/27 2019, doi: 10.1088/2053-1591/ab0f4c.

[125] A. G. Boldyreva *et al.*, "Gamma-Ray-Induced Degradation in the Triple-Cation Perovskite Solar Cells," *J Phys Chem Lett,* vol. 10, no. 4, pp. 813-818, Feb 21 2019, doi: 10.1021/acs.jpclett.8b03222.

[126] A. G. Boldyreva *et al.*, "Unravelling the Material Composition Effects on the Gamma Ray Stability of Lead Halide Perovskite Solar Cells: MAPbI3 Breaks the Records," *J Phys Chem Lett,* vol. 11, no. 7, pp. 2630-2636, Apr 2 2020, doi: 10.1021/acs.jpclett.0c00581.

[127] K. Yang *et al.*, "Radiation Tolerance of Perovskite Solar Cells Under Gamma Ray," *Org. Electron.,* vol. 71, pp. 79-84, 2019, doi: 10.1016/j.orgel.2019.05.008.

[128] S. Yang, Z. Xu, S. Xue, P. Kandlakunta, L. Cao, and J. Huang, "Organohalide Lead Perovskites: More Stable than Glass under Gamma-Ray Radiation," *Adv Mater,* vol. 31, no. 4, p. e1805547, Jan 2019, doi: 10.1002/adma.201805547.

[129] Y. Tu *et al.*, "Perovskite Solar Cells for Space Applications: Progress and Challenges," *Adv Mater,* vol. 33, no. 21, p. e2006545, May 2021, doi: 10.1002/adma.202006545.

[130] Q. Xu *et al.*, "Effect of Methylammonium Lead Tribromide Perovskite Based-Photoconductor Under Gamma Photons Radiation," *Radiat. Phys. Chem.*, vol. 181, 2021, doi: 10.1016/j.radphyschem.2020.109337.

[131] L. Gao, K. Tao, J. L. Sun, and Q. Yan, "Gamma-Ray Radiation Stability of Mixed-Cation Lead Mixed-Halide Perovskite Single Crystals," *Adv. Opt. Mater.*, vol. 10, no. 3, 2021, doi: 10.1002/adom.202102069.

[132] M. I. Saidaminov *et al.*, "High-Quality Bulk Hybrid Perovskite Single Crystals Within Minutes by Inverse Temperature Crystallization," *Nat Commun*, vol. 6, p. 7586, Jul 6 2015, doi: 10.1038/ncomms8586.

[133] G. Maculan *et al.*, "CH3NH3PbCl3 Single Crystals: Inverse Temperature Crystallization and Visible-Blind UV-Photodetector," *J Phys Chem Lett*, vol. 6, no. 19, pp. 3781-6, Oct 1 2015, doi: 10.1021/acs.jpclett.5b01666.

[134] Y. Rakita *et al.*, "CH3NH3PbBr3 is Not Pyroelectric, Excluding Ferroelectric-Enhanced Photovoltaic Performance," *APL Mater.*, vol. 4, no. 5, 2016, doi: 10.1063/1.4949760.

[135] A. Georgiev and W. Gast, "Digital Pulse Processing in High Resolution, High Throughput, Gamma-Ray Spectroscopy," *IEEE Trans. Nucl. Sci.*, vol. 40, no. 4, pp. 770-779, 1993, doi: 10.1109/23.256659.

[136] B. W. Loo, F. S. Goulding, and D. Gao, "Ballistic Deficits in Pulse Shaping Amplifiers," *IEEE Trans. Nucl. Sci.*, vol. 35, no. 1, pp. 114-118, 1988, doi: 10.1109/23.12686.

[137] M. Nakhostin and K. Hitomi, "Pulse-Height Loss in the Signal Readout Circuit of Compound Semiconductor Detectors," *Nucl. Instrum. Methods Phys. Res. A: Accel. Spectrom. Detect. Assoc. Equip.*, vol. 893, pp. 146-150, 2018, doi: 10.1016/j.nima.2018.03.053.

[138] S. Cornaby and K. Kozaczek, "X-Ray Sources for Handheld X-Ray Fluorescence Instruments," in *Encyclopedia of Analytical Chemistry*, 2016, pp. 1-25.

[139] M. J. Berger *et al. XCOM: Photon Cross Section Database (version 1.5)*. [Online]. Available: http://physics.nist.gov/xcom

[140] F. v. Loon *et al.*, "Intracavity Diamond Heatspreaders in Lasers: The Effects of Birefringence," *Opt. Express*, vol. 14, no. 20, pp. 9250-9260, 2006/10/02 2006, doi: 10.1364/OE.14.009250.

[141] G. Turri, "Optical Absorption, Depolarization, and Scatter of Epitaxial Single-Crystal Chemical-Vapor-Deposited Diamond at 1.064μm," *Optical Engineering*, vol. 46, no. 6, 2007, doi: 10.1117/1.2748044.

[142] H. Spieler, *Semiconductor Detector Systems*. Oxford University Press, 2005.

[143] S. Ebnesajjad, "Chapter 4 - Surface and Material Characterization Techniques," in *Surface Treatment of Materials for Adhesive Bonding (Second Edition)*, S. Ebnesajjad Ed. Oxford: William Andrew Publishing, 2014, pp. 39-75.

[144] A. Thompson *et al.*, *X-Ray Data Booklet*. Berkeley, CA: Lawrence Berkeley National Laboratory, 2009.

[145] K. Nakada, Y. Matsumoto, Y. Shimoi, K. Yamada, and Y. Furukawa, "Temperature-Dependent Evolution of Raman Spectra of Methylammonium Lead Halide Perovskites, CH3NH3PbX3 (X = I, Br)," *Molecules*, vol. 24, no. 3, 2019, doi: 10.3390/molecules24030626.

[146] Y. Liu, Z. Yang, and S. F. Liu, "Recent Progress in Single-Crystalline Perovskite Research Including Crystal Preparation, Property Evaluation, and Applications," *Adv Sci (Weinh)*, vol. 5, no. 1, p. 1700471, Jan 2018, doi: 10.1002/advs.201700471.

[147] T. Markvart and L. Castañer, "Chapter I-1-B - Semiconductor Materials and Modeling," in *McEvoy's Handbook of Photovoltaics (Third Edition)*, S. A. Kalogirou Ed.: Academic Press, 2018, pp. 29-57.

[148] X. Xiao *et al.*, "Argon Plasma Treatment to Tune Perovskite Surface Composition for High Efficiency Solar Cells and Fast Photodetectors," *Adv Mater*, vol. 30, no. 9, Mar 2018, doi: 10.1002/adma.201705176.

[149] J. van der Weide and R. J. Nemanich, "Argon and Hydrogen Plasma Interactions on Diamond (111) Surfaces: Electronic States and Structure," *Appl. Phys. Lett.*, vol. 62, no. 16, pp. 1878-1880, 1993, doi: 10.1063/1.109639.

[150] D. F. O'Kane and K. L. Mittal, "Plasma Cleaning of Metal Surfaces," *Journal of Vacuum Science and Technology*, vol. 11, no. 3, pp. 567-569, 1974, doi: 10.1116/1.1318069.

[151] Y. Liu *et al.*, "Flexible Lead Bromide Perovskite Solar Cells," *ACS Appl. Energy Mater.*, vol. 3, no. 10, pp. 9817-9823, 2020, doi: 10.1021/acsaem.0c01473.

[152] J. M. Frost and A. Walsh, "What Is Moving in Hybrid Halide Perovskite Solar Cells?," *Acc Chem Res*, vol. 49, no. 3, pp. 528-35, Mar 15 2016, doi: 10.1021/acs.accounts.5b00431.

[153] K. Higgins *et al.*, "Exploration of Electrochemical Reactions at Organic–Inorganic Halide Perovskite Interfaces via Machine Learning in In Situ Time-of-Flight Secondary Ion Mass Spectrometry," *Adv. Funct. Mater.*, vol. 30, no. 36, 2020, doi: 10.1002/adfm.202001995.

[154] M. Ahmadi, L. Collins, K. Higgins, D. Kim, E. Lukosi, and S. V. Kalinin, "Spatially Resolved Carrier Dynamics at MAPbBr3 Single Crystal-Electrode Interface," *ACS Appl Mater Interfaces*, vol. 11, no. 44, pp. 41551-41560, Nov 6 2019, doi: 10.1021/acsami.9b16287.

[155] S. Meloni *et al.*, "Ionic Polarization-Induced Current-Voltage Hysteresis in CH3NH3PbX3 Perovskite Solar Cells," *Nat Commun*, vol. 7, p. 10334, Feb 8 2016, doi: 10.1038/ncomms10334.

[156] A. Musiienko *et al.*, "Deep Levels, Charge Transport and Mixed Conductivity in Organometallic Halide Perovskites," *Energy Environ. Sci.*, vol. 12, no. 4, pp. 1413-1425, 2019, doi: 10.1039/c9ee00311h.

[157] W. Tress, N. Marinova, T. Moehl, S. M. Zakeeruddin, M. K. Nazeeruddin, and M. Grätzel, "Understanding the Rate-Dependent J–V Hysteresis, Slow Time Component, and Aging in CH3NH3PbI3 Perovskite Solar Cells: The Role of a Compensated Electric Field," *Energy Environ. Sci.*, vol. 8, no. 3, pp. 995-1004, 2015, doi: 10.1039/c4ee03664f.

[158] D. Kim *et al.*, "Ferroelectric and Charge Transport Properties in Strain-Engineered Two-Dimensional Lead Iodide Perovskites," *Chem. Mater.*, vol. 33, no. 11, pp. 4077-4088, 2021, doi: 10.1021/acs.chemmater.1c00679.

[159] D. M. Trucchi, P. Allegrini, A. Bellucci, P. Calvani, A. Galbiati, and M. Girolami, "Resistant and Sensitive Single-Crystal Diamond Dosimeters for Ionizing Radiation," *Nucl. Instrum. Methods Phys. Res. A: Accel. Spectrom. Detect. Assoc. Equip.*, vol. 718, pp. 373-375, 2013, doi: 10.1016/j.nima.2012.10.095.

[160] M. Jung, J. Morel, and P. Siffert, "Real-Time High Intensity X-ray Dosimetry Diamond Monitors: Response Simulations Compared to Silicon Sensitivities," *Nucl. Instrum. Methods Phys. Res. A: Accel. Spectrom. Detect. Assoc. Equip.*, vol. 554, no. 1-3, pp. 514-526, 2005, doi: 10.1016/j.nima.2005.07.063.

[161] R. W. Pringle, H. W. Taylor, and K. I. Roulston, "Radiative Capture of Thermal Neutrons by Cd113," *Phys. Rev.*, vol. 87, no. 6, pp. 1016-1017, 09/15/ 1952, doi: 10.1103/PhysRev.87.1016.

[162] A. Plompen *et al.*, "High-Resolution Study of the113Cd(n,γ) Spectrum by Statistical Decay Model with Discrete Levels and Transitions," *EPJ Web Conf.*, vol. 146, 2017, doi: 10.1051/epjconf/201714605009.

[163] P. L. Mulligan, L. R. Cao, and D. Turkoglu, "A Multi-Detector, Digitizer Based Neutron Depth Profiling Device for Characterizing Thin Film Materials," *Rev Sci Instrum*, vol. 83, no. 7, p. 073303, Jul 2012, doi: 10.1063/1.4732168.

[164] D. Turkoglu, J. Burke, R. Lewandowski, and L. R. Cao, "Characterization of a New External Neutron Beam Facility at The Ohio State University," *J. Radioanal. Nucl. Chem.*, vol. 291, no. 2, pp. 321-327, 2011, doi: 10.1007/s10967-011-1289-2.

[165] J. Peng, Y. Chen, K. Zheng, T. Pullerits, and Z. Liang, "Insights Into Charge Carrier Dynamics in Organo-Metal Halide Perovskites: From Neat Films to Solar Cells," *Chem Soc Rev*, vol. 46, no. 19, pp. 5714-5729, Oct 2 2017, doi: 10.1039/c6cs00942e.

[166] W. Pan *et al.*, "Cs2AgBiBr6 Single-Crystal X-ray Detectors with a Low Detection Limit," *Nat. Photonics*, vol. 11, no. 11, pp. 726-732, 2017, doi: 10.1038/s41566-017-0012-4.

[167] S. N. Ahmed, *Physics and Engineering of Radiation Detection*. San Diego, UNITED STATES: Elsevier, 2014.

[168] G. S. Camarda *et al.*, "Polarization Studies of CdZnTe Detectors Using Synchrotron X-Ray Radiation," *IEEE Trans. Nucl. Sci.*, vol. 55, no. 6, pp. 3725-3730, 2008, doi: 10.1109/tns.2008.2004707.

[169] M. Strassburg, C. Schroeter, and P. Hackenschmied, "CdTe/CZT Under High Flux Irradiation," *J. Instrum.*, vol. 6, no. 01, pp. C01055-C01055, 2011, doi: 10.1088/1748-0221/6/01/c01055.

[170] H. Elhadidy, V. Dedic, J. Franc, and R. Grill, "Study of Polarization Phenomena in n-type CdZnTe," *J. Phys. D: Appl. Phys.*, vol. 47, no. 5, 2014, doi: 10.1088/0022-3727/47/5/055104.

[171] B. Yang *et al.*, "Controllable Growth of Perovskite Films by Room-Temperature Air Exposure for Efficient Planar Heterojunction Photovoltaic Cells," *Angew Chem Int Ed Engl*, vol. 54, no. 49, pp. 14862-5, Dec 1 2015, doi: 10.1002/anie.201505882.

[172] A. Musiienko *et al.*, "Deciphering the Effect of Traps on Electronic Charge Transport Properties of Methylammonium Lead Tribromide Perovskite," *Sci. Adv.*, vol. 6, no. 37, p. eabb6393, 2020, doi: 10.1126/sciadv.abb6393.

[173] M. Marinelli *et al.*, "Analysis of Traps in High Quality CVD Diamond Films Through the Temperature Dependence of Carrier Dynamics," *Diamond Relat. Mater.*, vol. 12, no. 10-11, pp. 1733-1737, 2003, doi: 10.1016/s0925-9635(03)00204-8.

[174] L. Milazzo and A. Mainwood, "Modelling of Diamond Particle Detectors: Temperature Dependence of the Trapping and Detrapping Phenomena," *Diamond Relat. Mater.*, vol. 12, no. 3-7, pp. 658-661, 2003, doi: 10.1016/s0925-9635(02)00315-1.

[175] S.-H. Park *et al.*, "Temperature Effect on the CZT Radiation Detector Performance," *J. Korean Phys. Soc.*, vol. 56, no. 4, pp. 1079-1082, 2010, doi: 10.3938/jkps.56.1079.

[176] B. W. Sturm, H. Zhong, T. H. Zurbuchen, and P. L. Koehn, "Investigation of the Asymmetric Characteristics and Temperature Effects of CdZnTe Detectors," *IEEE Trans. Nucl. Sci.*, vol. 52, no. 5, pp. 2068-2075, 2005, doi: 10.1109/tns.2005.856728.

Appendix

List of Abbreviations

BCP	Bathocuproine
CCE	Charge Collection Efficiency
CLCF	Charge Loss Correction Factor
CZT	CdZeTe
DCF	Depth Correction Factor
DCM	Dichloromethane (CH_2Cl_2)
DMF	Dimethylformamide ($(CH_3)_2NC(O)H$)
DMSO	Dimethyl Sulfoxide ($(CH_3)_2SO$)
EDX/EDS	Energy Dispersive X-ray Spectroscopy
ETL	Electron Transport Layer
FA	Formamidinium ($HC(NH_2)_2^+$)
FEP	Full Energy Peak
FFT	Fast Fourier Transform
FWHM	Full Width Half Maximum
HDPE	High Density Polyethylene
HPGe	High Purity Germanium
HPSi	High Purity Silicon
HTL	Hole Transport Layer
ICP-OES	Inductive Coupled Plasma-Optical Emission Spectrometry
ITC	Inverse Temperature Crystallization

I-V	Current-Voltage
LiMAPB	MAPB doped with lithium in the form of LiCl
MA	Methylammonium ($CH_3NH_3^+$)
MAPB	$CH_3NH_3PbBr_3$, or $MAPbBr_3$
MCNP	Monte Carlo N-Particle Transport Code
MHP	Metal Halide Perovskite
OMHP	Organometallic Halide Perovskite
OSURR	The Ohio State University Research Reactor
PL	Photoluminescence
PuBe	^{239}Pu/Be neutron source
RIID	Radioisotope Identification Device
RMS	Root Mean Square
SC	Single Crystal
SNM	Special Nuclear Material
SNR	Signal to Noise Ratio
SRV	Surface Recombination Velocity
TCC	Trap Controlled Conductivity
ToF	Time of Flight
TRPL	Time Resolved Photoluminescence
XPS	X-ray Photoelectron Spectroscopy
XRD	X-ray Diffraction

Vita

Ryan Tan was born in December of 1996 in Pennsylvania. He received his Bachelor of Science degree in chemical engineering from the University of Pittsburgh in April of 2018, and began his dissertation research for his Ph.D. in nuclear engineering at the University of Tennessee-Knoxville (UTK) in August of 2018 under the advisement of Dr. Eric Lukosi. While at UTK, Ryan also received a Master of Science degree in nuclear engineering in 2020, along with a Master of Arts degree in political science in 2021. He has had experience working at Oak Ridge National Laboratory, the National Nuclear Security Administration, and Y-12 National Security Complex in radiochemistry, nuclear incident response, and nuclear nonproliferation, and has received awards from the Nuclear Regulatory Commission, Health Physics Society, and Waste Management Symposia.